A Self-bound Dilute Quantum Liquid of Dysprosium Atoms

Von der Fakultät Mathematik und Physik der Universität Stuttgart
zur Erlangung des akademischen Grades eines Doktors der
Naturwissenschaften (Dr. rer. nat.) genehmigte Abhandlung

vorgelegt von

Matthias Schmitt

aus Trier

Hauptberichter:	Prof. Dr. Tilman Pfau
Mitberichter:	Prof. Dr. Hidenori Takagi
Prüfungsvorsitzender:	Prof. Dr. Hans Peter Büchler
Tag der mündlichen Prüfung:	22. März 2017

5. Physikalisches Institut
Universität Stuttgart
2017

Abstract

Self-bound many-body systems are formed through a balance of attractive and repulsive forces and these systems occur in many physical scenarios. For example liquid droplets are formed by a balance of the mutual attractive and repulsive forces that derive from different components of the inter-particle potential. However, the creation of self-bound ensembles of ultracold atoms has not been possible up to now because they require forces other than the usual short-range contact interaction, which is either attractive or repulsive but never both. In contrast to purely contact interacting gases, a dipolar Bose-Einstein condensate adds the dipolar interaction that itself can be attractive or repulsive. The recent observation that such a dipolar Bose-Einstein condensate restabilizes to quantum droplets after an initial collapse paved the way for a new research direction that goes beyond the standard mean-field approach. In this thesis, we report on the observation that these droplets can become self-bound in a trap-free levitation field and that they exhibit similar properties as a quantum liquid. We observe the existence of a critical number of atoms for the dilute magnetic quantum liquid, below which it evaporates into an expanding gas. Consequently, we observe an interaction-driven phase transition around this critical atom number between a self-bound liquid and a gas in the quantum degenerate regime.

List of Publications

In the framework of this thesis, the following articles have been published:

- M. Schmitt, M. Wenzel, F. Böttcher, I. Ferrier-Barbut and T.Pfau, *Self-bound droplets of a dilute magnetic quantum liquid*, Nature **539**, 259-262 (2016).
- I. Ferrier-Barbut, M. Schmitt, M. Wenzel, H. Kadau and T. Pfau, *Liquid quantum droplets of ultracold magnetic atoms*, Journal of Physics B: Atomic, Molecular and Optical Physics, **49**, 214004 (2016).
- I. Ferrier-Barbut, H. Kadau, M. Schmitt, M. Wenzel and T. Pfau, *Observation of quantum droplets in a strongly dipolar Bose gas*, Phys. Rev. Lett. **116**, 215301 (2016).
- H. Kadau, M. Schmitt, M. Wenzel, C. Wink, T. Maier, I. Ferrier-Barbut and T. Pfau, *Observing the Rosensweig instability of a quantum ferrofluid*, Nature **530**, 194-197 (2016).
- T. Maier, I. Ferrier-Barbut, H. Kadau, M. Schmitt, M. Wenzel, C. Wink, T. Pfau, K. Jachymski and P. S. Julienne, *Broad universal Feshbach resonances in a chaotic spectrum of dysprosium atoms*, Phys. Rev. A **92**, 060702(R) (2015).
- T. Maier, H. Kadau, M. Schmitt, M. Wenzel, I. Ferrier-Barbut, T. Pfau, A. Frisch, S. Baier, K. Aikawa, L. Chomaz, M. J. Mark, F. Ferlaino, C. Makrides, E. Tiesinga, A. Petrov and S. Kotochigova, *Emergence of Chaotic Scattering in Ultracold Er and Dy*, Phys. Rev. X **5**, 041029 (2015).
- T. Maier, H. Kadau, M. Schmitt, A. Griesmaier and T. Pfau, *Narrow-line magneto-optical trap for dysprosium atoms*, Optics Letters **39**, 3138 (2014).
- M. Schmitt, E. A. L. Henn, J. Billy, H. Kadau, T. Maier, A. Griesmaier and T. Pfau, *Spectroscopy of a narrow-line optical pumping transition in atomic dysprosium*, Optics Letters **38**, 637 (2013).

Contents

Zusammenfassung

Gegenstand dieser Dissertation ist die Untersuchung des kürzlich beobachteten Zustandes eines Quanten-Tröpfchens, welches aus einem ultrakalten atomaren Gas geformt wurde. Zu diesem Zweck wurden Experimente zur Charakterisierung des Entstehungsvorganges durchgeführt. Schließlich wurde durch die Beobachtung, dass ein Quanten-Tröpfchen selbst-gebunden ist, gezeigt, dass diese dem Zustand einer Quantenflüssigkeit ähnlicher sind als der eines Quantengases.

Eine wichtige Forschungsrichtung in der Physik beschreibt die Untersuchung verschiedener Aggretatszustände und das Konzipieren neuer Zustände mit einzigartigen Eigenschaften. Einige Aggregatzustände erfahren wir täglich: Festkörper, Flüssigkeiten, Gase und Plasmen. Bei einem Zustandswechsel spricht man von einem Phasenübergang. Verschiedene Zustände werden oft in einem Phasendiagramm zusammen dargestellt. So können beispielsweise Festkörper, Flüssigkeiten und Gase in einem $P - T$ Diagramm dargestellt werden in dem die einzelnen Phasen einzigartig für verschiedene Drücke und Temperaturen auftauchen.

Der erste quantenmechanische Aggregatzustand konnte erst nach 1908 durch die Verflüssigung von Helium angestrebt werden. Dieser Durchbruch von Heike Kamerlingh Onnes erlaubte es Temperaturen zu erreichen, die nur wenige Kelvin über dem absoluten Nullpunkt liegen. Im Jahre 1913 wurde er deshalb mit dem Nobelpreis für Physik ausgezeichnet [1]. Bereits 1911 benutzte er einen Kryostaten mit flüssigem Helium um festes Quecksilber zu kühlen. Er entdeckte, dass der elektrische Widerstand des Quecksilbers unterhalb einer gewissen kritischen Temperatur von $T_\mathrm{k} = 4.2\,\mathrm{K}$ nicht mehr messbar war - das Quecksilber wurde supraleitend. Während denselben Experimenten beobachtete er einen zweiten Phasenübergang, dieses Mal im Helium selbst bei einer Temperatur von $T_\lambda = 2.2\,\mathrm{K}$, was er allerdings nur in seinen Notizen erwähnte [2]. Später interpretierten Kapitza, Allen und Misener diesen Übergang als Phasenübergang zu einem suprafluiden Zustand, welcher durch eine verschwindende innere Reibung charakterisiert ist [3, 4]. Im selben Jahr erklärte London, dass der Phasenübergang von einer sogenannten Bose-Einstein-Kondensation (BEK) und einer starken Wechselwirkung zwischen den Helium Teilchen stammt [5]. Im Gegensatz zu einem klassichen Phasenübergang resultiert die Bose-Einstein-Kondensation aus der Statistik der bosonischen Teilchen.

In dieser Dissertation arbeiten wir mit stark verdünnten atomaren Gasen bei ultrakalten Temperaturen - ungefähr ein Millionstel über dem absoluten Nullpunkt. Bei diesen Bedingungen können die Atome ebenfalls ein Bose-Einstein-Kondensat bilden. Der erste experimentelle Nachweis eines BEKs in Alkalimetallen war 1995 [6–8], welcher 2001 mit dem Nobelpreis für Physik ausgezeichnet wurde. Seitdem versuchen Forscher die Eigenschaften dieses Zustandes zu entschlüsseln, sowohl theoretisch als auch experimentell mit ultrakalten Atomen.

Obwohl diese Gase stark verdünnt sind und die Wechselwirkung zwischen den Atomen deutlich schwächer als bei flüssigem Helium ist, wussten Forscher, dass die Wechselwirkungen im gasförmigen BEK eine dominante Rolle spielen [9]. Insbesondere sind Wechselwirkungen verantwortlich dafür, dass BEKs suprafluide Eigenschaften besitzen. Aus diesem Grund ist es wichtig die Wechselwirkungen in einem BEK kontrollieren zu können um damit später weitere Quantenzustände studieren zu können. In Alkalimetallen dominiert eine kurzreichweitige Wechselwirkung, die durch einen einzigen Parameter charakterisiert werden kann: die s-Wellen Streulänge a. Diese Streulänge, und damit die Stärke der Wechselwirkung, kann durch sogenannte Feshbach Resonanzen (FR) verändert werden. Eine FR wurde 1998 zum ersten Mal in einem BEK beobachtet [10] und ist seitdem ein wichtiges Werkzeug für ultrakalte Quantengase [11]. Diese Resonanzen sind allerdings nicht einzigartig für bosonische Teilchen. Mit ihrer Hilfe wurden bereits molekulare BEKs [12–14] aus fermionischen Quantengasen erstellt [15].

Obwohl ein BEK aus ultrakalten Atomen suprafluide Eigenschaften besitzt, ist es dennoch ein Gas und muss deshalb durch ein externes Fallenpotential gehalten werden. Im Gegensatz zum Gas ist suprafluides ^{4}He eine Quantenflüssigkeit und deshalb selbstgebunden. Diese Eigenschaft zeigt sich durch das Ausbilden stabiler Tröpfchen. Aufgrund der interessanten Quantennatur beschreiben flüssige Tröpfchen aus Helium ein intensives Forschungsthema [16, 17]. Diese Tröpfchen existieren durch gegenseitige anziehende und abstoßende Kräfte die aus der van-der-Waals Anziehung und der Abstoßung des Paulischen Ausschließungsprinzips resultieren. Sie dienen als abgeschlossenes, isoliertes Quantensystem mit dem beispielsweise die Suprafluidität von einem mesoskopischen Ensemble untersucht werden kann [18]. Weitere Beispiele für selbst-gebundene Quantenflüssigkeiten sind Atomkerne [19], die durch ein Gleichgewicht zwischen der attraktiven, kurzreichweitigen Kernkraft und der Abstoßung der Nukleonen durch das Paulische Ausschließungsprinzip und der Coulombkraft zusammengehalten werden. Neutronensterne [20] stabilisieren sich selbst durch das Gleichgewicht zwischen der Eigengravitation und dem Entartungsdruck der Neutronen, welcher wiederum durch das Paulische Ausschließungsprinzip beschrieben wird. Selbst-gebundene Quanten-Tröpfchen geformt von ultrakalten atomare Gasen wurden vorhergesagt [21, 22], konnten allerdings bisher nicht erzeugt werden da

zusätzliche Kräfte neben der kurzreichweitigen Kontaktwechselwirkung benötigt werden.

Die ersten selbst-gebundenen makroskopischen Objekte in BEKs waren Solitonen [23, 24]. Diese Solitonen wurden in quasi-eindimensionalen BEKs beobachtet und existieren aufgrund schwacher attraktiver Wechselwirkung, die der natürlichen Expansion aufgrund der kinetischen Energie entgegenwirkt. Allerdings sind die beobachteten Solitonen nur entlang einer Raumrichtung selbst-gebunden und mussten weiterhin in die beiden anderen Richtungen durch ein Fallenpotential gehalten werden.

Im Jahre 2005 wurde zum ersten Mal ein BEK aus Chromatomen hergestellt [25] und brachte eine neue Art der Wechselwirkung mit sich: die Dipol-Dipol Wechselwirkung. Im Gegensatz zur kurzreichweitigen und isotropen Kontaktwechselwirkung ist die Dipol-Dipol Wechselwirkung langreichweitig und anisotrop. Chromatome besitzen ein magnetisches Moment von $\mu_\mathrm{m} = 6\,\mu_\mathrm{B}$, mit μ_B dem Bohrschen Magneton. Dadurch ist die dipolare Wechselwirkung nicht mehr vernachlässigbar und erste Experimente beobachteten bereits den Effekt der Magnetostriktion, die Ausdehnung der ultrakalten Wolke entlang des Magnetfeldes [26, 27]. Weitere Studien an dipolaren BEKs wurden in Stuttgart und Paris durchgeführt [28, 29]. Es stellte sich heraus, dass die Stabilität eines dipolaren BEKs durch die Dipol-Dipol Wechselwirkung modifiziert wird [30, 31]. Unter gewissen Bedingungen, bei denen die gesamte Wechselwirkung zwischen den Atomen anziehend wirkt, kollabiert ein dipolares BEK und zeigt eine d-Wellen Symmetrie [32–34]. Die dipolare Wechselwirkung koppelt Spin und Bahndrehimpuls der Elektronen [35, 36] und erlaubt dipolaren Gasen eine einzigartige Kühlmethode: das Entmagnetisierungskühlen [37]. Diese Spinrelaxation war ebenfalls wichtig bei der Untersuchung von sogenannten dipolaren Spinor BEKs [38, 39]. Zusätzlich gibt es eine anisotrope Modifizierung der kollektiven Modenfrequenzen [40] und des Anregungssprektrums [41] der Chromatome durch die dipolare Wechselwirkung.

Trotz des hohen magnetischen Moments von Chrom ist der Beitrag der dipolaren Wechselwirkung zur gesamten Wechselwirkung nur ungefähr 16 % [42]. Trotzdem konnte mit Hilfe einer FR ein stark dipolares BEK mit Chromatomen hergestellt werden [43], allerdings war aufgrund der FR die Lebensdauer des BEKs stark limitiert. Diese Limitierung wurde durch die Bose-Einstein-Kondensation der beiden Lanthanide Dysprosium [44, 45] und Erbium [46, 47] überwunden. Beide Elemente besitzen ein höheres magnetisches Moment als Chrom mit $\mu_\mathrm{m,Dy} = 10\,\mu_\mathrm{B}$ und $\mu_\mathrm{m,Er} = 7\,\mu_\mathrm{B}$. Zusätzlich weisen beide Elemente ein dichtes, chaotisches Feshbach Spektrum auf [48, 49] welches die Möglichkeit zur Erzeugung von stark magnetischen Molekülen eröffnet [50, 51]. Vor kurzem wurde ein Quanten-Ferrofluid aus einem Dysprosium BEK erstellt [52], in der die Rosensweig-Instabilität [53] beobachtet werden konnte. Im Gegensatz zum Kollaps eines Chrom BEKs stellte sich heraus, dass sich ein Dysprosium BEK nach einem anfänglichen Kollaps wieder

stabilisiert und Quanten-Tröpfchen bildet [54].

Diesen Phasenübergang zwischen einem ^{164}Dy BEK und einem Quanten-Tröpfchen haben wir genauer untersucht. Die Molekularfeldtheorie prognostiziert, dass ein Dysprosium BEK ähnlich wie ein Chrom BEK kollabieren sollte. Die Entstehung der Quanten-Tröpfchen konnte allerdings durch Simulationen mit Hilfe einer effektiven Gross-Pitaevskii Gleichung bestätigt werden. Im Gegensatz zur Molekularfeldtheorie mussten Quantenfluktuationen berücksichtigt werden, die eine zusätzliche repulsive Kraft hervorrufen.

Zur experimentellen Untersuchung des Phasenübergangs wurde zunächst ein BEK in einer optischen Falle erstellt und mittels eines Magnetfelds wurden die atomaren Magnete ausgerichtet. Mithilfe einer Feshbach Resonanz wurde das BEK für verschiedene Seitenverhältnisse der Falle in den instabilen Bereich gebracht. Wir beobachteten, dass oberhalb eines kritischen Seitenverhältnisses von $\lambda_c = 1.87(8)$ abhängig von der Atomzahl im BEK grundsätzlich mehrere dieser Quanten-Tröpfchen entstanden. Hier handelt es sich um einen Phasenübergang erster Ordnung nach der Definition von Ehrenfest. In diesem Bereich haben wir die kritische Streulänge gemessen, bei der wir den Phasenübergang beobachteten. Durch Simulationen und Variationsrechnungen mit einem Gaußansatz stellte sich heraus, dass dieser Übergang durch ein Rotonenkollaps in einem bistabilen Bereich hervorgerufen wird. In diesem bistabilen Bereich koexistieren die BEK-Phase und die Tröpfchen-Phase. Im Gegensatz dazu entstand unterhalb dieses kritischen Seitenverhältnisses stets nur ein einzelnes Quanten-Tröpfchen. In diesem Bereich beobachteten wir einen kontinuierlichen Übergang zwischen BEK und Tröpfchen. Diese Messungen führten schließlich zu einem Phasendiagramm, in dem wir drei Phasen identifizierten: die BEK-Phase, die Tröpfchen-Phase und die bistabile Phase.

Eine faszinierende Eigenschaft dieser Quanten-Tröpfchen ist die Tatsache, dass sie selbst-gebunden sind. Um dies experimentell nachzuweisen nutzten wir die bereits erlangten Kenntnisse zur deterministischen Erstellung eines einzelnen Tröpfchens in der optischen Falle. Die Falle wurde anschließend adiabatisch ausgeschaltet und wir ließen die Tröpfchen mit Hilfe eines Magnetfeldgradienten schweben. Wir beobachteten, dass die Tröpfchen erst nach gewisser Zeit expandierten, und fanden eine maximale Lebensdauer von 100 ms. Den Effekt der Expansion erklären wir dadurch, dass die Tröpfchen Atome verlieren bis sie einen kritische Atomzahl unterschreiten. Ab diesem Zeitpunkt ist das Wechselwirkungsgleichgewicht nicht mehr gegeben und aufgrund der kinetischen Energie der Atome führt dies zu einem abstoßenden Effekt, den wir als Expansion wahrnehmen. Diese kritische Atomzahl wurde für verschiedene Streulängen gemessen und beschreibt die Phasengrenzlinie zwischen den selbst-gebundenen Tröpfchen und dem ungebundenen Gas. Ein Vergleich zwischen den gemessenen kritischen Atomzahlen und den Simulationen resultierte in einer Neubestimmung der Hintergrundstreulänge für das ^{164}Dy Isotop.

Introduction

The research in physics is driven by curiosity to understand the universe we live in. One important direction is understanding the different states of matter and design new phases with novel properties. The most prominent states that we experience in our everyday life are solids, liquids, gases and plasmas. A change from one state to another is called a phase transition. All possible phases are typically connected in a phase diagram. For the mentioned classical states, we can connect solids, liquids and gases in a $P-T$-diagram, meaning all phases are unique for different pressures and temperatures.

The first observation of a quantum mechanical macroscopic state was enabled through the liquefaction of helium in 1908. This breakthrough by Heike Kamerlingh Onnes allowed to reach temperatures of a few Kelvin above the absolute zero temperature point and awarded him the Nobel prize in physics in 1913 [1]. In 1911, he used a cryostat to cool down solid mercury below $T_\mathrm{c} = 4.2\,\mathrm{K}$, the critical temperature for superconductivity. In the same experiments, he observed a transition in helium at $T_\lambda = 2.2\,\mathrm{K}$ without paying further attention to this [2]. This transition was later on interpreted as the transition to a superfluid state characterized by a zero viscosity [3, 4]. This superfluid transition was later understood as arising from a so-called Bose-Einstein condensation [5], together with strong interactions between the particles. In contrast to a classical phase transition, Bose-Einstein condensation is a result of the statistics of the bosonic particles.

In this thesis, we are working with dilute atomic gases at extremely low temperatures - on the order of a millionth of a Kelvin above absolute zero. In these conditions, the ultracold atoms can condense as well to a Bose-Einstein condensate (BEC). The first observation of the BEC phase for alkali atoms was reported in 1995 [6–8] which was awarded with the Nobel prize in 2001. Since then, researchers try to unravel the properties of this state both theoretically and experimentally using ultracold atoms.

Although the gases are very dilute and interactions are much weaker than in the case of liquid helium, it became clear that interactions play a dominant role in gaseous BECs [9]. In particular, interactions are fundamental to provide superfluid properties to BECs. The ability to control the interactions in a BEC is thus key to study novel quantum states. In alkali atoms the dominant interaction is a short-range interaction which can be characterized by a single parameter: the s-wave scattering length a. Tuning of the contact

interaction strength is possible through so-called Feshbach resonances (FRs), which were first observed in a BEC in 1998 [10]. Since then, FRs are a major tool in ultracold atomic systems [11]. They are not unique for bosonic systems and they have been successfully used to create molecular BECs [12–14] formed from fermionic quantum gases [15].

Although being superfluid, a BEC of ultracold atoms is still in the gas phase and therefore needs to be confined by an external trapping potential. In contrast, superfluid ^{4}He is in a liquid state and therefore self-bound. This self-bound liquid character manifests itself through the formation of droplets. Due to their interesting quantum nature, liquid helium droplets constitute an intense field of research [16, 17]. These self-bound droplets are formed by the mutual attractive and repulsive forces resulting from van-der-Waals attraction and the electronic Pauli exclusion principle, respectively. They can serve as closed, isolated quantum systems with which to probe, for example, superfluidity of mesoscopic ensembles [18]. Further examples of self-bound quantum liquids are nuclei [19], which are based on a balance of an attractive short-range nuclear force and the Pauli and Coulomb repulsion of the nucleons. In neutron stars [20], the balance between self-gravitating forces and the neutron degeneracy pressure, described by the Pauli exclusion principle, are responsible for their stability. Self-bound quantum droplets formed from ultracold atoms have been suggested [21, 22] but so far it was not possible to observe them since they require forces other than the usual zero-range contact interaction.

In BECs, the first self-bound macroscopic objects observed were bright solitons [23, 24]. These solitons are observed in quasi-one-dimensional BECs resulting from a weakly attractive interaction that counteracts the natural expansion due to the kinetic energy. The self-bound character was thus observed only along one direction of space, while the other two directions still had to be confined by a trapping potential.

The first realization of a chromium BEC [25] in 2005 opened the possibility to study the effect of a new kind of interaction in quantum gases: the dipole-dipole interaction. In contrast to the short-range and isotropic contact interaction, the dipole-dipole interaction is long-range and anisotropic. With the magnetic moment of chromium of $\mu_\mathrm{m} = 6\,\mu_\mathrm{B}$, where μ_B is the Bohr magneton, the dipole-dipole interaction is not negligible and early experiments already allowed the observation of magnetostriction, namely the elongation of the cloud along the magnetic field direction [26, 27]. Further studies on dipolar BECs have been performed in Stuttgart and Paris [28, 29]. It has been shown that the stability of a dipolar BEC is modified by the dipolar interaction [30, 31]. Under conditions where the overall interaction between the atoms is attractive, a dipolar BEC has been shown to collapse and the collapse product exhibits a d-wave symmetry [32–34]. The dipolar interaction couples the spin degree of freedom with the orbital angular momentum [35, 36] allowing for a cooling method unique to dipolar atoms: the demagnetization cooling

[37]. The spin relaxation was also important in spinor physics with dipolar BECs [38, 39]. Additionally, the dipolar interaction anisotropically modifies the collective mode frequencies of chromium [40] as well as the excitation spectrum [41].

Although chromium has a large magnetic moment, the contribution of the dipolar interaction to the total interaction energy is only about 16 % [42]. Nevertheless, using a FR a chromium BEC was brought into the strongly dipolar regime [43], however low lifetimes resulting from the FR limited the observation times. This limitation was overcome with the condensation of two lanthanides: dysprosium [44, 45] and erbium [46, 47]. Both species possess a higher magnetic moment than chromium with $\mu_{\mathrm{m,Dy}} = 10\,\mu_{\mathrm{B}}$ and $\mu_{\mathrm{m,Er}} = 7\,\mu_{\mathrm{B}}$. Due to their complex structure, both elements exhibit a dense chaotic Feshbach spectrum [48, 49] opening the possibility to create strongly magnetic molecules [50, 51]. Most recently, it was possible to mimic the Rosensweig instability [53] and create a quantum ferrofluid from a dysprosium quantum gas [52]. We will see in this thesis that the study of Dy BECs have allowed us to demonstrate that the collapse of a dipolar BEC observed in chromium BECs is prevented for dysprosium owing to its strong dipole interaction, resulting in a so-called quantum droplet [54].

Outline of this thesis

In this thesis we further clarify the recently observed state of a quantum droplet.

We start by introducing the theory of dipolar Bose-Einstein condensates in chapter 1. We describe the two relevant inter-particle interactions, starting with the short-range isotropic contact interaction and a method to modify the interaction strength using Feshbach resonances. We continue with a description of the dipolar interaction which is long-range and anisotropic. Combining both interactions, we introduce the Gross-Pitaevskii equation in a mean-field treatment. A Gaussian variational ansatz, as well as the Thomas-Fermi approximation help to find semi-analytical solutions to the Gross-Pitaevskii equation. We introduce the quantum fluctuations as first correction beyond the mean-field description and finally expand the Gross-Pitaevskii equation to include this correction.

In chapter 2 we theoretically compare the properties of a BEC with those of liquid quantum droplets on the example of superfluid ^{4}He droplets. We continue with calculations on the phase diagram of a trapped dipolar BEC and study the properties of the individual phases. Finally, we theoretically show that the quantum droplets are self-bound in three dimensions above a certain critical atom number.

In the third chapter, we introduce the element dysprosium and discuss its properties. We continue with the experimental setup and our procedure to create a degenerate gas of dysprosium. We then show our results on the measurements of the phase diagram.

There, we first identify the critical trap aspect ratio that splits the regime of the multi droplet phase from the single droplet phase. We finish the chapter measuring the critical scattering length in the multi droplet phase as a function of the trap aspect ratio.

In the last chapter, we show our measurements on the self-bound quantum droplets. We start by explaining the technique on how to create these droplets and how we image them. We investigate the survival probability that describes the probability to find a droplet after certain time of free expansion as a function of the scattering length and create a first model to analyze the transition from the dilute liquid state to the gas state. We finish with our direct measurement of the critical atom number and discuss its consequences on the knowledge of the scattering length of dysprosium.

Part I.

Theoretical Foundations

1. Dipolar Bose-Einstein condensates

In this chapter we give a brief description of the theoretical background on dipolar Bose-Einstein condensates (BECs). We start with an introduction to Bose-Einstein condensation and the two-body interactions that come into play in their realization with neutral atoms. In this context, we consider the isotropic short-range interaction that results from van-der-Waals interactions and present a method to modify the interaction strength. We continue the description with the anisotropic long-range dipole-dipole interaction. The resulting interacting BEC is further described within a mean-field approach leading to the famous Gross-Pitaevskii equation. We introduce the Gaussian and the Thomas-Fermi approximation to simplify the problem. Calculating the first correction terms to the mean-field approach finally yields an effective Gross-Pitaevskii equation.

1.1. Bose-Einstein condensation

In 1924 Bose predicted a phase where a macroscopic number of photons occupies the same quantum state [55]. This hypothesis was extended by Einstein in 1924 and 1925 for a non-interacting gas of bosons [56, 57]. In this new state of matter, nowadays called Bose-Einstein condensate (BEC), the bosons share the very same single-particle state. The discovery of superfluidity in liquid helium in 1938 by Kapitza and Allen & Misener[3, 4] is now recognized as the first evidence for Bose-Einstein condensation. They observed a vanishing viscosity below a certain λ-point. It was London in 1938 who first pointed out the connection between the superfluid state and BECs [5]. He suggested that the λ-point phase transition can be seen as Bose-Einstein condensation. In 1941 this idea was pushed forward by Landau [58] and later in the 1950s Penrose & Onsager postulated Bose-Einstein condensation to require a macroscopic phase coherence throughout the whole sample [59, 60]. Nowadays it is clear that the observed condensate fraction in superfluid helium was very low due to strong interactions.

It was 40 years later that Bose-Einstein condensation in its simplest form was actually observed due to the development of laser cooling and trapping of neutral atoms [61]. This opened up a completely new area of research since atomic samples provide a much cleaner environment than the earlier studies on liquid helium. It was Ketterle, Wieman

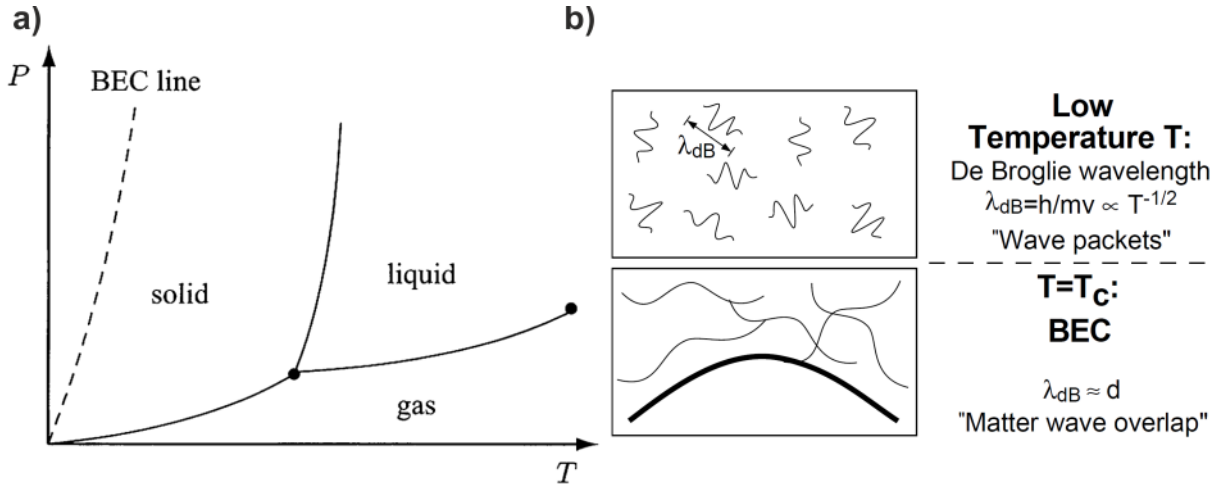

Figure 1.1.: Schematic representation of Bose-Einstein condensation: a) A Schematic $P-T$ phase diagram in thermal equilibrium. We can see that the BEC state occurs in the solid regime confirming that gaseous BECs are metastable. Taken from [63]. **b)** Visualization of a thermal gas for low temperatures that condenses at the critical temperature. The de-Broglie wavelength at $T > T_{\mathrm{C}}$ is smaller than the inter-particle spacing making them incoherent. At $T = T_{\mathrm{C}}$ the matter waves start to overlap and the particles become coherent, behaving as one macroscopic matter wave. Taken from [65].

& Cornell and Hulet in 1995 and 1997 who finally succeeded in the production of a BEC of alkali atoms [6–8, 62]. Since then several atomic species have been brought to quantum degeneracy, including more complex lanthanide atoms. In contrast to liquid helium, the interactions in these atomic systems are much weaker such that 'pure' condensates can be produced. It is important to mention that at the experimental temperatures, the ground state is actually a solid and gaseous BECs exist only in a metastable state (see figure 1.1a). The mechanism through which an ultracold gas decays to the solid state is the recombination of free atoms into molecules, which requires collisions of at least three atoms. As will be discussed in this chapter, the density of a gaseous BEC is low enough for this process to be very slow. Hence, despite being metastable, the BEC state can be observed for timescales on the order of a few seconds.

The following description of the theoretical basis of BECs is only a short insight and more details can be found in the following books [63, 64] and articles [65, 66]. The quantum mechanical phenomenon of Bose-Einstein condensation of atoms can be described as follows: We consider an ideal Bose gas of N particles confined in a volume V giving a particle density $n = N/V$. The coherence length of the particles is given by their thermal de-Broglie wavelength

$$\lambda_{\mathrm{dB}}(T) = \sqrt{\frac{2\pi\hbar^2}{m k_{\mathrm{B}} T}}, \tag{1.1}$$

with the reduced Planck constant $\hbar = h/2\pi$, the particle mass m, the Boltzmann constant k_{B} and the sample temperature T. To quantify the transition from a thermal gas to a BEC, we define the phase space density

$$\mathcal{D} = n\lambda_{\mathrm{dB}}^3. \tag{1.2}$$

In a thermal gas, the inter-particle spacing $n^{-1/3}$ is much larger than λ_{dB} leading to $\mathcal{D} \ll 1$ and the gas behaves purely classical, since the atoms are incoherent. By increasing the density as well as decreasing the temperature the phase space density reaches values close to one, indicating that wave functions of individual particles start to overlap (see figure 1.1). One would expect the BEC state to be reached for $\mathcal{D} = 1$ but the quantum mechanical calculation yields that the phase transition occurs for $\mathcal{D} > \zeta(3/2)$[1]. Here a macroscopic number of particles occupies the BEC state and we can give a critical temperature

$$k_{\mathrm{B}} T_{\mathrm{C}} = \frac{2\pi\hbar^2}{m} \left(\frac{n}{\zeta(3/2)} \right)^{2/3}. \tag{1.3}$$

Typical critical temperatures range from $T_{\mathrm{C}} \approx 50\,\mathrm{nK} - 2\,\mu\mathrm{K}$ at densities of $n \approx 10^{19} - 10^{21}\,\mathrm{m}^{-3}$.

Similar as in liquid helium, not all the atoms immediately collapse to the BEC ground state but depending on the relative temperature of the atoms, the condensate fraction is given by

$$\frac{N_{\mathrm{BEC}}}{N_{\mathrm{tot}}} = 1 - \left(\frac{T}{T_{\mathrm{C}}} \right)^3, \tag{1.4}$$

with N_{BEC} describing the atoms occupying the BEC ground state and N_{tot} the total number of atoms. As described earlier, this condition is only true in the regime where interactions are very weak.

1.2. Two-body interactions

Compared to solids, the density in an ultracold atomic gas is nine orders of magnitude smaller and thus we might expect that interactions can be neglected. Despite the dilute-ness, it has been shown that the fundamental properties of a BEC like its shape, collective oscillation frequencies or stability are determined by interactions [63, 64, 67, 68], since

[1] $\zeta(s)$ describes the Riemann zeta function.

the kinetic energy of the particles is very low.

In this section we introduce the two important interactions in a dipolar BEC. We start with the isotropic short-range contact interaction and show how to tune its interaction strength. Subsequently, we discuss the anisotropic long-range dipolar interaction.

1.2.1. Short-range contact interaction

When two atoms approach each other at separation r they feel a weak attractive force coming from electrically induced dipole-dipole interactions, known as van-der-Waals attraction that scales as $-C_6/r^6$ with the van-der-Waals coefficient C_6. At very small distances the electron orbitals start to overlap leading to strong Coulomb repulsion that scales with C_{12}/r^{12}, with C_{12} representing the strength of the electrostatic repulsion. Adding these two contributions leads to the well-known Lennard-Jones potential with a potential depth of $V(r_{\mathrm{vdW}})/k_{\mathrm{B}} \approx 10^3\,\mathrm{K}$. The characteristic interaction length r_{vdW}, also called van-der-Waals length, can be estimated using Heisenberg's uncertainty principle $\Delta p \approx \hbar/\Delta x$ with the kinetic energy $\Delta p^2/2m_{\mathrm{red}}$, where m_{red} describes the reduced mass of two particles. As they approach each other they gain kinetic energy equal to the van-der-Waals term of the molecular potential leading to $r_{\mathrm{vdW}} \approx 100\,a_0$ for typical van-der-Waals coefficients[2]. Since the de-Broglie wavelength in a BEC is typically much larger than this interaction length ($r_{\mathrm{vdW}}/\lambda_{\mathrm{dB}} \ll 1$), atoms move freely until they approach each other closer than r_{vdW} and collide elastically. In that sense it is not important to know the exact molecular potential and we can replace it with a much simpler two-body pseudo potential which yields the same scattering properties. To investigate the elastic scattering properties we consider a scattering event between two colliding atoms in the center of mass frame shown in figure 1.2a. To obtain the symmetry of the scattered wave function, we calculate which relative angular momentum states are involved. The angular momentum reads $\hbar l \simeq r_{\mathrm{imp}} m_{\mathrm{red}} v$ with the impact parameter r_{imp} and the relative velocity v. We can express the relative velocity in terms of the de-Broglie wavelength with $\lambda_{\mathrm{dB}} \simeq h/m_{\mathrm{red}}v$. A collision only happens if the impact parameter is smaller than the interaction length leading to the condition $l \leq 2\pi r_{\mathrm{vdW}}/\lambda_{\mathrm{dB}}$. With the condition mentioned earlier ($r_{\mathrm{vdW}}/\lambda_{\mathrm{dB}} \ll 1$), the only possible solution is $l = 0$ and the scattered wave function is spherically symmetric, a so-called s-wave. The resulting pseudo potential that describes an isotropic two-body

[2] With $\Delta p^2/2m_{\mathrm{red}} = C_6/r_{\mathrm{vdW}}^6$ and $\Delta x = r_{\mathrm{vdW}}$ the interaction length is given by $r_{\mathrm{vdW}} = (2m_{\mathrm{red}}C_6/\hbar^2)^{1/4}$. For Dysprosium, $C_6^{\mathrm{Dy}} = 2003\,E_{\mathrm{h}}\,a_0^6$ [51] and the Hartree energy $E_{\mathrm{h}} = 4.360\times10^{-18}\,\mathrm{J}$ we obtain $r_{\mathrm{vdW}}^{\mathrm{Dy}} = 156\,a_0$.

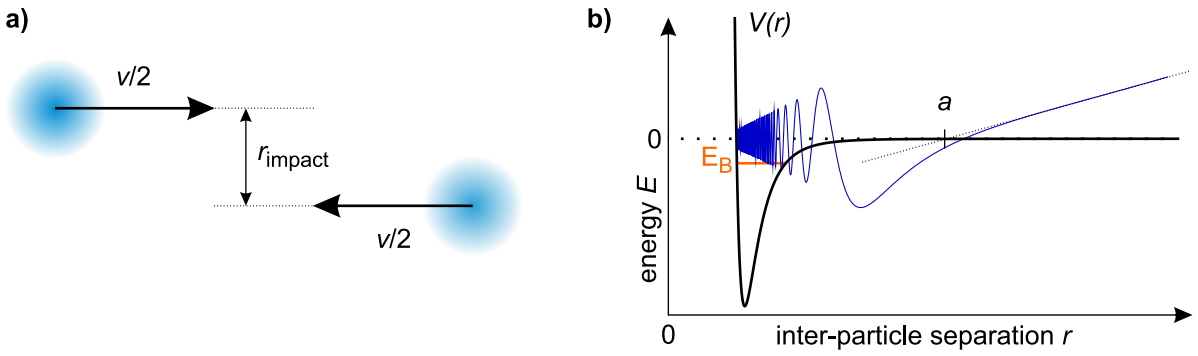

Figure 1.2.: Elastic scattering problem of two neutral atoms: a) The center of mass frame of two colliding particles with relative velocity v and impact parameter r_{imp}. **b)** The molecular potential $V(|\boldsymbol{r}|)$ as a function of the inter-particle distance r. The orange line shows the last molecular bound state that determines the wave function $\psi(r)$, illustrated as blue line. The scattering length a is determined by an extrapolation of the asymptotic regime at $r \gg r_{\mathrm{vdW}}$. Adapted from [69].

short-range interaction is given by

$$V_{\mathrm{contact}} = g\delta(\boldsymbol{r}) = \frac{4\pi\hbar^2 a}{m}\delta(\boldsymbol{r}) \tag{1.5}$$

with the Dirac delta distribution $\delta(\boldsymbol{r})$ and the contact interaction strength g that depends on the s-wave scattering length a and the particle mass m. In this context a positive (negative) scattering length corresponds to a repulsive (attractive) potential. An important consequence of this pseudo potential is that a scattering event of two atoms is fully described by a single parameter, the scattering length a. An interpretation at the real molecular potential $V(\boldsymbol{r})$ is shown in figure 1.2b and can be found in [63]. The wave function ψ of the scattered particles shows an asymptotic behavior at very large distances $r > r_{\mathrm{vdW}}$. Intercepting this asymptote with the r-axis leads to the scattering length a that can take positive and negative values. Such a molecular potential typically possesses a number of bound states. The form of ψ and consequently the value of a is determined by the position of the last bound state in the molecular potential as ψ couples to this state. When the scattered particles approach each other on very short distances ($r \leq r_{\mathrm{vdW}}$), the wave function shows fast oscillations and is finally being reflected by the C_{12}/r^{12} part of the potential.

1.2.2. Manipulation of the contact interaction strength: A Feshbach resonance

Since the scattering properties are only described by the scattering length a it is very useful to be able to change this parameter. Tuning the interactions indeed allows to get a deeper understanding of their effect and how they induce correlations between particles. It is possible to tune the molecular bound state using electric fields [70], but the required field strength is very high and difficult to implement in a standard vacuum apparatus. In cold atomic experiments Feshbach resonances (FRs) are used. First theoretical studies on FRs were done by Feshbach in 1958 in the context of nuclear physics [71] and later on brought into the context of atomic physics [72] by Fano in 1961. Up to now different types of FRs have been used to modify ultracold quantum systems, including magnetic FRs [11], optical FRs [73, 74] and orbital FRs [75]. Here, we will focus on magnetic FRs, although all types exhibit the same basic principles.

In section 1.2.1 we introduced the molecular potential for two atoms approaching each other. Due to the internal structure of atoms there is a manifold of molecular potentials, each one with different quantum numbers. To explain the properties of a FR we take into account two potentials, the so-called open and closed channels, shown in figure 1.3. The second potential is called closed channel as the kinetic energy of the incoming particles ($E \approx 0$) is lower than the channels potential energy for large interparticle distances r. Nevertheless, if the closed channel has a bound state with energy $E_\mathrm{c} = E$, resonant coupling leads to a strong mixing between open and closed channel and a very weakly-bound and short-lived diatomic molecule is formed. This effect is called a FR and leads to a divergence of the scattering length as shown in figure 1.3b. The width ΔB of such a FR is given by the coupling strength between closed and open channel. If the magnetic moment between the closed and the open channel is different, the energy difference ΔE, respectively E_c, can be tuned due to the different Zeeman shift using magnetic fields. In the limit of low temperatures or small kinetic energies, this allows complete tuning of a between $(-\infty, \infty)$ described by

$$a(B) = a_\mathrm{BG}\left(1 - \frac{\Delta B}{B - B_0}\right), \tag{1.6}$$

with the background scattering length a_BG and the position of the FR B_0.

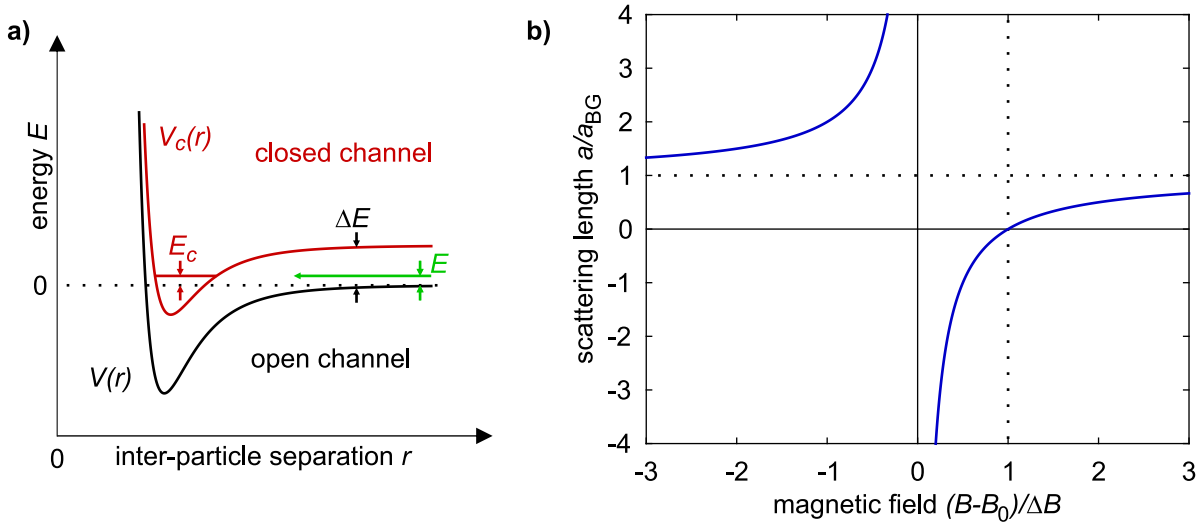

Figure 1.3.: Feshbach Resonance: a) We show two molecular potentials, the open and the closed channel. A Feshbach resonance occurs when the energy of a bound state E_c of the closed channel is equal to the kinetic energy of the incoming particles E. The energy difference ΔE between closed and open channel, and thereby the bound state E_c relative to E, can be tuned by external magnetic fields. **b)** We show the dependence of the scattering length in units of the background scattering length a_{BG} as a function of the magnetic field in units of the width of the FR ΔB. At the position of the FR B_0 the scattering length diverges according to equation (1.6). The vertical dotted line indicates ΔB and shows that a goes through a zero-crossing here. The horizontal dotted line shows a_{BG} as asymptote for magnetic field values far away from any FRs.

1.2.3. Long-range dipolar interaction

In ultracold dipolar gases the atoms do not only feel the van-der-Waals, but also a dipole-dipole interaction. It arises due to the natural interaction that exists between magnetic dipoles. The first dipolar condensate has been produced from chromium atoms in 2005 [25] as they possess a strong magnetic dipole moment of $\mu_m = 6\,\mu_B$, with the Bohr magneton μ_B. Since then the dipolar community grew and atoms with an even stronger magnetic moment, erbium [46] and dysprosium [44] with $7\,\mu_B$ and $10\,\mu_B$ respectively, have been studied. In the following we will describe the properties of the dipolar interaction. A more detailed insight in the topic of ultracold dipolar systems can be found in [28].

In the following description, we assume an external magnetic field that is sufficiently strong to polarize the atomic cloud. In this situation, two aligned dipoles feel the dipole-dipole interaction potential

$$V_{dd}(\boldsymbol{r}, \vartheta) = \frac{\mu_0 \mu_m^2}{4\pi} \frac{1 - 3\cos^2\vartheta}{r^3}, \tag{1.7}$$

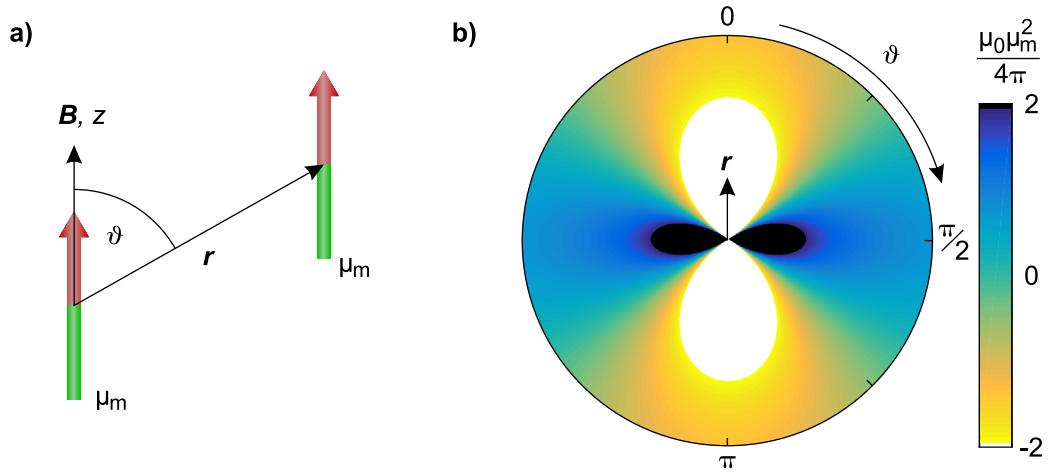

Figure 1.4.: Dipole-Dipole Interaction: a) A schematic drawing of the dipole-dipole interaction for two dipoles with magnetic moment μ_m aligned by a magnetic field $\boldsymbol{B}$ along the z-direction. They are separated from each other by the vector $\boldsymbol{r}$ at an angle $\vartheta = \sphericalangle(\boldsymbol{r}, \boldsymbol{B})$. **b)** The dipolar interaction potential is plotted against the distance r and the angle ϑ. The interaction strength is given in units of $\mu_0\mu_\mathrm{m}^2/4\pi$ and capped at ± 2. Attraction is indicated as bright colors (light green to white), while repulsion is shown for dark colors (cyan to black). At the magic angle of $\vartheta \approx 55\,^\circ$ the interaction strength is zero, shown in green.

with the vacuum permeability μ_0 and the angle ϑ between the direction of polarization and the relative position of the dipoles $\boldsymbol{r}$. This potential has two main features in its anisotropy and its long-range character. The anisotropy can be seen from the angle dependence and leads to an attractive force for $\vartheta = 0$ (head-to-tail configuration) and a repulsive force for $\vartheta = \pi/2$ (side-by-side configuration). The long-range character comes from the r^{-3} dependence[3]. Due to its long-range character the potential cannot be replaced by a simple Dirac delta potential [28].

In the description of dipolar systems, it is useful to introduce various parameters that quantify the dipolar interaction strength. Similar to the contact interaction, where we introduced the scattering length a, we define the characteristic dipolar length as

$$a_\mathrm{dd} = \frac{\mu_0\mu_\mathrm{m}^2 m}{12\pi\hbar^2}, \tag{1.8}$$

as well as the dipolar coupling strength as

$$g_\mathrm{dd} = \frac{4\pi\hbar^2 a_\mathrm{dd}}{m} = \frac{\mu_0\mu_\mathrm{m}^2}{3}. \tag{1.9}$$

[3]We use the definition of [76] that the potential is short-range if it decays faster than r^{-D} for D dimensions. Following this definition, the dipole-dipole interaction potential is long-range in 3D, while in 1D and 2D it is short-range.

These definitions are chosen in a way that a homogeneous, three dimensional BEC becomes unstable for $a_{\mathrm{dd}} \geq a$. We need to stress here, that a_{dd} does not correspond to a finite interaction radius, as is the case for the contact interaction a. Finally, to compare the two interactions we define the relative dipolar strength as

$$\varepsilon_{\mathrm{dd}} = \frac{g_{\mathrm{dd}}}{g} = \frac{a_{\mathrm{dd}}}{a} = \frac{\mu_0 \mu_{\mathrm{m}}^2 m}{12\pi\hbar^2 a}. \tag{1.10}$$

For a BEC to be dominated by dipolar effects, the dipolar interaction needs to be at least as strong as the contact interaction giving $\varepsilon_{\mathrm{dd}} \geq 1$.

We can write the resulting interaction potential for a dipolar quantum gas as

$$V_{\mathrm{int}}(\boldsymbol{r}) = g\delta(\boldsymbol{r}) + \frac{3}{4\pi} g_{\mathrm{dd}} \frac{1 - 3\cos^2\vartheta}{r^3}. \tag{1.11}$$

Note, that eq. (1.11) results from a simple addition of the short-range part of the potential arising from van-der-Waals interactions, and the long-range dipole-dipole interaction. In principle, the scattering problem must be solved in the complete potential, and as a consequence a coupling between the two parts should exist. It has been shown that in the limit of weak dipolar interaction, one can apply the so-called first-order Born approximation [77] and eq. (1.11) is correct[4]. However, for a dipolar interaction strength on the order of the contact interaction ($\varepsilon_{\mathrm{dd}} \sim 1-2$), corrections to the Born approximation exist [78]. We will see that, although the results described in this thesis use eq. (1.11), these corrections must be taken into account for further studies.

1.3. Theoretical description of a trapped dipolar condensate

In the previous section we introduced the interaction potentials for two colliding dipolar atoms within the first-order Born approximation. In this section we will discuss the necessary theory to describe the many-body problem of an interacting BEC starting with a mean-field description that leads to the so-called Gross-Pitaevskii equation. We continue with the Gaussian variational ansatz for a non-interacting BEC, followed by the Thomas-Fermi approximation for an interacting BEC. We finish this section with the first beyond mean-field correction term, which originates from quantum fluctuations around the mean-field value.

[4] In this case, the scattering length is modified by the presence of the dipolar interaction, but eq. (1.11) is still correct with this modified a.

1.3.1. Mean-field treatment: Gross-Pitaevskii equation

To theoretically tackle the problem of many interacting particles we first use the so-called mean-field ansatz. This means that each particle will see an effective potential that is build up by all other particle interactions. We write the many-body Hamiltonian in second quantization that describes N interacting bosons confined in an external potential V_{ext} as

$$\begin{aligned}\hat{\mathcal{H}} = &\int \mathrm{d}^3 r\, \hat{\Psi}^\dagger(\boldsymbol{r}) \left(-\frac{\hbar^2}{2m}\nabla^2 + V_{\text{ext}}(\boldsymbol{r})\right) \hat{\Psi}(\boldsymbol{r}) \\ &+\frac{1}{2}\int \mathrm{d}^3 r\, \mathrm{d}^3 r'\, \hat{\Psi}^\dagger(\boldsymbol{r})\hat{\Psi}^\dagger(\boldsymbol{r}')V_{\text{int}}(\boldsymbol{r}-\boldsymbol{r}')\hat{\Psi}(\boldsymbol{r}')\hat{\Psi}(\boldsymbol{r}),\end{aligned} \tag{1.12}$$

with the boson field operator $\hat{\Psi}(\boldsymbol{r})$ ($\hat{\Psi}^\dagger(\boldsymbol{r})$) that annihilates (creates) a particle at position $\boldsymbol{r}$ and the two-body interaction potential from eq. (1.11). The field operators fulfill the normalization $N = \int \mathrm{d}^3 r \langle \hat{\Psi}^\dagger(\boldsymbol{r})\hat{\Psi}(\boldsymbol{r})\rangle$ with the expectation value denoted as angle brackets. Using the Heisenberg representation [66] given by

$$\begin{aligned} i\hbar\frac{\partial}{\partial t}\hat{\Psi}(\boldsymbol{r},t) &= \left[\hat{\Psi}(\boldsymbol{r},t), \hat{\mathcal{H}}\right] \\ &= \left(-\frac{\hbar^2}{2m}\nabla^2 + V_{\text{ext}}(\boldsymbol{r}) + \int \mathrm{d}^3 r' \hat{\Psi}^\dagger(\boldsymbol{r}',t)V_{\text{int}}(\boldsymbol{r}-\boldsymbol{r}')\hat{\Psi}(\boldsymbol{r}',t)\right)\hat{\Psi}(\boldsymbol{r},t),\end{aligned} \tag{1.13}$$

the boson field operators become time dependent. We can decompose the boson field operators into the mainly occupied condensate wave function Ψ plus a small perturbation $\delta\hat{\Psi}$ as

$$\hat{\Psi}(\boldsymbol{r},t) = \Psi(\boldsymbol{r},t) + \delta\hat{\Psi}(\boldsymbol{r},t). \tag{1.14}$$

This perturbation, also called quantum fluctuations, is crucial to explain the results reported in this thesis and will be treated in section 1.3.3. For now we will neglect them, setting $\langle\delta\hat{\Psi}(\boldsymbol{r},t)\rangle = 0$, so that the complex number $\Psi(\boldsymbol{r},t)$ coincides with the mean value of the field. It has been shown that basic properties of a condensate can be fully described in this mean-field approach. Inserting eq. (1.14) into eq. (1.13) leads to the non-local, time-dependent Gross-Pitaevskii equation

$$i\hbar\frac{\partial}{\partial t}\Psi(\boldsymbol{r},t) = \left(-\frac{\hbar^2}{2m}\nabla^2 + V_{\text{ext}}(\boldsymbol{r}) + gn(\boldsymbol{r},t) + \int \mathrm{d}^3 r' V_{\text{dd}}(\boldsymbol{r}-\boldsymbol{r}')n(\boldsymbol{r}',t)\right)\Psi(\boldsymbol{r},t). \tag{1.15}$$

with the density of the condensate $n(\boldsymbol{r},t) = |\Psi(\boldsymbol{r},t)|^2$. Using the ansatz that the wave function can be described as $\Psi(\boldsymbol{r},t) = \psi(\boldsymbol{r})\exp(-i\mu t/\hbar)$, with μ being the chemical

potential, we can separate off the time dependence and end up with the stationary GPE

$$\mu\psi(\boldsymbol{r}) = \left(-\frac{\hbar^2}{2m}\nabla^2 + V_{\text{ext}}(\boldsymbol{r}) + \Phi_{\text{contact}}(\boldsymbol{r}) + \Phi_{\text{dd}}(\boldsymbol{r})\right)\psi(\boldsymbol{r}), \tag{1.16}$$

and define the mean-field potentials of the contact interaction $\Phi_{\text{contact}}(\boldsymbol{r}) = gn(\boldsymbol{r})$ and dipolar interaction $\Phi_{\text{dd}}(\boldsymbol{r}) = \int \mathrm{d}^3r' V_{\text{dd}}(\boldsymbol{r}-\boldsymbol{r}')n(\boldsymbol{r}')$. To calculate ground state properties of the condensate we use a variational ansatz and derive the energy functional to be

$$E(n,\boldsymbol{r}) = \int \mathrm{d}^3r \left(\frac{\hbar^2}{2m}\nabla^2 + V_{\text{ext}}(\boldsymbol{r}) + \frac{\Phi_{\text{contact}} + \Phi_{\text{dd}}}{2}\right) n(\boldsymbol{r}), \tag{1.17}$$

where we identify the first term as the kinetic energy, the second term as external potential (or harmonic oscillator) energy and the last term as the interaction energy, which is the sum of contact and dipolar interaction. In the next section we will describe two analytical methods to minimize the energy functional using different trial density functions.

1.3.2. Gaussian variational ansatz and Thomas-Fermi approximation

In ultracold atomic gases, the atoms have to be trapped in an external potential V_{ext}. In the results that we present in this thesis, atoms are trapped in anisotropic harmonic traps described by the three-dimensional harmonic oscillator potential

$$V_{\text{ext}} = \frac{m}{2}(\omega_x^2x^2 + \omega_y^2y^2 + \omega_z^2z^2), \tag{1.18}$$

with the trap frequencies $\omega_{x,y,z}$. The trapping leads to an inhomogeneous density distribution, described in the following.

Gaussian variational ansatz

The Gaussian variational ansatz can be used to obtain semi-analytical solutions to equation (1.17). While the solutions coincide with the exact ground state in the regime of zero interactions, they will be close to the exact solutions including interactions when the kinetic energy dominates. For simplicity we start with a non-interacting BEC and insert eq. (1.18) into eq. (1.16) resulting in the well-known three-dimensional quantum-mechanical harmonic oscillator

$$\mu\psi(\boldsymbol{r}) = \left(-\frac{\hbar^2}{2m}\nabla^2 + \frac{m}{2}\left(\omega_x^2x^2 + \omega_y^2y^2 + \omega_z^2z^2\right)\right)\psi(\boldsymbol{r}). \tag{1.19}$$

As stated before, the wave function fulfills the normalization condition $N = \int d^3r|\psi(\boldsymbol{r})|^2$. In general, the solutions are given by the Hermite functions and the ground-state wave function is a Gaussian:

$$\psi(\boldsymbol{r}) = \sqrt{\frac{N}{\pi^{3/2}a_x a_y a_z}} \exp\left(-\frac{x^2}{2a_x^2} - \frac{y^2}{2a_y^2} - \frac{z^2}{2a_z^2}\right), \tag{1.20}$$

with the harmonic oscillator length $a_{x,y,z} = \sqrt{\hbar/m\omega_{x,y,z}}$ giving a characteristic harmonic oscillator length of $\bar{a} = (a_x a_y a_z)^{1/3} = \sqrt{\hbar/m\bar{\omega}}$ with the geometric mean of the trap frequencies $\bar{\omega} = (\omega_x\omega_y\omega_z)^{1/3}$. Replacing the harmonic oscillator length with a Gaussian width $\sigma_{x,y,z}$ as variational parameter, we find the density distribution

$$n(\boldsymbol{r}) = n_0 \exp\left(-\frac{x^2}{\sigma_x^2} - \frac{y^2}{\sigma_y^2} - \frac{z^2}{\sigma_z^2}\right), \tag{1.21}$$

with the central density $n_0 = N/(\pi^{3/2}\sigma_x\sigma_y\sigma_z)$. Although interactions are neglected, this ansatz allows the study of stationary as well dynamic properties of non-dipolar BECs [79, 80].

Thomas-Fermi approximation for contact interaction

Another way to find semi-analytical solutions is to neglect terms in eq. (1.17). For example, the Thomas-Fermi approximation neglects the kinetic energy term. This approximation is valid for a large atom number N with sufficiently high densities. In this case, the interaction terms in eq. (1.16) dominate over the kinetic energy and we can simplify the GPE for a non-dipolar BEC to

$$\mu\psi(\boldsymbol{r}) = \left(\frac{m}{2}\left(\omega_x^2x^2 + \omega_y^2y^2 + \omega_z^2z^2\right) + gn(\boldsymbol{r})\right)\psi(\boldsymbol{r}). \tag{1.22}$$

We can analytically solve this equation and end up with the well-known parabolic density distribution for a BEC with contact interaction given as

$$n(\boldsymbol{r}) = n_0 \max\left\{\left(1 - \frac{x^2}{R_x^2} - \frac{y^2}{R_y^2} - \frac{z^2}{R_z^2}\right), 0\right\}, \tag{1.23}$$

with the central density $n_0 = 15N/(8\pi R_x R_y R_z)$ and the Thomas-Fermi radii $R_{x,y,z} = \sqrt{2\mu/(m\omega_{x,y,z}^2)}$. Due to the normalization, we can express the chemical potential as a

function of the atom number as [66]

$$\mu = \frac{\hbar\bar{\omega}}{2}\left(\frac{15Na}{\bar{a}}\right)^{2/5}, \tag{1.24}$$

leading to a Thomas-Fermi radius of

$$R_{x,y,z} = 15^{1/5}\left(\frac{Na}{\bar{a}}\right)^{1/5}\frac{\bar{\omega}}{\omega_{x,y,z}}\bar{a}. \tag{1.25}$$

We can see that the Thomas-Fermi radii are only significantly larger than the harmonic oscillator length $\bar{a}$ if the condition $Na/\bar{a} \gg 1$ is fulfilled. Consequently, we can define this condition as a validity condition for the Thomas-Fermi approximation.

Thomas-Fermi approximation for dipolar interactions

Due to the non-local character of the dipole-dipole interaction, the description of a BEC using the Thomas-Fermi approximation becomes significantly more complicated. Nevertheless, it was shown that even in the presence of the dipole-dipole interaction, the Thomas-Fermi approximation results in an inverted parabola density distribution [81, 82]. However, the effect of the dipolar interaction is a distortion of this parabola along the magnetic field as we will show below. For simplicity we will consider a cylindrically symmetric trap ($\omega_x = \omega_y = \omega_\rho$) with the polarization axis aligned along the z-direction with trap frequency ω_z. With this we define a trap aspect ratio $\lambda = \omega_z/\omega_\rho$. As a first step, we assume that the dipolar interaction is weak and the density profile of the BEC still resembles an inverted parabola. In analogy to the trap aspect ratio we can define a cloud aspect ratio for the BEC with $\kappa = R_\rho/R_z$ using the Thomas-Fermi radii observed in eq. (1.25). The dipoles generate the following mean-field potential [81, 82]

$$\Phi_{\mathrm{dd}}(\boldsymbol{r}) = n_0 g_{\mathrm{dd}}\left\{\frac{\rho^2}{R_\rho^2} - \frac{2z^2}{R_z^2} - f_{\mathrm{dip}}(\kappa)\left(1 - \frac{3}{2}\frac{\rho^2 - 2z^2}{R_\rho^2 - R_z^2}\right)\right\}, \tag{1.26}$$

with the dipolar anisotropic function

$$f_{\mathrm{dip}}(\kappa) = \frac{1+2\kappa^2}{1-\kappa^2} - \frac{3\kappa^2 \mathrm{artanh}\left(\sqrt{1-\kappa^2}\right)}{(1-\kappa^2)^{3/2}}, \tag{1.27}$$

that decreases monotonically with increasing κ and changes sign at $\kappa = 1$, shown in figure 1.5a. We can see that ρ and z appear either constant or quadratic in eq. (1.26). Consequently, the density distribution for a dipolar condensate in Thomas-Fermi approximation

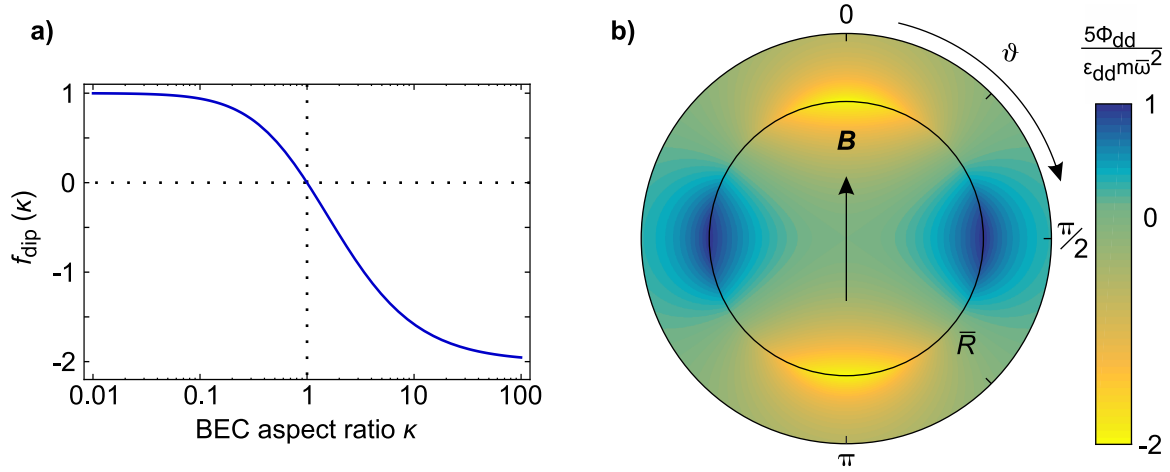

Figure 1.5.: Dipolar mean-field potential: a) Dipolar anisotropic function f_{dip} as a function of the BEC aspect ratio κ. For $\kappa < 1$, the BEC exhibits a prolate (cigar) shape and the anisotropic function is positive with $f_{\mathrm{dip}} = 1$ for $\kappa \to 0$. f_{dip} becomes zero for a round BEC and approaches $f_{\mathrm{dip}} = -2$ for $\kappa \to \infty$, where the BEC has an oblate (pancake) shape. **b)** The dipolar mean-field potential for $\kappa = 1$ with Thomas Fermi radius $\bar{R}$. It represents a saddle-like shaped potential that is attractive along the magnetic field direction and repulsive perpendicular to it.

still resembles an inverted parabola. However, the Thomas-Fermi radii now depend on both the contact interaction strength g and the dipolar interaction strength g_{dd} and are given by

$$R_\rho = \left[\frac{15N\kappa}{4\pi m\omega_\rho^2}\left\{g + g_{\mathrm{dd}}\left(\frac{3}{2}\frac{\kappa^2 f_{\mathrm{dip}}(\kappa)}{1-\kappa^2} - 1\right)\right\}\right]^{1/5}, \tag{1.28}$$

and $R_z = R_\rho/\kappa$. The BEC aspect ratio κ has to be determined by solving the transcendental equation

$$\lambda = \kappa\left(\frac{1 + 2\varepsilon_{\mathrm{dd}} - \frac{3\varepsilon_{\mathrm{dd}} f_{\mathrm{dip}}(\kappa)}{1-\kappa^2}}{1 - \varepsilon_{\mathrm{dd}} + \frac{\kappa^2}{2}\frac{3\varepsilon_{\mathrm{dd}} f_{\mathrm{dip}}(\kappa)}{1-\kappa^2}}\right)^{1/2}. \tag{1.29}$$

The deformation of the condensate with respect to the trap aspect ratio is known as magnetostriction and was first observed in a chromium BEC [26]. The magnetostriction effect can be understood when we have a closer look at the dipolar mean-field potential in eq. (1.26). If we consider a spherically symmetric trap ($\lambda = 1$) with trap frequency $\bar{\omega}$ and weak dipolar interaction such that the BEC is nearly spherical with Thomas-Fermi radii $\bar{R}$, we can simplify eq. (1.26) to

$$\Phi_{\mathrm{dd}}(\boldsymbol{r}) = \varepsilon_{\mathrm{dd}}\frac{m\bar{\omega}^2}{5}(1 - 3\cos^2\vartheta)\begin{cases} r^2, & \text{for} \quad r \le \bar{R} \\ \frac{\bar{R}^5}{r^3}, & \text{for} \quad r > \bar{R} \end{cases}. \tag{1.30}$$

The resulting saddle-shaped potential that is attractive along the magnetic field orientation and repulsive perpendicular to it is shown in figure 1.5b. Consequently, a dipolar BEC becomes elongated along the magnetic field orientation. Calculating the energy density for a dipolar BEC in Thomas-Fermi approximation yields

$$\frac{E_{\text{int}}}{V} = \frac{gn^2}{2}(1 - \varepsilon_{\text{dd}} f_{\text{dip}}(\kappa)). \tag{1.31}$$

From this equation, and the fact that $f_{\text{dip}}(\kappa)$ is a monotonous function, it is also obvious that to minimize its energy, the condensate will minimize κ, leading to magnetostriction.

1.3.3. Beyond mean-field correction: Quantum fluctuations

The mean-field approach, although sufficient to describe most properties of weakly interacting gases, fails to describe the results that we present in this thesis. This can be seen when having a closer look at eq. (1.31), showing that a dipolar BEC with $\varepsilon_{\text{dd}} > 1$ in a prolate shape causes its energy density to become negative. Minimizing the energy in this case is done by an ever increasing density, leading to a collapse. On the contrary, our experimental observations have shown that a dipolar BEC restabilizes in so-called quantum droplets [52, 54], which are the main subject of this thesis. For this reason, in this section we will have a closer look at the quantum fluctuations that were introduced in eq. (1.14).

In 1957, Lee, Huang and Yang calculated a correction term to the energy arising from quantum fluctuations in the case of a gas with purely contact interaction [83, 84]. In brief, taking into account quantum fluctuations around the mean-field value in eq. (1.14) allows us to diagonalize the Hamiltonian with the Bogolyubov method [85]. We then obtain an energy that is given by the population of each mode, plus the vacuum energy in each of these modes [63, chp.5.7]

$$\hat{\mathcal{H}} = \sum_{\boldsymbol{p}} \varepsilon_{\boldsymbol{p}} \hat{b}^\dagger_{\boldsymbol{p}} \hat{b}_{\boldsymbol{p}} + E_0. \tag{1.32}$$

Here, the ground state is defined by the absence of excitation and its energy is simply E_0. In this case, we recover the mean-field expression, plus a correction. The beyond mean-field correction can thus be seen as arising from the zero-point motion of the collective modes of the condensate. An extension to dipolar quantum gases was calculated in 2011/2012 by Lima and Pelster [86, 87] within the local-density approximation for a trapped inhomogeneous gas resulting in the energy density [88]

$$\frac{E_{\text{QF}}}{V} = \frac{64}{15} gn^2 \sqrt{\frac{na^3}{\pi}} F_5(\varepsilon_{\text{dd}}), \tag{1.33}$$

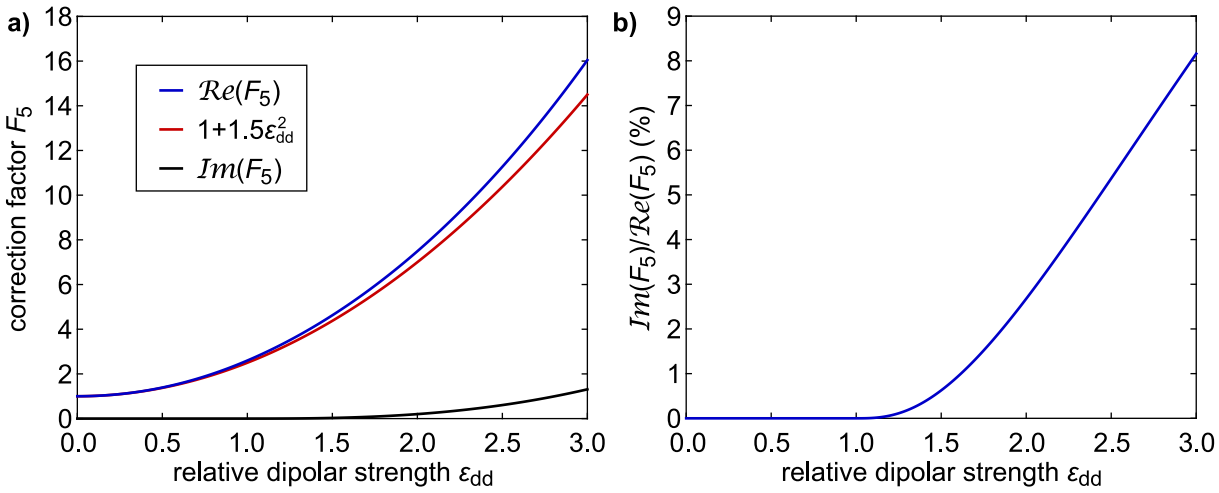

Figure 1.6.: Correction factor: a) We plot real (blue line) and imaginary part (black line) of the correction factor $F_5(\varepsilon_{\mathrm{dd}})$ from eq. (1.34) as a function of the relative dipolar strength. We see that the function is purely real up to $\varepsilon_{\mathrm{dd}} = 1$ and a small imaginary part appears for $\varepsilon_{\mathrm{dd}} > 1$. For comparison, we plot the second order Taylor expansion $1+1.5\varepsilon_{\mathrm{dd}}^2$ of F_5, which we use in simulations of our experiments. **b)** We plot the imaginary part divided by the real part of F_5 against the relative dipolar strength. We see that starting from $\varepsilon_{\mathrm{dd}} = 1.5$ the proportion increases linearly with $\varepsilon_{\mathrm{dd}}$ but does not exceed 10 % for $\varepsilon_{\mathrm{dd}} < 3$.

with the correction factor[5] $F_l(\varepsilon_{\mathrm{dd}})$ that is defined as

$$F_l(\varepsilon_{\mathrm{dd}}) = \frac{1}{2}\int \mathrm{d}\theta_k \sin\theta_k \left(1+\varepsilon_{\mathrm{dd}}(3\cos^2\theta_k - 1)\right)^{l/2}. \tag{1.34}$$

We can see that this correction is negligible in the case of very weak contact interaction or low densities ($na^3 \to 0$). The dipolar part is purely real only for $\varepsilon_{\mathrm{dd}} < 1$, however the imaginary part remains less than 10 % of its real part for $\varepsilon_{\mathrm{dd}} \leq 3$ as can be seen in figure 1.6. We can also calculate the fraction of the BEC that gets expelled from the ground state due to these quantum fluctuations. This so called condensate depletion reads

$$\frac{N-N_0}{N} = \frac{8}{3\sqrt{\pi}}\sqrt{na^3}F_3(\varepsilon_{\mathrm{dd}}). \tag{1.35}$$

[5]For simplicity, we can approximate F_5 using a Taylor expansion as $F_5(\varepsilon_{\mathrm{dd}}) \approx 1+1.5\varepsilon_{\mathrm{dd}}^2$. We use this approximation throughout this thesis.

1.3.4. Effective Gross-Pitaevskii equation

We now expand the Gross-Pitaevskii equation (1.15) by the quantum fluctuations yielding

$$i\hbar\frac{\partial}{\partial t}\Psi(\boldsymbol{r},t) = \Bigg\{ -\frac{\hbar^2}{2m}\nabla^2 + V_{\text{ext}}(\boldsymbol{r}) + gn(\boldsymbol{r},t) + \int \mathrm{d}^3r' V_{\text{dd}}(\boldsymbol{r}-\boldsymbol{r}')n(\boldsymbol{r}',t) + \frac{32g\sqrt{a^3}}{3\sqrt{\pi}}\left(1+\frac{3}{2}\varepsilon_{\text{dd}}^2\right)|\Psi(\boldsymbol{r},t)|^3\Bigg\}\Psi(\boldsymbol{r},t). \tag{1.36}$$

From this we can calculate an energy functional that reads

$$E(n,\boldsymbol{r}) = \int \mathrm{d}^3r \left(\frac{\hbar^2}{2m}\nabla^2 + V_{\text{ext}}(\boldsymbol{r}) + \frac{\Phi_{\text{contact}}+\Phi_{\text{dd}}}{2} + \frac{64}{15}gn\sqrt{\frac{na^3}{\pi}}F_5(\varepsilon_{\text{dd}})\right)n. \tag{1.37}$$

First of all we see that we indeed recover the mean-field energy of the ground state, plus the correction from equation (1.33). Using equation (1.37), we calculate the ground state properties of a dipolar BEC within a Gaussian variational ansatz using the trial function (1.21). Here, we assume a cylindrical symmetric trap recalling the trap aspect ratio $\lambda = \omega_z/\omega_\rho$. The contributing energy terms read [87, 89]

$$\begin{aligned}
\frac{E_{\text{kin}}}{\hbar\bar{\omega}} &= \frac{N\bar{a}^2}{4}\left(\frac{2}{\sigma_\rho^2}+\frac{1}{\sigma_z^2}\right),\\
\frac{E_{\text{ext}}}{\hbar\bar{\omega}} &= \frac{N}{4\bar{a}^2\lambda^{2/3}}\left(2\sigma_\rho^2+\lambda^2\sigma_z^2\right),\\
\frac{E_{\text{contact+dd}}}{\hbar\bar{\omega}} &= \frac{N^2}{\sqrt{2\pi}}\frac{\bar{a}^2 a}{\sigma_\rho^2\sigma_z}\left(1-\varepsilon_{\text{dd}}f_{\text{dip}}(\kappa)\right),\\
\frac{E_{\text{qf}}}{\hbar\bar{\omega}} &= \frac{512\sqrt{2}}{75\sqrt{5}\pi^{7/4}}\left(\frac{Na}{\bar{a}}\right)^{5/2}\left(\frac{\bar{a}^3}{\sigma_\rho^2\sigma_z}\right)^{3/2}F_5(\varepsilon_{\text{dd}}),
\end{aligned} \tag{1.38}$$

being the kinetic energy, the potential energy, the contact and dipolar interaction energy and the quantum fluctuation energy, respectively.

In addition, we perform simulations on a three-dimensional grid using a split-step Fourier method [88, 90]. To do so, we first calculate the ground state via imaginary time evolution and use this ground state to obtain dynamic properties via real-time evolution. A detailed discussion about this method can be found in reference [91]. Throughout the thesis, we will compare our experimental findings with simulations using our experimental conditions.

2. Theory of quantum droplets

Interacting atomic Bose-Einstein condensates, although exhibiting hydrodynamic behavior and superfluidity, remain in a gaseous phase. Due to their diluteness, they constitute a low density case of quantum fluids, as described in the previous chapter. Another finite-sized quantum fluid, a high density case, is the one of a quantum liquid or quantum droplets. Can we bridge the gap between these two cases is a question that we want to answer in this chapter.

Thus, we start this chapter comparing the properties of BECs to those of quantum droplets, specifically those formed from liquid ^{4}He. We continue by calculating the stability diagram for a dipolar BEC using an effective Gross-Pitaevskii equation. From these calculations we distinguish two mechanisms for the transition between a gaseous BEC to a liquid droplet which results either in the creation of multiple droplets or a single droplet. Through the analysis of the stability, we identify the mentioned new liquid phase that essentially bridges the gap between the two described systems. In the last part we discuss the possibility of creating self-bound quantum droplets from this new liquid and study its properties.

2.1. From Bose-Einstein condensates to quantum droplets

The theory of Bose-Einstein condensation has been discussed in the previous section. In this section, we want to stress some specific properties of BECs and compare them to properties of quantum droplets, considering the example of liquid ^{4}He. To do so, we first overview the theory of helium droplets, which is described in more details in reference [92]. In the case of liquid ^{4}He droplets, the density is eight orders of magnitude larger than that of a typical BEC. The atoms in these droplets are also strongly interacting with each other leading to $na^3 \sim 1$. Having such strong quantum correlations, we cannot describe a droplet by a mean-field approach. At this point, we can for example use a microscopic theory [17, chp.3] that either relies on stochastic Monte Carlo simulations [93] or on non-stochastic approaches [94]. Here, we want to start from a more macroscopic view using

an effective density functional approach [95]. At zero temperature, the energy can be expressed by the particle density $n(\boldsymbol{r})$ as [96]

$$E(n,\boldsymbol{r}) = E_{\mathrm{c}}(n,\boldsymbol{r}) + \int d\boldsymbol{r}\left(\frac{\hbar^2}{2m}\left|\nabla\sqrt{n(\boldsymbol{r})}\right|^2 + nV_{\mathrm{ext}}(\boldsymbol{r})\right). \tag{2.1}$$

This is the natural generalization of the Gross-Pitaevskii functional (eq. 1.17) with the correlation energy

$$E_{\mathrm{c}}(n,\boldsymbol{r}) = \int d\boldsymbol{r}\left(\frac{b}{2}n^2 + \frac{c}{2}n^{2+\gamma} + d(\nabla n)^2\right), \tag{2.2}$$

with the phenomenological parameters b, c and γ to reproduce the ground state energy, the density, and the compressibility, while d adjusts the surface tension. Comparing eq. (2.1) with eq. (1.37) we find a lot of similarities. In the case of a dilute BEC, eq. (1.37) is also an effective functional as we inserted the quantum fluctuations term in the mean-field functional, thus ignoring the quantum depletion. However, as opposed to eq. (2.1), each term is not phenomenological but derived from the microscopic theory in the weakly interacting limit. The parameter b is the prefactor of the mean-field term, which is non-local in the case of interest of dipolar BECs. We identify c directly as the quantum fluctuations term prefactor, where we have $\gamma = 1/2$. In contrast to liquid helium, there is no term that scales as $d(\nabla n)^2$ of microscopic origin, however we can right away identify which term will play this role in the BEC functional: the kinetic energy, which will create skin effects by penalizing density gradients. Nevertheless, we will see later on, that surface tension can become relevant.

We now want to compare a few important properties of these two systems.

Temperature

The critical temperature of BECs range from $T \approx 50\,\mathrm{nK} - 2\,\mu\mathrm{K}$. Using evaporation techniques [97], temperatures as low as 3 nK can be reached [98]. Further adiabatic cooling through weakening of the trapping potential could lead to temperatures as low as 450 pK [99]. These systems, can essentially be treated as zero temperature BECs.

The bulk superfluid transition temperature of liquid helium 4 is $T_\lambda = 2.17\,\mathrm{K}$. The temperature of ^{4}He droplets has been indirectly measured using SF_6 molecules yielding a temperature of 0.37(5) K [100]. Similar to the BEC case, the droplets can be treated as $T = 0$ systems, as collective modes are not significantly populated at these temperatures. In contrast to the BEC case, we cannot study a temperature range for ^{4}He droplets. Due to finite evaporation rates in a single droplet, the temperature of these droplets will -

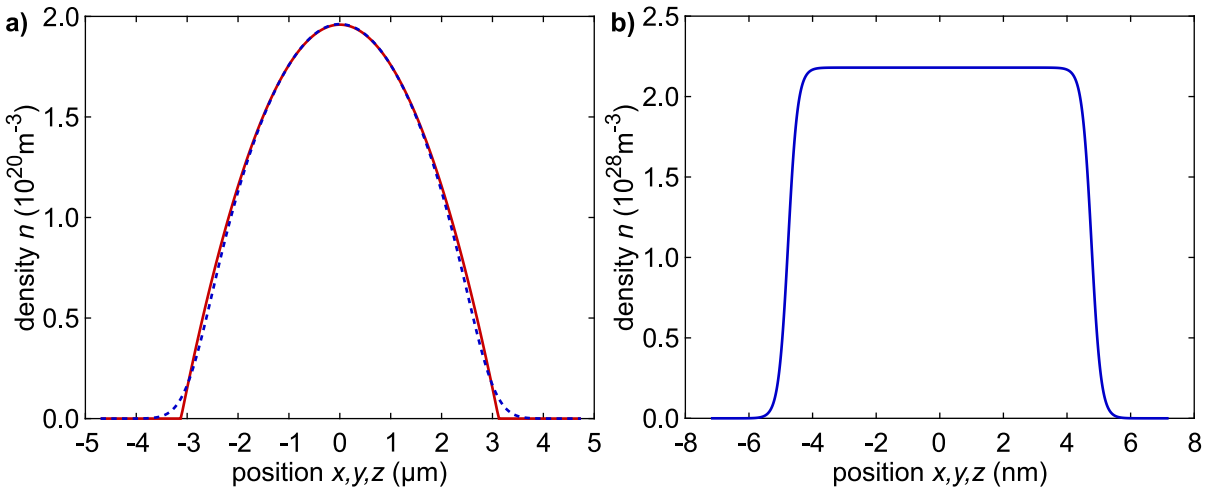

Figure 2.1.: Density profiles: **a)** We plot the density profile of a non-dipolar BEC with $N = 10{,}000$ ^{164}Dy atoms at a scattering length of $a = 100\,a_0$ in a spherical harmonic trap with mean trap frequency $\bar{\omega} = 2\pi \cdot 100\,\mathrm{Hz}$. The blue dashed line shows a numerical solution to eq. (1.16), setting $\Phi_{\mathrm{dd}} = 0$, while the red line is calculated using eq. (1.23). We can see that both solutions agree well, besides the region around the surface. **b)** We use eq. (2.3) to plot the density profile of a ^{4}He droplet with $N = 10.000$ atoms.

within milliseconds - drop to $T \sim 0.3\,\mathrm{K}$ assuming atom numbers higher than 1,000 [101].

Ground state

We calculated the ground state of a repulsively-interacting BEC in section 1.3.2 using a Gaussian variational ansatz or in the Thomas-Fermi approximation. Assuming a contact-interacting gas in the Thomas-Fermi limit, we know the ground state density distribution is given by eq. (1.23), as shown in figure 2.1. Additionally, we plot the numerical result of eq. (1.16), setting $\Phi_{\mathrm{dd}} = 0$. Both results match well, besides a narrow region at the surface. Here, the density vanishes such that the interaction term becomes small and the profile is determined by the balance between the external potential and the quantum pressure [102].

In the case of a helium droplet we have to minimize the energy in eq. (2.1) with respect to the density. There is no need of a trapping potential since the ground state is a self-bound droplet state. We show the density profile of a helium droplet with 10,000 atoms in figure 2.1b. At these high atom numbers, it has been shown that the density profile is described by [103]

$$n(r) = \frac{n_{\mathrm{bulk}}}{2}\left(1 - \tanh\left(2\,\frac{r-R}{g}\right)\right), \tag{2.3}$$

with the bulk helium density $n_{\text{bulk}} = 0.0218\,\text{Å}^{-3}$, the point R, where the density is reduced to the central density and the surface thickness g. We find that the density saturates at n_{bulk} and interpret that this droplet is incompressible. This regime, where the central density has reached the bulk helium density is called the 'leptodermous' regime [104] and has very strong analogies with the liquid drop model. Here, the ratio of g/R scales with the atom number as $N^{-1/3}$. For smaller droplets with an atom number $N \lesssim 240$ this relation is no longer valid and the system becomes 'pachydermic'. At some point, the system becomes 'holodermic', in which case the droplet is a pure surface and the density does not reach n_{bulk}. Using eq. (1.23), it has been shown that the surface thickness of measured helium droplets is $g = 6.4(1.3)\,\text{Å}$, which is independent of the atom number [103]. We see that both profiles differ from each other in shape, absolute size and density. To understand the difference, we can compare the energy per particle in both cases. For the helium droplet, we can express the energy per particle via the liquid drop model to be [92]

$$\frac{E}{N} = a_v + a_s N^{-1/3} + a_c N^{-2/3} + ..., \tag{2.4}$$

with the volume coefficient $a_v = \mu \approx -7.2\,\text{K}$ [17, chp.3], that is at the same time the chemical potential , the surface coefficient a_s and the curvature coefficient a_c. The negative chemical potential together with the strong repulsive interactions in such a droplet leads to the self-bound character where the density is capped at n_{bulk}. For the atomic system we use the Thomas-Fermi approximation of equation (1.37), set $V_{\text{ext}} = 0$ and assume a contact interacting gas with $\Phi_{\text{dd}} = 0$. We solve the integral assuming a homogeneous density distribution $n = N/V$ and result with

$$\frac{E}{N} = \frac{gN}{2V} + \frac{gN}{2V}\frac{128}{15\sqrt{\pi}}\sqrt{\frac{Na^3}{V}}F_5(\varepsilon_{\text{dd}}). \tag{2.5}$$

The important result is that the energy per particle is positive $E/N > 0$, showing the necessity of a trapping potential. Nevertheless, in section 2.3 we will see that when two types of interactions are present, here contact and dipolar interactions, we can meet the conditions to form a self-bound droplet from an ultracold atomic gas.

2.2. Stability and phase diagram of a trapped dipolar BEC

In this section we calculate and describe the phase diagram for a trapped BEC under the influence of the contact and dipolar interactions. The dipolar interaction strongly

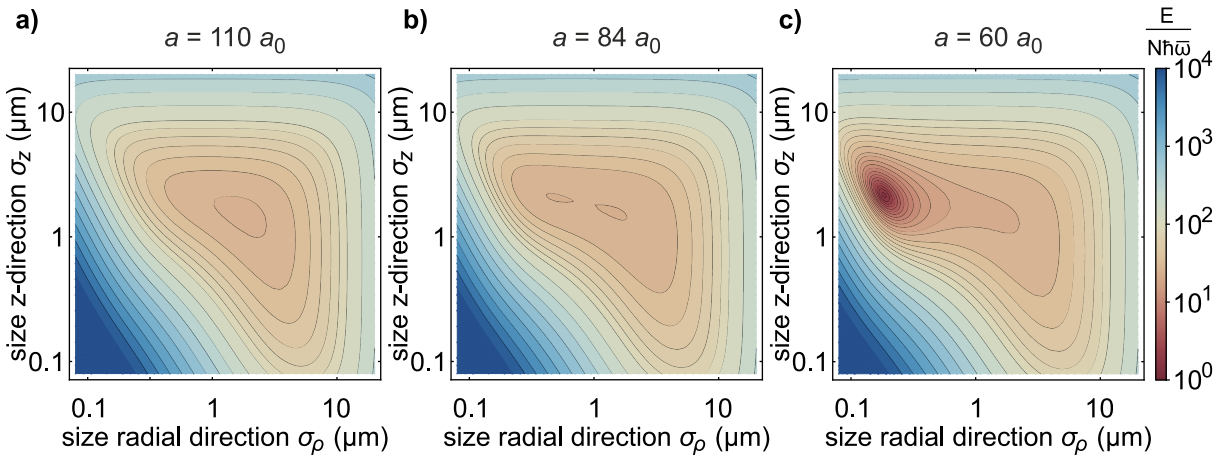

Figure 2.2.: Energy landscape: We plot the calculated energy per particle E/N in units of $\hbar\bar{\omega}$ with $\bar{\omega} = 2\pi \cdot 110\,\mathrm{Hz}$ from eq. (1.38) versus the radial- and z-direction for three different scattering lengths at a trap aspect ratio of $\lambda = 2$ for $N = 8{,}000$ atoms. The color bar is the same for all three plots and is offset by $E/(N\hbar\bar{\omega}) = 16$ to prevent negative values in the logarithmic plots. In **a)**, the scattering length is $a = 110\,a_0$ and we find a minimum at $\sigma_z = 2.00\,\mu$m and $\sigma_\rho = 2.40\,\mu$m. This corresponds to a BEC. In **b)**, the scattering length is $a = 84\,a_0$ and we find two minima, one at $\sigma_z = 2.09\,\mu$m and $\sigma_\rho = 1.95\,\mu$m and one at $\sigma_z = 2.76\,\mu$m and $\sigma_\rho = 0.65\,\mu$m. These two minima correspond to a BEC and a droplet, respectively. For a scattering length of $a = 60\,a_0$, shown in **c)**, the BEC minimum disappears and we only find the droplet minimum at $\sigma_z = 2.89\,\mu$m and $\sigma_\rho = 0.25\,\mu$m.

influences the stability of a BEC compared to a purely contact interacting one [105, 106], and makes it dependent on the trapping potential. In the mean-field ansatz, this has been extensively studied theoretically [77, 107] as well as measured experimentally using chromium atoms [30, 31]. A dipolar BEC is always stable as soon as the scattering length a is larger than the dipolar length a_{dd}. For $a < a_{\mathrm{dd}}$ we can still obtain a stable BEC in the mean-field picture if the trap aspect ratio is high enough, such that the atoms are mostly aligned in a side-by-side configuration and the overall interaction remains repulsive. In the Thomas-Fermi approximation, we can calculate a relation for the critical scattering length as [30]

$$a_{\mathrm{crit}}(\lambda) = a_{\mathrm{dd}} f(\kappa(\lambda)). \tag{2.6}$$

In mean-field, for $a < a_{\mathrm{crit}}$ the overall interaction becomes attractive as the atoms mostly align in a head-to-tail configuration and the BEC collapses. If we include quantum fluctuations, we add another repulsive interaction that prevents the collapse from happening and restabilizes the cloud at finite density. This new phase is called a quantum droplet that we want to study in this section.

To do so, we will use the Gaussian ansatz calculating the energy landscape with the

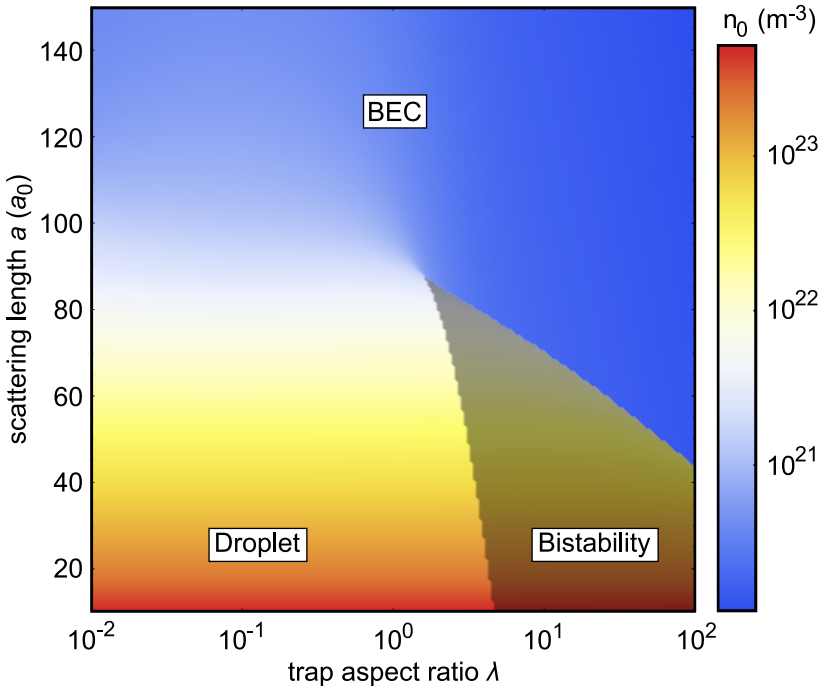

Figure 2.3.: Phase diagram: We plot the peak density as a function of scattering length $a = [10, 150]\, a_0$ and trap aspect ratio $\lambda = [10^{-2}, 10^2]$ for an atom number $N = 8{,}000$ at mean trap frequency $\bar{\omega} = 110\,\text{Hz}$. The color bar represents the peak density of the Gaussian distribution n_0. At large scattering lengths, where the density is on the order of $n_0 \sim 10^{21}$ we find the BEC (low-density) phase. The gray area represents the bistability region where we find both the BEC and the droplet solution. The droplet (high-density) phase is found for low scattering length and low trap aspect ratio, where densities get as high as $n_0 \approx 5 \cdot 10^{23}$.

equations (1.38). Here, we will vary the trap aspect ratio as well as the scattering length for a given atom number. In figure 2.2 we show three example energy landscapes for the three different cases that will be found in the phase diagram for $\lambda = 2$ and $N = 8{,}000$. Figure 2.2a shows the landscape for $a = 110\, a_0$, where we find a single minimum that corresponds to the BEC phase with a peak density of $n_0 = 3 \cdot 10^{20}\,\text{m}^{-3}$. An example for the bistable region with $a = 84\, a_0$ is shown in figure 2.2b, where we find two minima, one corresponding to the BEC phase with a peak density of $n_0 = 4 \cdot 10^{20}\,\text{m}^{-3}$, and the other one corresponding to the droplet phase with a peak density of $n_0 = 3{\cdot}10^{21}\,\text{m}^{-3}$. Finally, at low scattering length $a = 60\, a_0$ the BEC minimum disappears and we remain with a single minimum corresponding to the droplet phase with a peak density of $n_0 = 2 \cdot 10^{22}\,\text{m}^{-3}$. To create a full phase diagram, we track the energy minima for varying scattering length and trap aspect ratio and plot the resulting phase diagram in figure 2.3. For large scattering lengths, we find the BEC phase independent of the trap aspect ratio. If the trap aspect ratio is smaller than a critical trap aspect ratio λ_c, we find a continuous crossover from

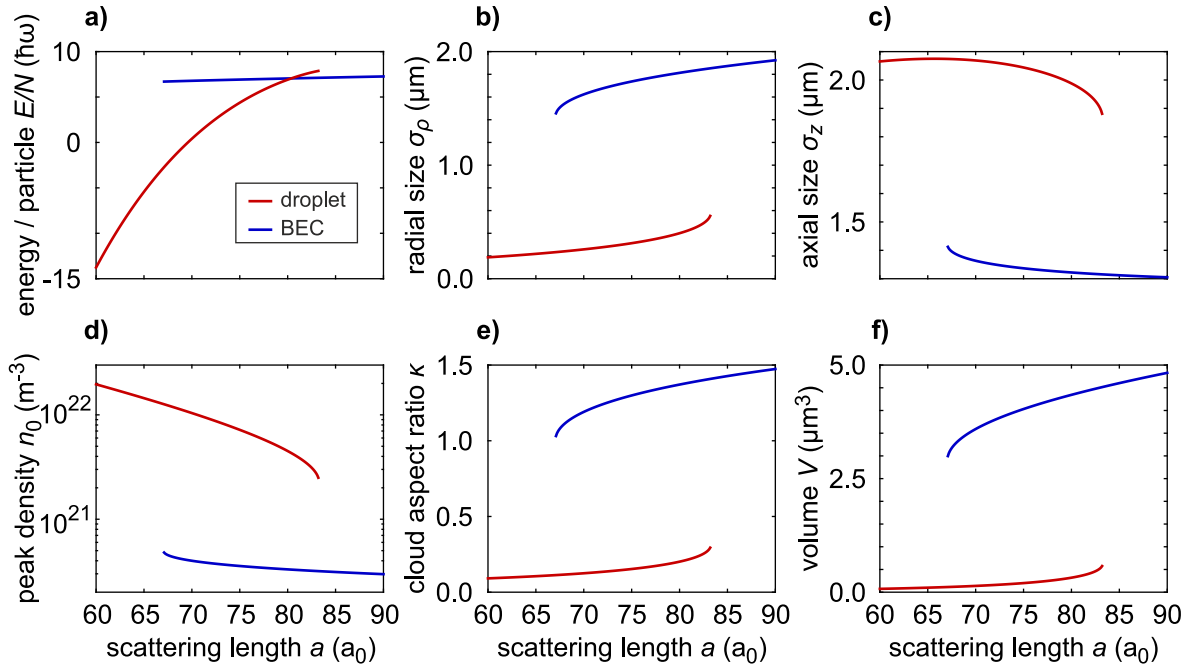

Figure 2.4.: Properties of a dipolar cloud in the bistability region: We plot important properties as a function of the scattering length $a = [60, 90]\, a_0$ for a trap aspect ratio $\lambda = 2.5$ and an atom number of $N = 8{,}000$. **a)** The energy per particle of the droplet and BEC solution cross at $a_{\text{equal}} = 80.4\, a_0$. The radial and axial size (**b),c)**) both show a discontinuity when going from one to the other solution indicating that this is a first-order phase transition. From the two sizes, we calculate the peak density **d)**, the BEC aspect ratio **e)** and the volume **f)**.

the BEC phase to the droplet phase for decreasing scattering length. For $\lambda > \lambda_c$ we find a phase transition from the BEC phase to a bistability phase, where the BEC solution, as well as the droplet solution exist. In the next two subsections, we will study the properties of these phases.

2.2.1. Bistability and angular roton collapse: The Rosensweig instability

To understand the phase transition within the bistable region, we have a closer look at a few important parameters. In figure 2.4, we plot the energy per particle E/N, the cloud sizes (σ_ρ, σ_z), the peak density n_0, the cloud aspect ratio κ and the volume $V = \sigma_\rho^2 \sigma_z$ for a trap aspect ratio of $\lambda = 2.5$. We see that the BEC solution exists down to scattering lengths as low as $a = 67\, a_0$, while the droplet solution exists up to $a = 83\, a_0$. Besides the density, a big difference is found in their size. While the BEC has an aspect ratio of $\kappa > 1$, the droplet becomes very small in the radial direction, leading to an aspect ratio as small

as $\kappa = 0.1$. The reason is that the atoms align themselves in a head-to-tail configuration along the magnetic field direction to minimize their energy. At $a_{\text{equal}} = 80.4\,a_0$, the energy per particle of the BEC phase and the droplet phase are equal. This tells us that the BEC phase is the ground state for $a > a_{\text{equal}}$ while the droplet state is the ground state for $a < a_{\text{equal}}$. Nevertheless, due to the bistability the transition point from a BEC to the droplet state is determined by thermal and quantum fluctuations and can happen anywhere in the bistable region. In the thermodynamic limit we speak of a first-order phase transition following Ehrenfest [108], as the order parameter, in our case the density, is discontinuous at the transition as can be seen in figure 2.4d.

It turns out that this phase transition is in the parameter range where the atomic cloud does not collapse to a single droplet but undergoes an angular roton instability. In 2007, Ronen et. al. predicted an angular roton instability for a dipolar BEC that crosses the stability threshold[6] [109]. The roton instability [110, 111] that has been calculated for infinite sized systems is fundamentally different from a phonon instability. While a phonon instability happens at quasi-momentum $\hbar\boldsymbol{q} = 0$, a roton instability happens at finite quasi-momentum. This leads to a situation where the atomic cloud does not collapse to the trap center but exhibits its maximum density away from the center. The angular roton instability describes this kind of collapse, where discrete angular modes become unstable due to the finite sized system. This allows a density distribution that is biconcave before collapsing on a high-density ring. This ring consequently collapses into a droplet ensemble where the number of droplets is directly correlated to the number of atoms in the BEC [52]. The angular roton minimum as well as the splitting into multiple droplets is in very strong analogy to the normal field or Rosensweig instability[7].

As the instability occurs for density modulations with a finite wavelength, this effect cannot be described by a Gaussian ansatz which assumes a fixed density distribution which is why we turn to effective GPE simulations. The simulation shown in figure 2.5 is done for the experimental parameters from our observations [52] with $N = 15{,}000$, $\omega_{x,y,z} = (44, 46, 133)\,\text{Hz}$ and $T = 20\,\text{nK}$. We show four extracted density profiles, the first one being a BEC with $a = 110\,a_0$ at $t = 0\,\text{ms}$. At that point, the scattering length is quenched to $a = 70\,a_0$. The second image shows the cloud after $t = 6\,\text{ms}$, where a biconcave structure starts to appear. On the third one, after $t = 7\,\text{ms}$ the collapse onto a ring is clearly visible. The last image shows the density profile after $t = 10\,\text{ms}$, where the droplet ensemble is fully developed. We have to state here, that the biconcave structure and consequent ring formation has not been observed experimentally. A possible explanation is that the fluctuations in our case are so strong, that we undergo the instability even before forming

[6] They find this instability for certain islands of the trap aspect ratio, with $\lambda > 6$.
[7] Details on the theoretical description of both systems can be found in [112].

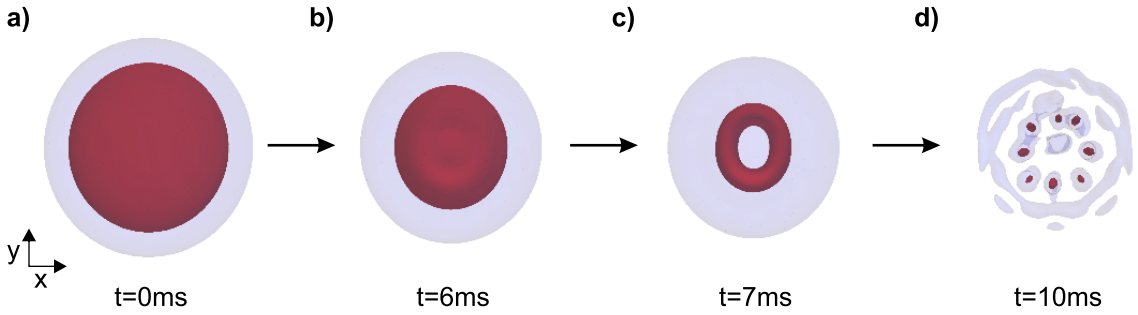

Figure 2.5.: Phase transition from BEC to droplet ensemble: We show the top view of four different density profiles in the xy-plane where the red and gray color represent two different isodensity surfaces, $0.2\,n_0, 0.02\,n_0$ respectively, where n_0 is rescaled to the maximum density for each image. **a)** We prepare the BEC with $N = 15{,}000$ in a trap with $\omega_{x,y,z} = (44, 46, 133)\,\mathrm{Hz}$ at a scattering length of $a = 110\,a_0$. At $t = 0\,\mathrm{ms}$, we quench the scattering length instantaneously to $a = 70\,a_0$. **b)** After $t = 6\,\mathrm{ms}$, we start to see a small biconcave structure. **c)** At $t = 7\,\mathrm{ms}$, the angular roton collapse leads to a density distribution that shows a ring structure. **d)** The droplet ensemble is fully developed after a hold time of $t = 10\,\mathrm{ms}$.

the exact angular roton structure. All of this holds true for $\lambda > \lambda_c$.

2.2.2. Single droplet state

In this section we consider the case where the trap aspect ratio is smaller than λ_c. In this case, the bistability vanishes as can be seen in figure 2.6. The first-order phase transition turns into a continuous crossover. In this crossover region, the droplet and the gaseous BEC phase transform continuously into each other for varying scattering lengths and cannot be differentiated from each other. We will see in section 2.3 that this is a consequence of the presence of the trapping potential.

This behavior is very similar to the phase transition between gas and liquid, where above a critical temperature, the first-order phase transition turns into a continuous crossover. To demonstrate that indeed the droplet phase possesses liquid properties, we calculate the density of a trapped droplet when compressing it by increasing the trap stiffness (frequency). We compare this to a gaseous BEC [113], when these two phases are well differentiated at a trap aspect ratio of $\lambda = 2.5$ and show the results in figure 2.7a. We observe a stark difference between the two phases: while the BEC density strongly scales with the compression as expected for a gas ($n_0 \propto \bar{\omega}^{6/5}$), the droplet behaves like a liquid in that its density is essentially insensitive to the compression. In addition, we plot the density as a function of atom number for the droplet phase. We observe that for high atom numbers, this density is almost insensitive to N. At low atom number $N < 5{,}000$,

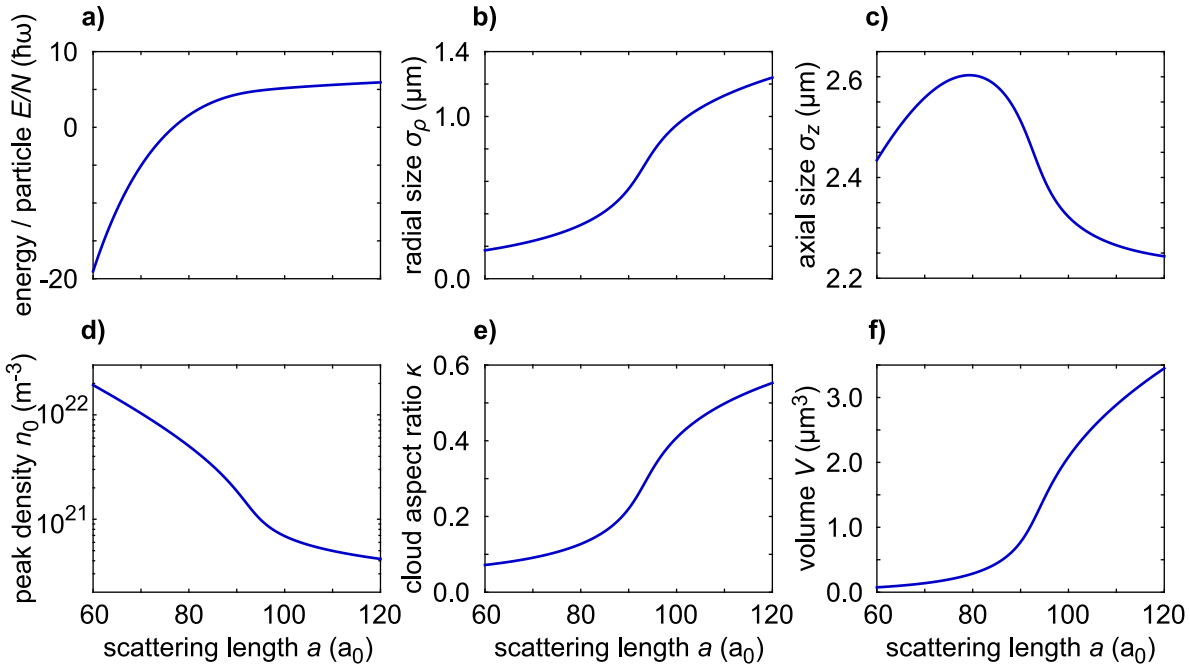

Figure 2.6.: Properties of a dipolar cloud in the crossover region: We plot important properties as a function of the scattering length $a = [60, 120]\, a_0$ for a trap aspect ratio $\lambda = 1$ and an atom number of $N = 8{,}000$. In contrast to figure 2.4, the discontinuity of the bi-stable region completely vanishes for $\lambda < \lambda_c$ and we now observe a smooth crossover. It seems surprising that we find a maximum in σ_z but the scale is small compared to the variation in σ_ρ such that the density as well as the cloud aspect ratio monotonically increase with decreasing a.

we observe a dependence in N. This is due to the fact that in this parameter range, the kinetic energy is non-negligible and tends to decrease the density. This is a strong indication that we deal with a quantum liquid, although very dilute compared to the ^{4}He droplets described in section 2.1. These liquid-like properties observed in a trapped case suggest that one should be able to observe the signature of a liquid state: a macroscopic self-bound state [114, 115]. In other words, if we place a liquid in a given volume it does not fill the whole volume as opposed to a gas but rather forms a self-bound droplet. In order to observe this the trapping potential has to be removed and we present the theory of such self-bound droplets in the following.

2.3. A self-bound dilute magnetic quantum liquid

The first indication of a self-bound state for these quantum droplets can already be seen in figure 2.6, where we calculated the energy per particle. This quantity becomes negative for a certain scattering length in the droplet phase, although this condition is not sufficient.

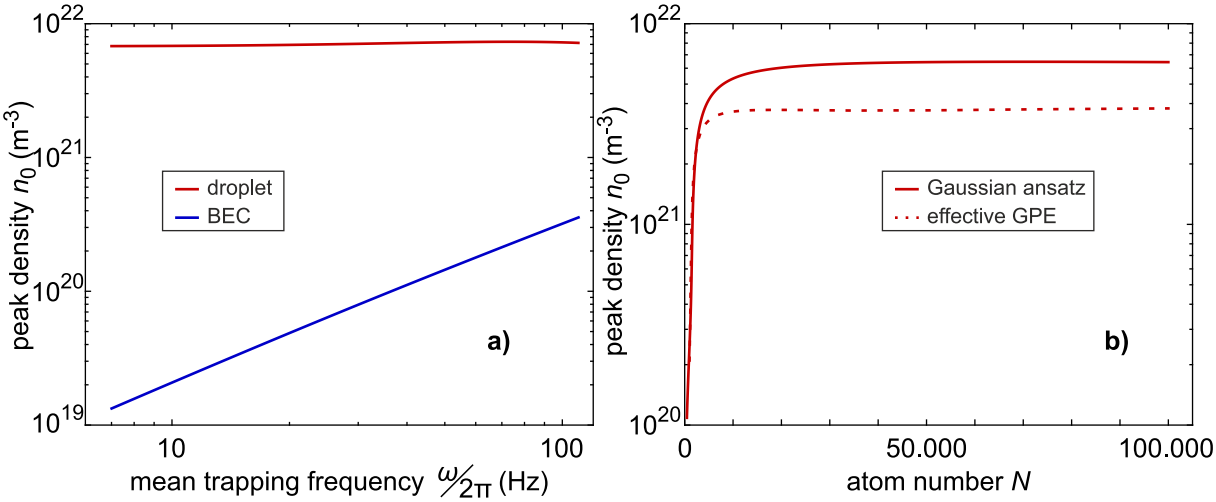

Figure 2.7.: Droplet density: a) Calculated peak density n_0 as a function of mean trapping frequency $\omega/2\pi$ for $N = 8{,}000$, $\lambda = 2.5$ and $a = 75\,a_0$ using the Gaussian variational ansatz. While the BEC peak density (blue line) increases with the trapping frequency to the well known $\bar{\omega}^{6/5}$-scaling, the droplet peak density (red line) is nearly insensitive to the weak compression, behaving like a liquid. **b)** Peak density n_0 as a function of atom number for $\lambda = 1$, $a = 80\,a_0$ and $\bar{\omega} = 2\pi \cdot 100\,\mathrm{Hz}$. We find the peak density to first be increasing with atom number and finally saturating for $N \gtrsim 5{,}000$. We show the calculation from the Gaussian variational ansatz as solid red line as well as the effective GPE simulations as dashed red line. The two curves deviate from each other once the kinetic energy effects can be neglected leading to a lower peak density for the effective GPE simulation. Adapted from [113].

To further investigate this effect, we calculate the energy functionals from eq. (1.38), setting $E_{\mathrm{ext}} = 0$, thus removing the external trapping potential. A resulting energy landscape is shown in figure 2.8a for a scattering length $a = 65\,a_0$ and an atom number $N = 8{,}000$. Although the trapping potential has been removed for these calculations, we find a minimum in the potential landscape at finite size. Within the variational ansatz, this demonstrates the existence of a macroscopic self-bound state at a finite density. We create a new phase diagram for the untrapped dipolar gas, as we track the minimum in the potential landscape for varying atom number and scattering length. We find that the energy minimum gets shallower for decreasing atom number until a critical atom number N_{crit} is reached, where the minimum disappears. The existence of a critical atom number is given by the reason that for low enough atom numbers the kinetic energy term dominates over the sum of the contact and dipolar interaction energy term such that the overall interaction becomes repulsive again. Additionally, we see that the self-bound solution disappears for scattering lengths that are higher than a_{dd}. We plot the critical atom number as a function of scattering length in figure 2.8b. To further compare these

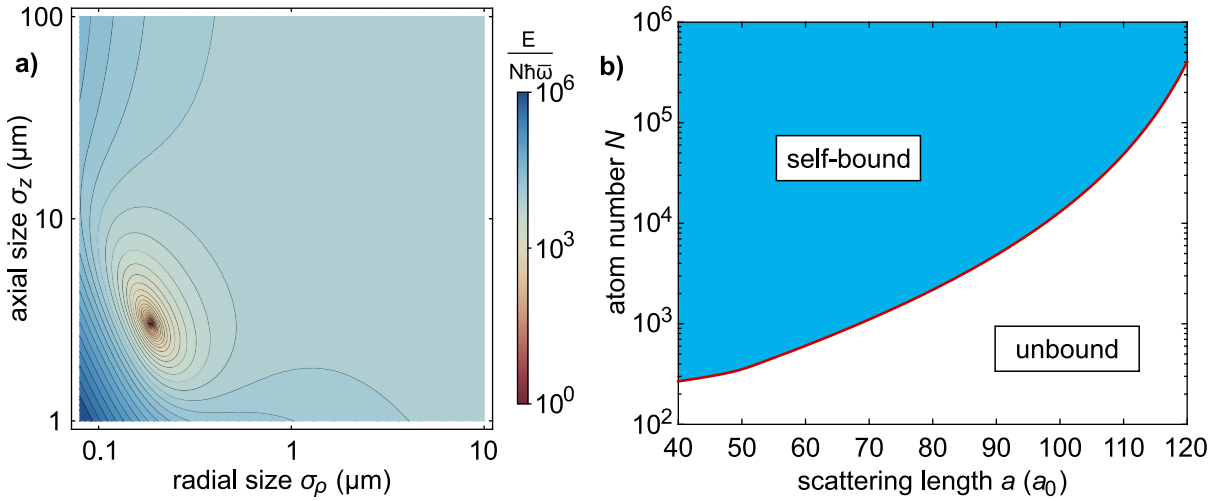

Figure 2.8.: Self-bound quantum droplet: a) Energy per particle E/N in units of $\hbar\bar{\omega}$ as a function of radial and axial size σ_ρ, σ_z for $a = 65\,a_0$ and $N = 8{,}000$ atoms using the Gaussian variational ansatz without external trapping potential. Note, that there is no trapping potential included in the calculation and we only rescale the energy by $\bar{\omega} = 1\,\text{Hz}$. We offset the energy by $E/(N\hbar\omega) = 10^4$ to prevent negative values for the logarithmic plot. We find a striking energy minimum for finite size. A quantum droplet formed at these conditions is a three-dimensional self-bound object. **b)** By varying a and N, we can calculate the critical atom number for which the energy minimum disappears and plot it versus scattering length as red line. For $N > N_{\text{crit}}$ we find a self-bound solution (bright blue area) while for $N < N_{\text{crit}}$ the cloud is unbound and freely expands.

droplets to the case of ^{4}He droplets, we simulate the ground state density profiles for three different atom numbers $N = (1{,}000, 10{,}000, 100{,}000)$ and show the axial and radial profile in figure 2.9a and b respectively. The resolution in the radial profile is limited by the grid size in these simulations. The anisotropy of these droplets results from an energy minimization due to the magnetostriction effect that was mentioned in section 1.3.2 which stands in strong contrast to helium droplets that has an equal size in each direction. Using the same terminology as for helium droplets, the droplet with $N = 1{,}000$ atoms is pachydermic, while for $N = 10{,}000$ and $N = 100{,}000$ the droplets are leptodermic showing a saturated peak-density. At $N = 100{,}000$, we can clearly see the effect of surface tension in the axial profile that is caused by the kinetic energy.

We want to shortly discuss the collective excitations for these quantum droplets. A detailed description and calculation for lowest excitation frequencies can be found in reference [114], while recent experiments on trapped erbium quantum droplets confirmed their calculations [116]. They calculate these eigenfrequencies and their eigenvalues that determine the character of the oscillation, and monitor them across the BEC to droplet

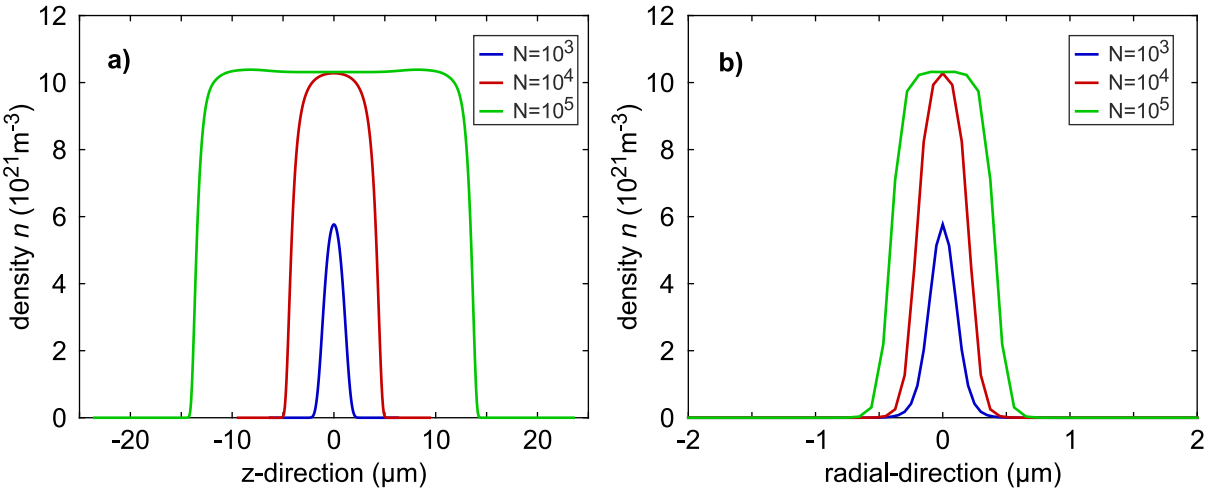

Figure 2.9.: Density profiles: a) We plot the axial density profile for a self-bound droplet at $\rho = 0$ with atom numbers ($N = 1{,}000, 10{,}000, 100{,}000$) in blue, red and green respectively. We see that the peak density is approximately the same for 10,000 and 100,000 atoms. **b)** Due to their small size in the radial direction, the resolution of the density profiles in the radial direction at $z = 0$ was limited by the grid size in the effective GPE simulations.

crossover. One important information is that all collective modes are not only dependent on scattering length but also are strongly dependent on atom number.

So far, we completely ignored effects that may change the atom number over time. The most important one is given in the three-body recombination that leads to atom loss. The parameter here is the three-body loss rate $L_3(n)$ that depends on the scattering length and is different for each atom [117]. As mentioned in section 1.1 the three-body loss at BEC densities is low enough to observe the BEC for a few seconds. In contrast, the density in these droplets is typically at least one order of magnitude higher than in the BEC, such that the droplet lifetime can be as low as $t \sim 300\,\mathrm{ms}$ [52]. We implement this in the Gross-Pitaevskii equation (1.36) that finally reads [88]

$$\begin{aligned} i\hbar\frac{\partial}{\partial t}\Psi(\boldsymbol{r},t) = \Bigg\{ &-\frac{\hbar^2}{2m}\nabla^2 + V_{\mathrm{ext}}(\boldsymbol{r}) + gn(\boldsymbol{r},t) + \int \mathrm{d}^3r' V_{\mathrm{dd}}(\boldsymbol{r}-\boldsymbol{r}')n(\boldsymbol{r}',t) \\ &+ \frac{32g\sqrt{a^3}}{3\sqrt{\pi}}\left(1+\frac{3}{2}\varepsilon_{\mathrm{dd}}^2\right)|\Psi(\boldsymbol{r},t)|^3 - i\frac{\hbar}{2}L_3 n(\boldsymbol{r},t)^2\Bigg\}\Psi(\boldsymbol{r},t). \end{aligned} \tag{2.7}$$

With the knowledge of the three-body loss rate L_3, this effective GPE is able to simulate the time dependence of a self-bound droplet.

Part II.

Experimental Observations

3. A dysprosium BEC in variable trapping potentials

In the following chapter we will describe the first set of results obtained in our dysprosium quantum gas. We will start this chapter by describing the structure of dysprosium and its resulting properties. The following section will deal with the setup and the method used to create a degenerate gas of dysprosium. While we only give a short overview, a detailed description of the complete setup can be found in reference [118]. We finish this chapter by describing our measurements of the phase diagram for a dipolar condensate in a cylindrically symmetric trap. At this point, we will identify the transitions from a Bose-Einstein condensate to the multi droplet phase as well as the single droplet phase.

3.1. Dysprosium

Dysprosium is a rare-earth element from the group of the lanthanides with 66 protons. It is a non-noble metal that oxidizes in an air atmosphere even at room temperature. The melting point is at $T_{\mathrm{melt}} = 1412\,^{\circ}\mathrm{C}$ and it boils at $T_{\mathrm{boil}} = 2567\,^{\circ}\mathrm{C}$. Dysprosium possesses seven stable isotopes, four of which with high natural abundance. Of these four isotopes ^{162}Dy (25.5%) & ^{164}Dy (28.3%) are bosonic and ^{161}Dy (18.9%) & ^{163}Dy (24.9%) are fermionic [119]. In the following, we will only consider the ^{164}Dy isotope since all the results we will present have been obtained with this isotope.

The 66 electrons in dysprosium lead to an electronic ground state configuration of $[\mathrm{Xe}]4\mathrm{f}^{10}6\mathrm{s}^2$ following the Aufbau principle[8]. This means dysprosium possesses a partly filled 4f shell inside a completely filled 6s shell, also known as submerged-shell configuration. Consequently, it allows for transitions where a 6s electron as well as a 4f electron is excited to higher electronic states[9]. Using Hund's rules we find that dysprosium has an

[8] The Aufbau principle describes the order in which electron orbitals are filled and is sometimes called Madelung, Janet or Klechkowsky rule (after Erwin Madelung, Charles Janet and Vsevolod Klechkovsky).

[9] Electrons from lower lying closed shells are typically strongly bound to the core and are not available for transitions to a higher lying electronic state.

orbital angular momentum of $L = 6$ and an electronic spin of $S = 2$ resulting in a total angular momentum of $J = 8$. The term symbol for the electronic ground state finally reads ${}^5I_8$. While the bosonic isotopes do not have a nuclear spin, the fermionic isotopes

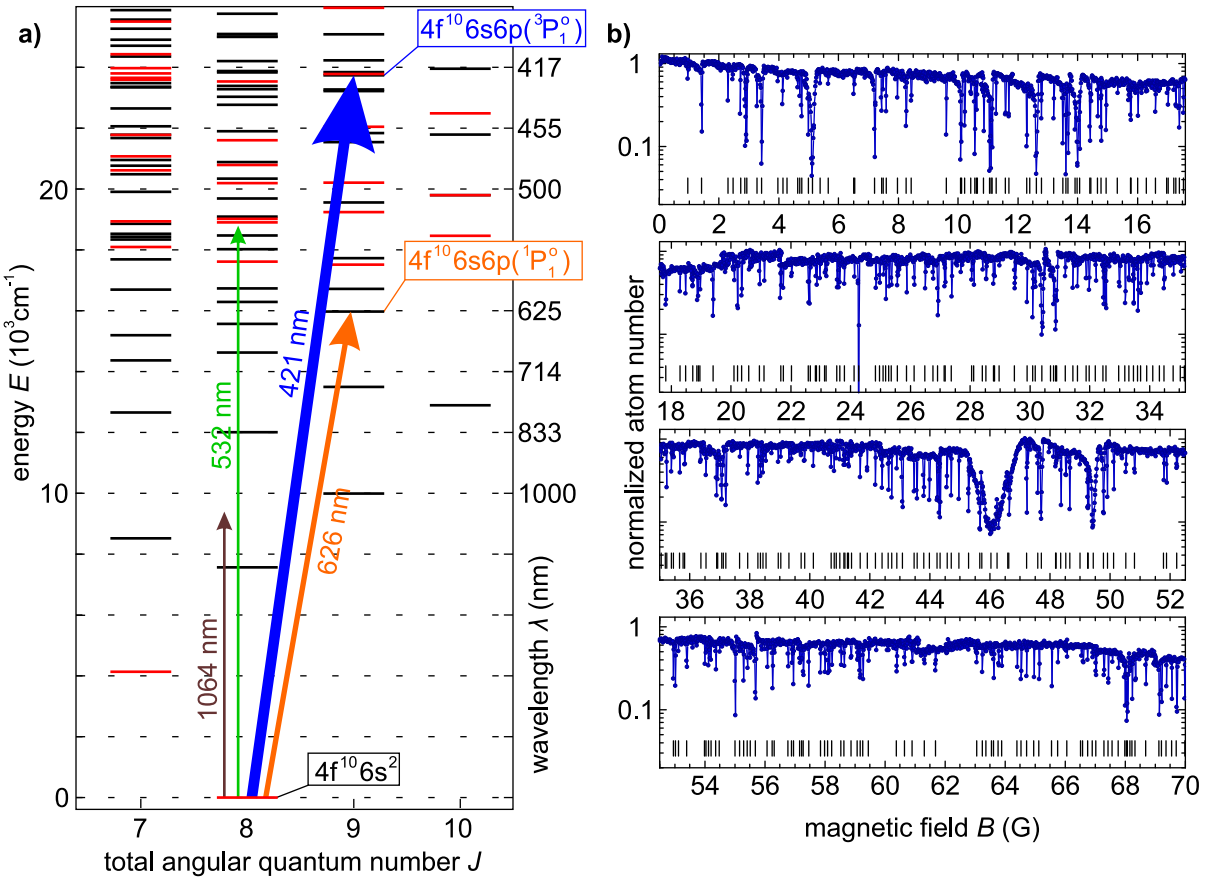

Figure 3.1.: Energy spectrum of dysprosium: **a)** We show a part of the energy level spectrum as a function of total angular quantum number J for dysprosium atoms. Even (odd) parity states are shown in black (red). We indicate two important transitions that both start at the $4f^{10}6s^2$ ground state. One transition excites the atoms to the $4f^{10}6s6p\,({}^3P_1^o)$ state with a transition wavelength of 421 nm. We make use of this transition in the imaging process. The second transition excites the atoms to the $4f^{10}6s6p\,({}^1P_1^o)$ state with a transition wavelength of 626 nm. This transition is used to post-cool the atoms in our crossed optical dipole trap. The wavelength of our dipole traps are indicated as brown (1064 nm) and green arrows (532 nm) that both lead to an attractive potential for the atoms. **b)** We show a trace of a FR scan for the ^{164}Dy isotope as normalized atom number vs. magnetic field up to a magnetic field of $B = 70$ G with a resolution of 14.5 mG. We observe a whole forest of FRs, counting 4.6 resonances per Gauss. Similar to the case of Erbium atoms [48], we observe quantum chaotic behavior in the collision properties and find that it emerges with increasing magnetic field [49].

possess a nuclear spin of $I = 5/2$ resulting in six hyperfine states ranging from $F = 11/2$

to $F = 21/2$. This electronic ground state brings a lot of interesting characteristics that are not only restricted to dysprosium but apply for most of the other lanthanides as well. Firstly, it is at the origin of the high magnetic moment of $\mu_\mathrm{m} = 9.93\,\mu_\mathrm{B}$ which is, together with terbium, the highest magnetic moment of all elements. The strong magnetic moment and the mass of the ^{164}Dy isotope ($m_{164} = 163.93\,\mathrm{u}$) results in a dipolar length (eq. 1.8) of

$$a_\mathrm{dd} = 131\,a_0, \tag{3.1}$$

with the Bohr radius a_0. Secondly, it leads to a very complex energy spectrum that is partly shown in figure 3.1a. And lastly, the scattering properties of dysprosium show quantum chaotic behavior resulting from a highly anisotropic C_6 coefficient [120]. This leads to a very high density of Feshbach resonances, visible in a magnetic-field scan in figure 3.1b. A detailed discussion about the scattering properties can be found in [118].

Three independent measurements for the background scattering length of Dy have been performed. The first one in 2015 in the group of Benjamin Lev, where they measured the cross-dimensional thermalization rate in a thermal gas and compared them to Monte Carlo simulations [121]. Using this method they extracted a background scattering length at a magnetic field of $B = 1.581(5)\,\mathrm{G}$ of $a_\mathrm{BG} = 92(8)\,a_0$. This result relies on the measurement of the scattering cross-section that is the sum of dipolar and contact scattering. A second, indirect measurement was provided by us in 2015, where we identified two broad FRs at a magnetic field of $B = 76.9(5)\,\mathrm{G}$ and $B = 179.1(6)\,\mathrm{G}$ [51]. Here, we measured the width and the binding energy of these resonances and extracted a background scattering length using a method given in reference [122]. This method resulted in a background scattering length of $a_\mathrm{BG} = 91(15)\,a_0$. The third measurement was again provided by the group of Benjamin Lev in 2016 [123]. This time they studied the anisotropic expansion of a thermal gas at a FR at a magnetic field of $B = 1.580(5)\,\mathrm{G}$ and result with a background scattering length of $a_\mathrm{BG} = 96(22)\,a_0$. Combining these three results we obtain a weighted averaged value of $a_\mathrm{BG} = 92.5(12.6)\,a_0$. Using eq. (1.10) this results in a relative dipolar strength of $\varepsilon_\mathrm{dd} = 1.42(19)$. We have to stress here that all these measurements have their drawbacks and are at a different magnetic field value than the one we use for our experiments. We will see in chapter 4 that we have to modify this scattering length to match our results.

Recalling section 2.2, we see that the creation of a stable BEC at such high relative dipolar strength either requires trap aspect ratios of $\lambda > 1.5$ or an increase of the scattering length above a_dd using a FR. In our experiments, we use a combination of both to create a BEC, as described in the following section.

3.2. Science cell and BEC of Dysprosium

In this section, we will present a part of the setup and our steps to create a degenerate gas of dysprosium. The starting point is a cloud of dysprosium atoms that has been loaded from a magneto-optical trap [124] into an optical dipole trap that is transported to a glass cell, as shown in figure 3.2.

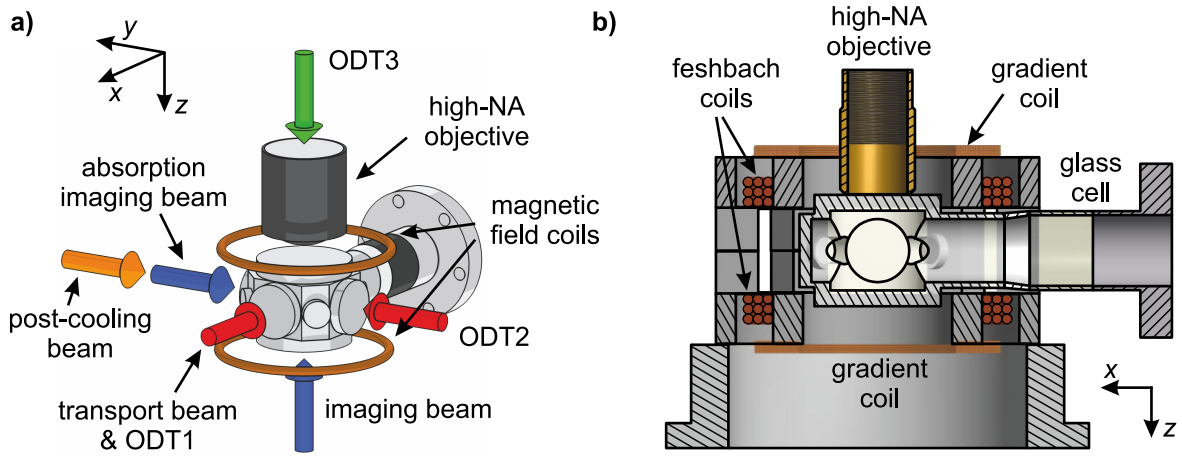

Figure 3.2.: Science Cell: a) A schematic drawing of the science cell. The atoms arrive in the glass cell in a transport beam aligned along the x-direction. They are transferred into a crossed optical dipole trap consisting of ODT1 (x-direction) and ODT2 (y-direction), where they are Doppler-cooled by 626 nm light (y-direction). The magnetic field coils provide homogeneous and gradient magnetic fields to manipulate the properties of the cloud. We can image the atoms via absorption imaging along y and z-direction or perform phase-contrast imaging along the z-direction. A third optical dipole trap (ODT3) along the z-direction allows for additional tuning of the trapping potential. **b)** A sectional side-view along the y-direction of the science cell. We implemented two pairs of coils, one in Helmholtz configuration to create homogeneous magnetic fields and one in anti-Helmholtz configuration to create magnetic field gradients. Both coil pairs are aligned along the z-direction and are mounted in a plastic holder to be as close to the atoms as possible. The microscope objective has a working distance of 25 mm resulting in a distance of 2.63 mm between objective and upper glass window. Taken from [118].

Setup & starting point

The octagonal glass cell offers two major advantages compared to a standard vacuum steel chamber. Firstly, it offers high optical access with its nine high quality glass windows[10]

[10]Gooch & Housego: fused silica glass, flatness $\lambda/20$.

bonded onto a blown quartz glass frame[11]. Secondly, it is non-magnetizable and therefore opens up the possibility for fast magnetic field switching. All windows are anti-reflection coated on their in- and outside for the wavelengths 421 nm, 532 nm and 1064 nm. In this glass cell, the atoms are transferred from the transport beam into a crossed optical dipole trap. The crossed trap consists of two focused dipole trap beams (ODT1 and ODT2) with a wavelength[12] of 1064 nm intersecting at an angle of 90°. ODT1 is aligned along the x-direction[13], superimposed with the transport beam, and radially symmetric with a beam waist of $w_\rho = 35(2)\,\mu$m. ODT2 on the other hand is aligned along the y-direction and elliptically shaped with beam waists $w_x = 109(5)\,\mu$m and $w_z = 29(2)\,\mu$m.

Theory of dipole traps

Before continuing with the experimental sequence, we first review the working principle of an optical dipole trap (ODT) [125]. An ODT for neutral atoms is a far red-detuned focused laser beam that traps atoms due to a finite, positive electric polarizability $\Re(\alpha)$ of an atom, where α is the scalar complex polarizability. The interaction between the alternating electromagnetic field of the laser beam $\boldsymbol{E}(\boldsymbol{r},t) = \tilde{E}(\boldsymbol{r})\exp(-i\omega t)$ and the induced dipole moment of the polarized atom $\tilde{p} = \alpha\tilde{E}$ leads to a trapping potential that is given by

$$V_{\mathrm{dip}}(\boldsymbol{r}) = -\frac{1}{2}\langle \boldsymbol{p}\cdot\boldsymbol{E}\rangle = -\frac{1}{2\epsilon_0 c}\Re(\alpha)I(\boldsymbol{r}), \tag{3.2}$$

with the driving frequency ω, the intensity of the field $I = 2\epsilon_0 c|\tilde{E}|^2$, the electric constant ϵ_0 and the speed of light c. In addition to the trapping potential, the interaction also leads to an absorption and consequently re-emission of photons that are described by the scattering rate

$$\Gamma_{\mathrm{sc}}(\boldsymbol{r}) = \frac{P_{\mathrm{abs}}}{\hbar\omega} = \frac{1}{\hbar\epsilon_0 c}\Im(\alpha)I(\boldsymbol{r}). \tag{3.3}$$

The polarizability α of a neutral atom can be calculated using the Lorentz's model of a classical oscillator. Here, the atom is considered as two-level system with the corresponding optical transition frequency ω_0 and the electron is bound elastically to its core. With this we obtain

$$\alpha(\omega) = 6\pi\epsilon_0 c^3 \frac{\Gamma/\omega_0^2}{\omega_0^2 - \omega^2 - i(\omega^3/\omega_0^2)\Gamma}, \tag{3.4}$$

[11] Precision Glassblowing (TechGlass).

[12] Our most recent measurement for the polarizability at this wavelength yields: $\Re(\alpha) = 139(10)$ a.u.. Here, a.u.is the atomic unit of the electric polarizability with 1 a.u. $= 1(e^2a_0^2)/E_{\mathrm{h}}$, with the elementary charge $e = 1.602\cdot10^{-19}$ C.

[13] The directions mentioned here are given in our laboratory coordinates, shown in figure 3.2.

with the damping rate Γ that describes the spontaneous decay from the excited state. Inserting eq. (3.4) into eqs. (3.2) and (3.3) and applying the rotating wave approximation[14] yields

$$V_{\mathrm{dip}}(\boldsymbol{r}) = -\frac{3\pi c^2}{2\omega_0^3}\frac{\Gamma}{\omega-\omega_0}I(\boldsymbol{r}) \tag{3.5}$$

and

$$\Gamma_{\mathrm{sc}}(\boldsymbol{r}) = \frac{3\pi c^2}{2\hbar\omega_0^3}\left(\frac{\Gamma}{\omega-\omega_0}\right)^2 I(\boldsymbol{r}). \tag{3.6}$$

The intensity profile of a laser beam propagating in z-direction is a Gaussian distribution that is given by [126, p.85]

$$I(x,y,z) = \frac{2P}{\pi w_x(z)w_y(z)}\exp\left\{-2\left(\frac{x^2}{w_x(z)^2}+\frac{y^2}{w_y(z)^2}\right)\right\}, \tag{3.7}$$

with the power of the laser beam P and the beam size in the x,y-direction $w_{\mathrm{x,y}}(z)$. Inserting eq. (3.7) into eq. (3.5) and considering low temperatures such that the atoms are trapped in the center of the beam we can use the harmonic approximation which yields

$$V_{\mathrm{dip}}(x,y,z) = V_0 + \frac{m}{2}(\omega_x^2+\omega_y^2+\omega_z^2). \tag{3.8}$$

Here, V_0 corresponds to the trap depth at the center of the trap that can be expressed as

$$V_0 = -\frac{\Re(\alpha)}{\epsilon_0\pi c}\frac{P}{w_x(0)w_y(0)}. \tag{3.9}$$

From eq. (3.8) we can derive the trap frequencies as a function of the trap depth

$$\omega_x = \sqrt{\frac{4V_0}{mw_x^2}}, \qquad \omega_y = \sqrt{\frac{4V_0}{mw_y^2}}, \qquad \omega_z = \sqrt{\frac{2V_0}{mz_{\mathrm{R,ell}}^2}}. \tag{3.10}$$

Here, the Rayleigh length for an elliptical beam is given by $z_{\mathrm{R,ell}} = z_{\mathrm{R}_x}z_{\mathrm{R}_y}/\sqrt{\frac{1}{2}(z_{\mathrm{R}_x}+z_{\mathrm{R}_y})^2}$. This shows that the polarizability of an atom for a given wavelength can be determined by the knowledge of the beam properties and the trapping frequencies. As we are working

[14] The leading terms are $1/(\omega_0-\omega)$ and $1/(\omega_0+\omega)$. As the laser frequency ω is usually on the same order of magnitude as the transition frequency ω_0, we can neglect the counter-rotating term and set $\omega/\omega_0 \approx 1$.

with a crossed optical dipole trap with three beams, eq. (3.8) has to be expanded to

$$\begin{aligned} V_{\mathrm{dip}}(x,y,z) = &- \frac{1}{\epsilon_0 \pi c}\left(\frac{\Re(\alpha_1)P_1}{w_{1,y}(x)w_{1,z}(x)} + \frac{\Re(\alpha_2)P_2}{w_{2,x}(y)w_{2,z}(y)} + \frac{\Re(\alpha_3)P_3}{w_{3,x}(z)w_{3,y}(z)}\right) \\ &+ \frac{m}{2}(\omega^2_{x,\mathrm{crossed}} + \omega^2_{y,\mathrm{crossed}} + \omega^2_{z,\mathrm{crossed}}), \end{aligned} \tag{3.11}$$

where $\alpha_{1,2,3}$ is the polarizability for the wavelength of each beam. Accordingly, the trap frequencies are given by

$$\begin{aligned} \omega_{x,\mathrm{crossed}} &= \sqrt{\frac{1}{m}\left(\frac{2V_{1,0}}{mz^2_{1,\mathrm{R,ell}}} + \frac{4V_{2,0}}{mw^2_{2,x}} + \frac{4V_{3,0}}{mw^2_{3,x}}\right)}, \\ \omega_{y,\mathrm{crossed}} &= \sqrt{\frac{1}{m}\left(\frac{4V_{1,0}}{mw^2_{1,y}} + \frac{2V_{2,0}}{mz^2_{2,\mathrm{R,ell}}} + \frac{4V_{3,0}}{mw^2_{3,y}}\right)}, \\ \omega_{z,\mathrm{crossed}} &= \sqrt{\frac{1}{m}\left(\frac{4V_{1,0}}{mw^2_{1,z}} + \frac{4V_{2,0}}{mw^2_{2,z}} + \frac{2V_{3,0}}{mz^2_{3,\mathrm{R,ell}}}\right)}. \end{aligned} \tag{3.12}$$

Post-cooling in the crossed dipole trap

Following the loading of the crossed dipolar trap, we post-cool the atomic sample with a beam of 626 nm light to increase the atom number in the crossed region. The cooling beam has an intensity of only $\sim 0.03\, I_{\mathrm{sat},626}$, with the saturation intensity of this transition $I_{\mathrm{sat},626} = 72\,\mu\mathrm{W/cm^2}$ [127]. The most efficient cooling is achieved for a cooling time of 500 ms at a red detuning of $\Delta_{626} = -1 \cdot \gamma_{626}$ with the linewidth $\gamma_{626} = 136(4)$ kHz. At this point, we typically trap $5 \cdot 10^5$ atoms in the crossed region, while $2.5 \cdot 10^6$ atoms still remain in ODT1. The temperature is typically $20\,\mu$K resulting in a phase-space density on the order of 10^{-4}.

Evaporative cooling to BEC

From this point on we perform forced evaporative cooling [97] to increase the phase-space density and achieve a BEC. This cooling technique relies on the removal of atoms with above-average energy from the trap. The remaining cloud rethermalizes through elastic two-body collisions and finally reaches a lower equilibrium temperature. In our case, an atom can leave the trap if its thermal energy is higher than the depth of the trapping potential. Thus, forced evaporation is performed by lowering the trapping potential depth by lowering the intensity of both dipole trap lasers in a way that optimizes the gain in

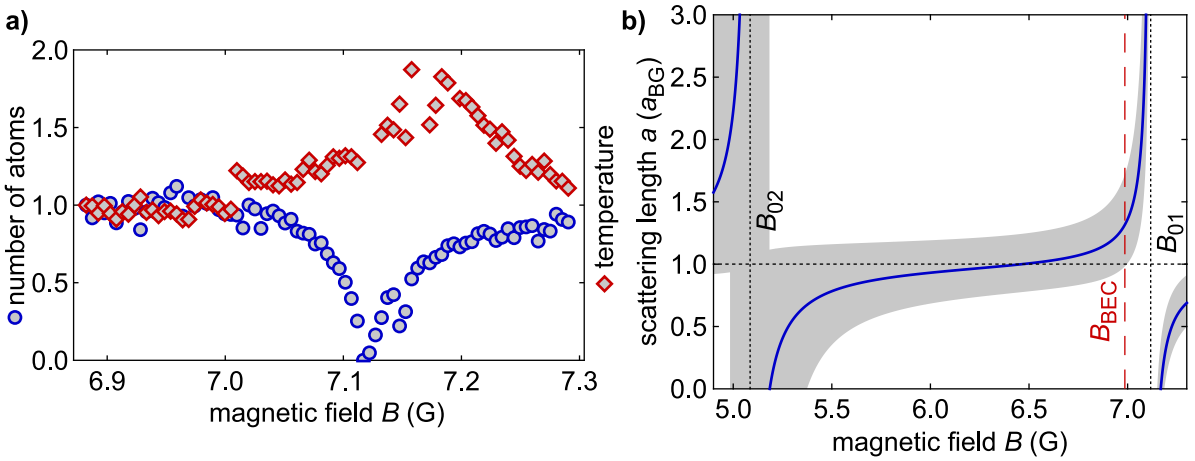

Figure 3.3.: Feshbach resonance: a) We show the normalized atom number (blue circles) and temperature (red diamonds) as a function of the magnetic field around the FR at $B_{01} = 7.117(3)\,\mathrm{G}$. Its position can be very well identified using the minimum in atom number. In contrast to this, the width determination through the maximum in temperature is defective as we see that a second resonance appears at a magnetic field of $B = 7.15(1)$ that creates an additional peak in temperature. Nevertheless, we measure the width to be $\Delta B_1 = 51(15)\,\mathrm{mG}$. Adapted from [52]. **b)** We calculate the scattering length in units of the background scattering length as a function of magnetic field. To do so, we take into account the resonance at $B_{01} = 7.117(3)\,\mathrm{G}$ as well as the resonance at $B_{02} = 5.1(1)\,\mathrm{G}$ with its respective widths $\Delta B_1 = 51(15)\,\mathrm{mG}$ and $\Delta B_2 = 0.1(1)\,\mathrm{G}$. The gray area represents one standard deviation taking into account the errors in the positions, widths and the error in a_{BG}. We typically create a BEC at a field of $B_{\mathrm{BEC}} = 6.986(5)$ where the scattering length is calculated to be $a \approx 1.3\,a_{\mathrm{BG}}$.

phase-space density. In a first 6 s long evaporation process we use a magnetic field of $B = 1\,\mathrm{G}$ ($a \approx a_{\mathrm{BG}}$) to reach temperatures of around $2\,T_{\mathrm{C}}$, where $T_{\mathrm{C}} \approx 100\,\mathrm{nK}$.

Recalling section 2.2 we need to increase the scattering length to be able to create a stable BEC. We do this, using the $\Delta B_1 = 51(15)\,\mathrm{mG}$ wide FR at $B_{01} = 7.117(3)\,\mathrm{G}$ that is shown in figure 3.3a. This resonance allows the tuning of a to values where we can create a stable BEC and still have long lifetimes. We model the scattering length in this region using an additional resonance at $B_{02} = 5.1(1)\,\mathrm{G}$ with a width of $\Delta B_2 = 0.1(1)\,\mathrm{G}$, and calculate the corresponding scattering length in figure 3.3b. With this knowledge, we tune the magnetic field to $B_{\mathrm{BEC}} = 6.986(5)\,\mathrm{G}$ where we calculate the scattering length to be $a \approx 1.3\,a_{\mathrm{BG}}$. With these parameters, we perform a second evaporation sequence that takes 1 s to finally generate a BEC of up to 15,000 atoms at a temperature of 50 nK. After this second evaporation we apply a magnetic field gradient along the z-direction with a strength of $\nabla B = 1.1\,\mathrm{G/cm}$. This gradient leads to a deeper potential depth as it partly compensates for the earth magnetic field gradient ($\nabla B_{\mathrm{earth}} = -2.9\,\mathrm{G/cm}$) and leads to

a higher stability between different experimental realizations. We typically end up in a trap with calculated powers $P_{\mathrm{ODT1}} = 22\,\mathrm{mW}$ and $P_{\mathrm{ODT2}} = 611\,\mathrm{mW}$ yielding frequencies of $(\omega_x, \omega_y, \omega_z) = 2\pi \cdot (40, 40, 155)\,\mathrm{Hz}$ that result in a trap aspect ratio of $\lambda = 3.87$.

All these properties can be extracted by so-called time-of-flight measurements, where the trapping potential is suddenly turned off and the cloud is imaged after a given time of free expansion. We make use of this technique and resonantly image the atoms on the 421 nm transition after a free expansion time of $t_{of} = 18\,\mathrm{ms}$ along the y-direction. This kind of imaging technique allows the measurement of the momentum distribution of thermal clouds. From this we extract their temperature and can clearly identify the appearance of condensation as a bimodal distribution.

High resolution imaging

Time-of-flight imaging cannot yield information about the in-trap density without making assumptions about the state of the system. Therefore, a direct in-situ imaging allows to gain important knowledge without the necessity of making strong assumptions. Given the properties of a typical BEC, in-situ imaging techniques have to fulfill certain requirements. Firstly, with the BEC size of a few μm, we need to implement a microscope objective with a high resolution. In our setup we use a custom made microscope objective[15] with a focal length of $f = 25\,\mathrm{mm}$. Given the clear aperture of 17 mm, the numerical aperture is NA $= 0.32$ leading to a resolution of $\sim 1\,\mu\mathrm{m}$. The objective is mounted on three translation stages: a home-made xyz-stage and a tilt-stage[16] for rough alignment and a piezo xyz-stage[17] with a travel range of $300\,\mu\mathrm{m}^3$ for fine alignment. A second objective[18] with a focal length of 1250 mm leads to a magnification of $M = 50$. Both objectives are diffraction-limited for the wavelengths $\lambda = 421\,\mathrm{nm}$ and $\lambda = 532\,\mathrm{nm}$. The optical setup is completed by an electron multiplying charged coupled device (EMCCD) camera[19] with a pixel size of $(16 \cdot 16)\,\mu\mathrm{m}^2$. A detailed specification of the imaging setup can be found in reference [128]. Secondly, the density of a trapped BEC is so high that its optical density is much bigger than unity. In this regime, the absorption is not linear with the optical density and the extracted image does not reflect the line density. To prevent this, we perform polarization phase contrast imaging, first used to image a BEC of lithium atoms in 1997 [129]. The technique relies on the dispersive phase shift produced by a dense atomic sample. Here, we use off-resonant light that is red detuned to the 421 nm

[15] Special Optics: 54-17-25-532/421nm.
[16] Newport Spectra-Physics: M-TTN80.
[17] Physik Instrumente (PI): stage: P-563.3CD, controller: E-725.3CDA.
[18] Special Optics: 54-17-1250-532/421nm.
[19] Andor iXon DU897 ECS-EXF.

transition and linearly polarized. With the magnetic field aligned along the imaging direction, only σ^+ and σ^- light can couple to the atoms. As the dysprosium BEC is prepared in the lowest lying Zeeman state $m_J = -8$ the atoms mainly couple to the σ^- light as the Clebsch-Gordan coefficient for the σ^+ transition is a factor of 150 times weaker. This results in a phase shift for the σ^- component of the light after passing through the atomic cloud while the σ^+ component remains almost undisturbed. Combining these polarizations again on a linear polarizer leads to an intensity distribution that depends on the dispersive shift due to the atoms. We can extract the atomic column density by taking a series of three images. The intensity distribution of the first image I_1 is taken when the atoms are present. The second image I_2 is taken without the atoms and the third image I_3 gives the background counts resulting from dark counts of the camera. The column density is extracted from these images using the following formula, derived in [130]

$$n_{2\mathrm{D}} = 8\frac{2\pi}{3\lambda^2}\frac{\Delta_{421}}{\gamma_{421}}\left\{\theta - \arccos\left(\sqrt{\frac{I_1 - I_3}{I_2 - I_3}}\cos\theta\right)\right\}, \tag{3.13}$$

with the wavelength of the imaging light λ, its detuning to the transition Δ_{421}, the transition linewidth γ_{421} and the polarizing angle θ between the linear polarization of the imaging light and the linear polarizer. An image cleaning algorithm is applied to the resulting images that will be described in the appendix A. For all experiments shown here, we use a polarizer angle of $\theta = 15\,^\circ$ and variable detuning in the range $\Delta_{421} = [-5, -35] \cdot \gamma_{421}$.

Manipulation of the trap aspect ratio

The last important tool we use in our setup is ODT3 that is aligned along the z-direction. This dipole trap beam with a wavelength of 532 nm creates another attractive potential that allows tuning of the trap aspect ratio. Due to the wavelength being much closer to the strong optical transitions, this yields a high calculated polarizability [118, 131] of ~ 350 a.u.. As mentioned earlier, the polarizability of a transition can be determined if the beam properties and the trapping frequencies are known. We measure the trap frequencies for different powers of ODT3 by observing oscillations of the cloud size and center of mass. Here, we first linearly increase the power of ODT1 and ODT2 within 10 ms by a factor of two, hold the cloud for another 10 ms at this power level and then instantaneously return to the initial conditions. This sequence leads to a breathing of the cloud and an oscillation of the cloud with respect to the trap center due to slight misalignment of the different dipole traps as shown in figure 3.4a. We can extract all three trap frequencies using the two imaging directions shown in figure 3.2a and plot

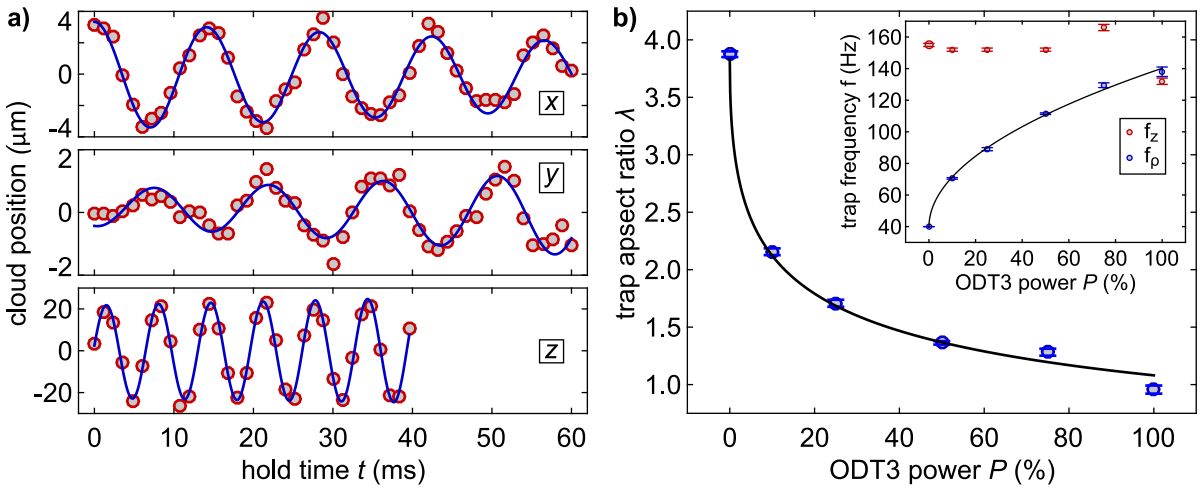

Figure 3.4.: Trap properties: a) Examples of trap frequency measurements (red circles) in the x, y, z-direction in panel (1,2,3) respectively. The data was taken for a power of ODT3 of 10 % of its total power of 14 mW. We plot the cloud position as a function of hold time t. To each data set, we fit a sine function (blue line) to extract the frequencies $f_x = 70.7(0.7)$ Hz, $f_y = 69.5(1.4)$ Hz and $f_z = 152.2(0.8)$ Hz. Here, the error in the brackets are one standard deviation. The position for the x, y-direction was taken with in-situ phase contrast imaging and represents the position offset in-trap while the z-direction was measured with a time-of-flight absorption image. This results in a bigger oscillation amplitude that does not represent the in-trap position but rather the momentum. **b) Inset:** We plot the trap frequencies as a function of ODT3 power. As f_x and f_y were very similar, we averaged them to a mean value, being f_ρ (blue circles). We fit f_ρ with a square-root function (black line) as expected from eq. (3.12). f_z (red circles) stays roughly constant as the contribution coming from the Rayleigh length of ODT3 is small. For $P = 100\,\%$, f_z drops which can be explained by a small mismatch of the relative waist positions of all three beams that pulls the atoms out of the central region of the crossed trap created by ODT1 and ODT2. **b)** We calculate the trap aspect ratio $\lambda = f_z/f_\rho$ (blue circles) and plot it as a function of ODT3 power P. The black line corresponds to the mean of f_z divided by the fit of the square-root function from the inset.

them in figure 3.4b as a function of the ODT3 power. The inset shows the trap frequency as a function of relative ODT3 power P, where $P = 100\,\%$ corresponds to a power of 14 mW. The trap frequencies in x, y-direction are very similar, so we averaged them to an effective radial frequency f_ρ. The radial frequency shows the characteristic square-root behavior with increasing power, while f_z is roughly constant and drops for a power of $P = 100\,\%$. From the measured frequencies and the fit, we can calculate the trap aspect ratio $\lambda = f_z/f_\rho$ as a function of P and find that we can realize ratios of $\lambda = 4$ down to $\lambda = 1$ in our setup.

As the beam is focused by our high-NA objective, we were not able to measure the beam

waist when adding it to the setup. Nevertheless, we calculated it to be $w_{x,y} = 18\,\mu$m. As the polarizability scales with the beam waist to the 4^{th} power, we cannot give an accurate measurement of the polarizability but only a new estimate[20]. We give a conservative range for the actual beam size that lies between 16 μm and 25 μm which leads to a polarizability in the range of $\Re(\alpha) = 64$ a.u. and $\Re(\alpha) = 386$ a.u..

3.3. Exploring the phase diagram

In this section we present an experimental exploration of the phase diagram for a trapped dipolar BEC, which was described theoretically in section 2.2. The corresponding measurements are enabled by the techniques that were introduced in the previous section. The first set of measurements determines the critical trap aspect ratio that separates the bi-stable region from the crossover region. In a second step we measure the critical scattering length for the Rosensweig instability as a function of the trap aspect ratio.

3.3.1. Rosensweig instability vs. single droplet state: Critical trap aspect ratio

We showed in section 2.2 that the Rosensweig instability results from a finite-wavelength instability of the dipolar BEC. Theoretically this is seen as a bistability region where the BEC phase (low density phase) and the droplet phase (high density phase) coexist. This bistability region only exists for a trap aspect ratio that is higher than $\lambda_c \simeq 1.8$. In figure 3.5, we show the phase diagram that has been calculated with the Gaussian ansatz, and sketch our experimental sequence. Our initial conditions are as follows: We start with a BEC consisting of $N \approx 8{,}000$ atoms at $\lambda = 3.87$ close to the FR at $B_{\mathrm{BEC}} = 6.986(5)$ G. We indicate this as point A in the phase diagram. The calculated scattering length at this field is $a \approx 1.3\,a_{\mathrm{BG}}$. Within 50 ms we linearly ramp up the power of ODT3 to change the trap aspect ratio to the desired value. In the subsequent 20 ms we linearly change the magnetic field to $B_{\mathrm{final}} = 6.468(5)$ G where we calculate a scattering length of $a \approx a_{\mathrm{BG}}$. At this point we are either in the droplet phase or in the bistability region of the diagram. We linearly turn off ODT3 within the next 50 ms and hold the cloud for an additional 10 ms at these conditions before imaging them with phase-contrast imaging at a detuning of $\Delta_{421} = -10 \cdot \gamma_{421}$. With this sequence, we assure that we always take the image in the same final trapping conditions, which we indicate as point B in the phase diagram. We show two characteristic images in figure 3.5b with $\lambda > \lambda_c$ and $\lambda < \lambda_c$ respectively. For

[20]The last measurement was done in [118] where we estimated the polarizability to be 11 a.u..

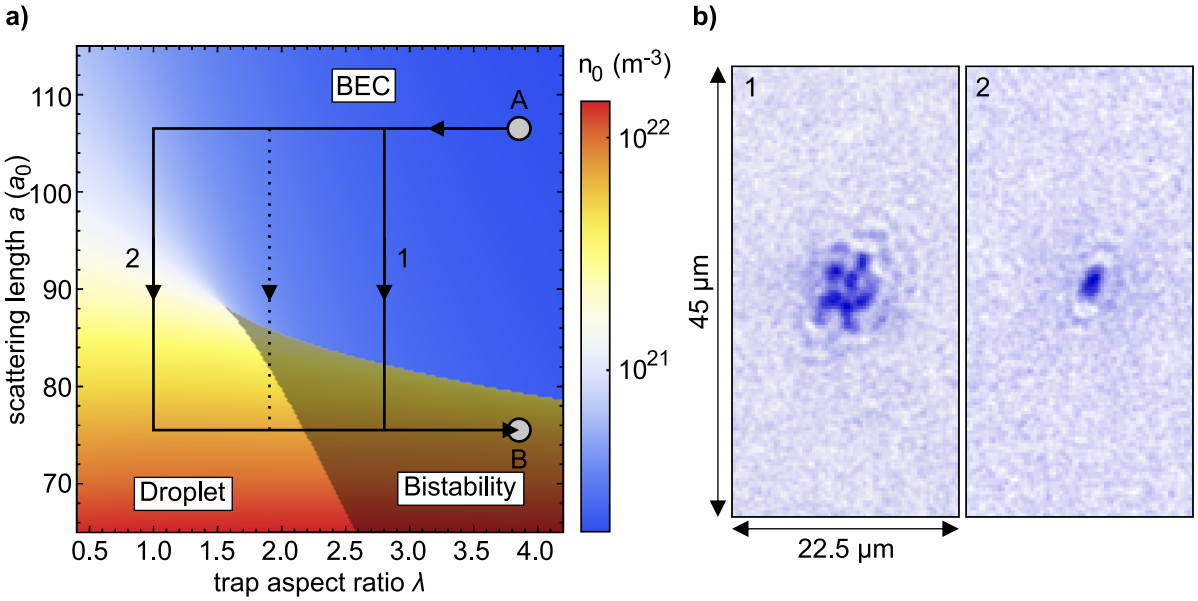

Figure 3.5.: Single droplet procedure: a) We recall the phase diagram from figure 2.3 and zoom into the interesting area of $a = [65, 115]\, a_0$ and $\lambda = [0.4, 4.2]$. Our experimental procedure starts at point A in the BEC phase. Notice, that the points A and B in this diagram do not represent accurate measures of the scattering lengths but rather indicate the region for our starting and final point. We change λ to the desired value before changing the scattering length using magnetic fields. We always image the cloud at point B. The two paths 1 and 2 correspond to the two limiting cases for the trap aspect ratio while the dotted path represents all measurements in between. **b)** We show two example pictures. In the first picture, we took path 1 and crossed the threshold to the bistable region, thus creating a droplet crystal. In contrast, picture 2 was taken after following path 2 where we first create a single droplet and then enter the bistable region. The result shows a single droplet.

$\lambda > \lambda_c$ we observe a droplet ensemble that results from the finite-wavelength instability, as was explained earlier. In contrast, for $\lambda < \lambda_c$ we always observe a single droplet representing the ground state of the droplet phase.

For a detailed analysis of the transition from a single droplet to a droplet crystal we make use of the so-called principal component analysis [132]. This imaging analysis technique is a statistical method that extracts significant features of a series of images. An explanation of the PCA can be found in the appendix B. In brief, it allows to express each image as a linear combination of the eigenvectors from the covariance matrix of all images. It can be shown that the eigenvectors with the biggest eigenvalues α are the most relevant ones to describe the images, which justifies the use for this basis set. We thus sort the eigenvectors by decreasing eigenvalue and plot α^2 as a function of the first 200 eigenvectors in figure 3.6a for two different trap aspect ratios. Here, $\lambda = 2.62$ shown as

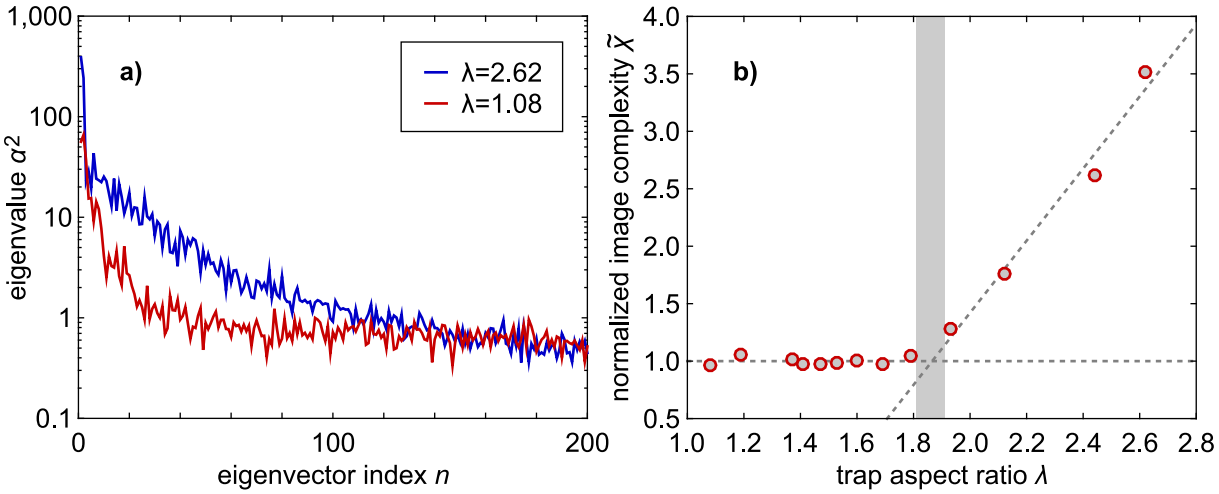

Figure 3.6.: Critical trap aspect ratio: a) We plot the first 200 squared eigenvalues α^2 over their index n for two different trap aspect ratios λ. For $\lambda = 2.62$ we create a droplet crystal. Consequently, we need more eigenvectors to represent the image than in the case of $\lambda = 1.08$, where we create single droplets. **b)** We show the normalized image complexity $\tilde{\chi}$ as a function of trap aspect ratio λ. $\tilde{\chi}$ is defined as the sum of the squared eigenvalues α^2 up to $n = 150$ and normalized to the range of $\lambda = 1.08$ to $\lambda = 1.79$ as these aspect ratios result in single droplet images. For $\lambda \geqslant 1.93$ we see an increase in $\tilde{\chi}$. A linear fit to this increase crosses $\tilde{\chi} = 1$ at $\lambda_c = 1.87(8)$, defining the critical trap aspect ratio. The gray shaded area visualizes the uncertainty of the fit.

blue curve is the decomposition for the droplet ensemble images, while $\lambda = 1.08$ represents the single droplet images. We can clearly see a difference in the first ~ 150 eigenvalues where the contribution for a droplet ensemble is much higher than for a single droplet image. As this represents the complexity of the image, we define the image complexity as

$$\chi = \sum_{n=1}^{150} \alpha_n^2. \tag{3.14}$$

We normalize χ by the mean image complexity χ_{sd} for a range of $\lambda = 1.08$ to $\lambda = 1.79$. The normalized image complexity $\tilde{\chi} = \chi/\chi_{\mathrm{sd}}$ as a function of the trap aspect ratio is shown in figure 3.6b. Due to the normalization, all values of $\tilde{\chi}$ from $\lambda = 1.08$ to $\lambda = 1.79$ are approximately one and most importantly, constant as a function λ. In contrast, we find a strong linear increase for trap aspect ratios from $\lambda = 1.93$ up to $\lambda = 2.62$. We fit this linear curve and extract $\lambda_c = 1.87(8)$ as the value where our fit curve reaches $\tilde{\chi} = 1$. This is in very good agreement with the theoretical predicted value of $\lambda_c \simeq 1.8$, which was discussed in section 2.2.

3.3.2. Critical scattering length

After identifying the critical trap aspect ratio, it is important to study the critical scattering length. For $\lambda < \lambda_c$ the transition from the BEC to the droplet phase is a continuous crossover as can be seen in figure 2.6 such that a measure for a critical a can not be given. We will concentrate on the transition in the bistable region. To do so, we slightly modify the experimental procedure: After creating a BEC, we increase the external magnetic field gradient within $t = 100\,\mathrm{ms}$ to $\nabla B_{\mathrm{earth}} = -2.8\,\mathrm{G/cm}$ and open the trap at the same time. The cloud is held for 20 ms in this new trap with frequencies $(f_\rho, f_z) = (20.5, 80)\,\mathrm{Hz}$. At this point, we have a BEC consisting of typically $N \approx 5{,}000$ atoms. In the following 20 ms we linearly ramp up the power of ODT3 to the desired trap aspect ratio. At the same time we linearly ramp the magnet field closer to the FR to $B = 7.089(5)\,\mathrm{G}$. We hold the cloud for another 20 ms before ramping the magnetic field to various final field values in the range between $B = 7.089(5)\,\mathrm{G}$ and $B = 6.365(5)\,\mathrm{G}$. The atoms are imaged via phase contrast imaging at a detuning of $\Delta_{421} = -5 \cdot \gamma_{421}$ after a final hold time of 20 ms. This procedure is repeated for five different trap aspect ratios between $\lambda = 2$ and $\lambda = 3.9$. We then take 25 images for each combination of magnetic field and trap aspect ratio and perform our statistical analysis. Here, we only sum the eigenvalues with index 7 to 80 to calculate the image complexity χ.

We show the result for $\lambda = 2.3$ in figure 3.7a. To be able to extract a critical scattering length, we fit the image complexity $\chi(B)$ with an error function of the form

$$f_{\mathrm{fit}}(B) = a \cdot \mathrm{erf}\{b \cdot (B - c)\} + d, \tag{3.15}$$

where (a, b, c, d) are the fitting parameters. Here, a represents the amplitude of the error function, $1/b$ its width, which represents the error of the critical magnetic field ΔB_c. The center of the error function and the critical magnetic field B_c are represented by c and d represents an offset. The normalized image complexity is calculated from the fit yielding $\tilde{\chi} = \chi/(d - a)$ such that a BEC gives $\tilde{\chi} = 1$ while structured images show $\tilde{\chi} > 1$.

For the given example, we find $B_c = 6.81(7)\,\mathrm{G}$. We perform the same analysis for the different values of λ and plot the critical magnetic field versus the trap aspect ratio in figure 3.7b as blue points. Additionally, we extracted a critical magnetic field from reference [52] that was measured at $\lambda = 2.96$ (red point). We find it to be slightly higher in critical magnetic field than the other points. One possible reason for this is the much higher atom number as well as the higher trapping frequencies with $N = 15{,}000$ and $\omega_{x,y,z} = 2\pi \cdot (46, 44, 133)\,\mathrm{Hz}$.

Using our knowledge about the scattering length in this area (see figure 3.3) we can convert the critical magnetic fields into critical scattering lengths. This dependence is

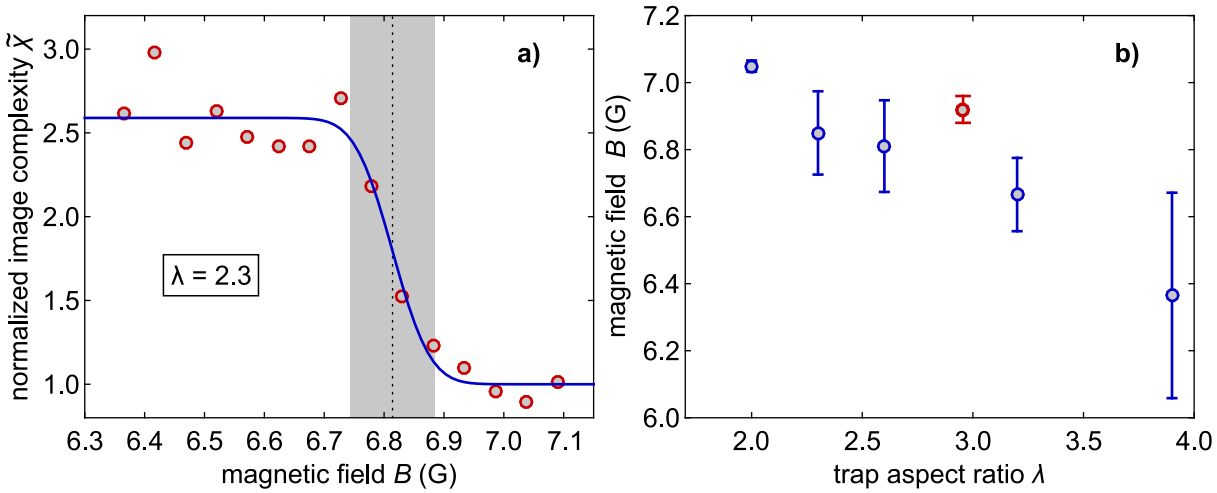

Figure 3.7.: Critical magnetic field: a) We show the normalized image complexity $\tilde{\chi}$ as a function of the applied magnetic field B for a trap aspect ratio of $\lambda = 2.3$ as red circles. At high magnetic fields ($a > a_c$) where we still observe a BEC, we normalize the image complexity to $\tilde{\chi} = 1$. At low magnetic field ($a < a_c$) where we observe droplet crystals, we find that the normalized image complexity settles to $\tilde{\chi} \approx 2.6$. In the intermediate magnetic field region ($a \approx a_c$), the instability process is stochastic and we find a smooth transition from $\tilde{\chi} = 1$ to $\tilde{\chi} = 2.6$. We fit the data with a modified error function given in eq. (3.15) and extract the critical magnetic field B_c (dashed black line) with the error ΔB_c (gray area). **b)** We show the critical magnetic field B_c as a function of the trap aspect ratio λ. The blue data points are the ones taken under the conditions described in the text. The red data point corresponds to the result obtained in [52] with the error bar denoting the width of the observed bistability. For this point, the atom number as well as the trap frequencies were higher with $N = 15.000$ and $\omega_{x,y,z} = 2\pi \cdot (46, 44, 133)$ Hz. These conditions can lead to a shift in the critical magnetic field.

shown in figure 3.8 for two different background scattering lengths. In blue, we plot the critical scattering length for $a_{BG} = 92.5(12.6)\, a_0$, while the red points correspond to $a_{BG} = 62.5(4.7)\, a_0$. The error bars are almost purely coming from systematic errors due to our limited knowledge of the properties of the two FRs. This can be easily seen when comparing the error of ΔB_c and Δa for a given λ.

To interpret the results, we compare the data to the calculated bistability region from a Gaussian ansatz (hatched green area) and extended Gross-Pitaevskii simulations (hatched black area) using our starting conditions mentioned earlier. Considering $a_{BG} = 92.5(12.6)\, a_0$ (blue points), the data seems to match the upper limit of the bistability. We would expect this transition to happen for lower scattering lengths since at this point the energy per particle for a droplet solution is much higher than that of a BEC as was already discussed in section 2.2.1. Indeed, we will see in section 4.3 that the

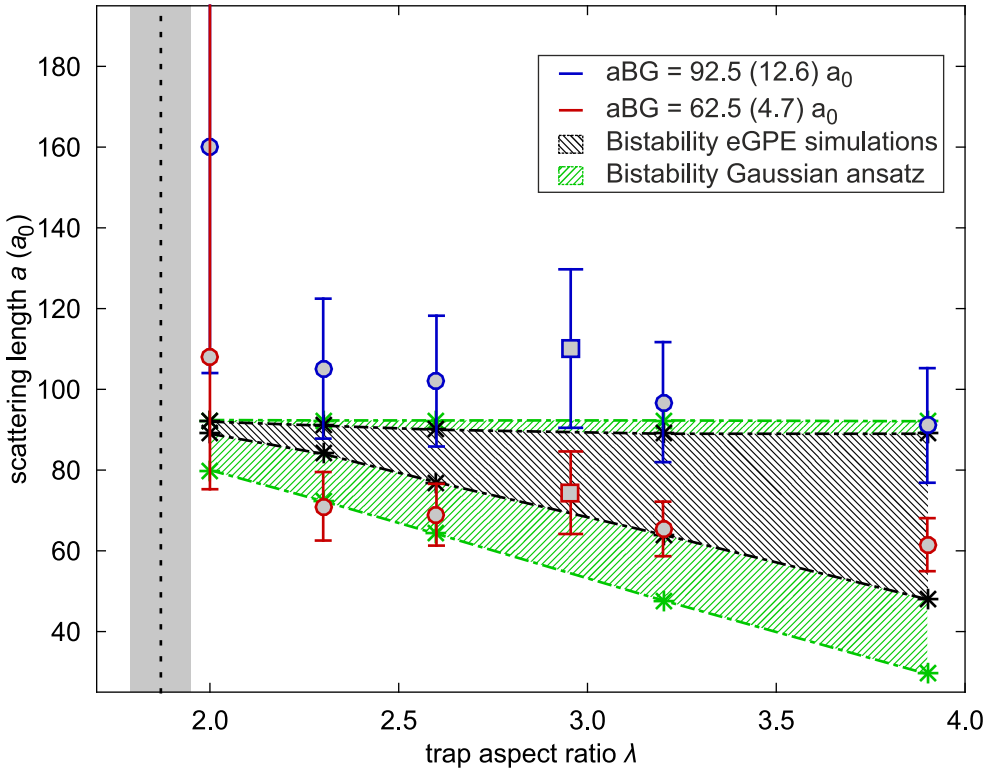

Figure 3.8.: Critical scattering length: We show the critical scattering length a_c as a function of the trap aspect ratio λ calculated for $a_{BG} = 92.5(12.6)\,a_0$ (red circles) as well as $a_{BG} = 62.5(4.7)\,a_0$ (blue circles). We compare these values to calculations of the bistability region from a Gaussian ansatz (hatched green area) and from extended Gross-Pitaevskii simulations (hatched black area) using our experimental parameters. The dashed black line and the gray area correspond to the critical trap aspect ratio λ_c. Comparing the data to the simulations show that the blue circles match the upper limit of the bistability region, while the red circles match the lower limit. Similar as in figure 3.7b, we calculate the critical scattering length for the result obtained in reference [52] as red and blue square.

background scattering length needs to be changed to a value of $a_{BG} = 62.5(4.7)\,a_0$ (red points) to explain the results obtained in that section. At these values, the data seems to match the lower limit of the bistability. To achieve better results for the critical scattering length, we either have to determine the properties of the two FRs more accurately or measure the scattering length in this magnetic field range, for example with the methods presented in [116].

4. Self-bound dilute quantum liquid

In the following chapter we will describe our experimental observations of self-bound droplets that were theoretically described in chapter 2. We will start with a detailed description of the preparation that is based on the results from chapter 3. The subsequent section will present observations on the survival probability of a self-bound droplet as a function of time and scattering length. We will continue with a measurement of the critical atom number and describe our model that is used to extract the critical atom number. We finish this chapter with our determination of the phase diagram in which we identified a phase transition between a self-bound liquid and a gas.

4.1. Preparation of a self-bound quantum droplet

The observation whether a quantum droplet is self-bound can only be done in a trap-free environment. To be able to create a self-bound quantum droplet, we need to prepare it in the most adiabatic way possible [114]. Thus the trap strength must be turned down slowly, and its aspect ratio must be prolate to ensure that the droplet is not deformed before being released. Intuitively, to fulfill the condition for adiabaticity the ramp speed has to be slower than the trap frequency which is impossible to realize as we decrease the trap strength to zero. However, due to the fact that these droplets are almost decoupled from the trapping potential, the important timescale for the ramp speed is given by their collective modes. In the self-bound regime these modes are determined solely by the interactions. From references [114, 116] we know that these collective modes have a typical frequency of a few tens of Hertz, which means that the ramp speed should be at least a few tens of milliseconds.

All our experiments aiming at the preparation and characterization of self-bound droplets start with a harmonically trapped BEC. The BEC preparation is the same as in section 3.2. We start with an atom number of $N = 6{,}000(500)$ at a temperature of $T \approx 20\,\mathrm{nK}$ at a magnetic field value of $B_{\mathrm{BEC}} = 7.089(5)\,\mathrm{G}$. First, we load the BEC into the three-beam crossed optical dipole trap. Within $t = 50\,\mathrm{ms}$ we increase the magnetic field gradient to a value of $\nabla B = 2.9\,\mathrm{G/cm}$ to completely compensate the earth's magnetic field gradient in the gravitational direction. Additionally, during this time we shape

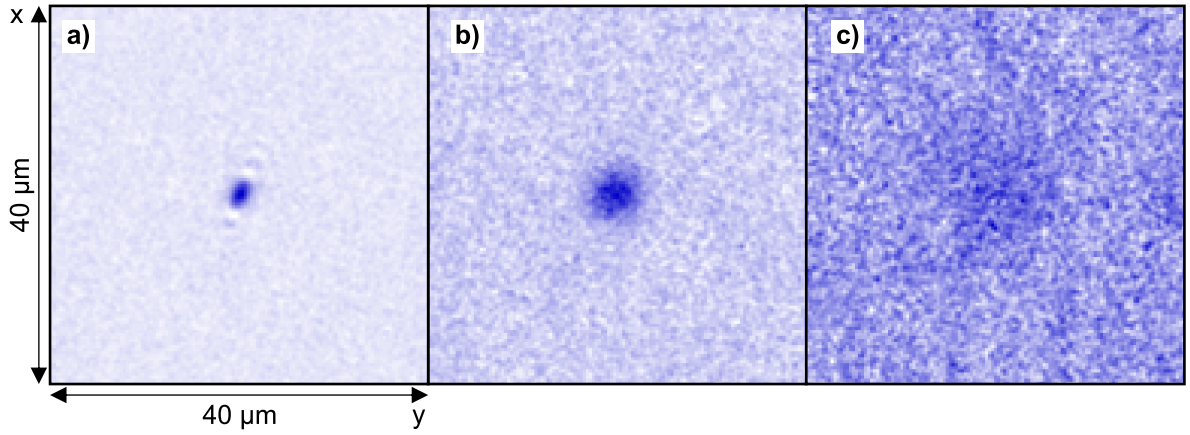

Figure 4.1.: Self-bound droplet measurements: We show three images that were taken at a magnetic field of $B = 6.624(5)\,\mathrm{G}$ after a levitation time of $t_{\mathrm{levitate}} = 50\,\mathrm{ms}$. All images have been rescaled to their maximum optical density and have been re-centered. In **a)**, we observe a self-bound droplet. In **b)** and **c)** we do not find a droplet but rather expanding clouds.

the trapping potential and end up in a trap with measured trap frequencies $\omega_{x,y,z} = 2\pi \cdot (61, 61, 80)\,\mathrm{Hz}$, corresponding to a trap aspect ratio of $\lambda = 1.3$. As we measured in section 3.3.1, the critical trap aspect ratio is at $\lambda_{\mathrm{c}} = 1.87(8)$ which means that we create a single droplet in the chosen trap configuration. At this point, the BEC has a prolate shape with a cloud aspect ratio of $\kappa = 0.66$ and a typical atom number of $N = 3{,}000(300)$[21]. Over the next 50 ms we lower the magnetic field strength to various values within a range of $B = 6.831(5) - 6.469(5)\,\mathrm{G}$ to decrease the scattering length and create a single droplet. We hold the atoms in this configuration for another 10 ms. Within the next 20 ms the three traps are ramped linearly to final trapping frequencies of $\omega_{x,y,z} = 2\pi \cdot (20, 25, 21)\,\mathrm{Hz}$, giving a trap aspect ratio of $\lambda = 1$ and a potential depth of $U_0 = -80\,\mathrm{nK}$.

We observe that despite being rather fast in principle, this ramp does not induce any notable oscillations. On the other hand, the low ramp time prevents high atom loss through three-body recombination. At this point, we suddenly turn off the trapping potential and freely levitate the atoms with the magnetic field gradient. We image the cloud after various levitation times of up to $t_{\mathrm{levitate}} = 90\,\mathrm{ms}$ using red-detuned phase-contrast polarization imaging at a detuning of $\Delta_{421} = -5 \cdot \gamma_{421}$. We show a few example images at a magnetic field of $B = 6.624(5)\,\mathrm{G}$ after a levitation time of $t_{\mathrm{levitate}} = 50\,\mathrm{ms}$ in figure 4.1. All images are rescaled to their maximum optical density and have been recentered. The first image (4.1a) shows a cloud that we identify as self-bound droplet since it is smaller than the resolution of our imaging system. As a result we see astigmatic

[21] Not all atoms are found within the BEC phase. Due to the low temperatures we cannot distinguish between thermal atoms and those within the BEC.

aberration effects. We see an expanded cloud on the second image in figure 4.1b. Fitting a Gaussian distribution to this profile yields a $1/e^2$ size of $\sigma_{x,y} = 1.95(5)\,\mu$m. Assuming a linear growth [54] at the beginning of the levitation time and an initial size[22] of $\sigma_0 = 300\,$nm this leads to a growth rate of $\dot{\sigma}_{x,y} = 33(1)\,$nm/ms. Assuming a thermal cloud, this size would yield a temperature of $T = 30\,$pK. Both calculations tell us that this cloud must have been a self-bound droplet that evaporated at some point during the levitation process. In this context, 'evaporation' is used to denote the transition from a dilute self-bound liquid state to an unbound gas phase. We barely see atoms on the third image (figure 4.1c). Again, fitting with a Gaussian distribution yields a size of $\sigma_{x,y} = 5.0(5)\,\mu$m. With the same initial size as before, this yields a growth rate of $\dot{\sigma}_{x,y} = 94(10)\,$nm/ms or a thermal gas temperature of $T = 200\,$pK. Since all droplets are released from the very same trapping potential, we would assume that they should have the same growth rate after evaporating back into the gas phase. The only possible explanation is that the droplets evaporated at different times during the levitation and the one shown in figure 4.1c evaporated much earlier than the one in b. In the next sections, we show two methods to analyze the self-bound character.

4.2. Survival probability against scattering length

To quantitatively characterize these self-bound droplets and determine the conditions for their existence, we count the images in which we observe a single droplet. This is done for variable hold time between $t_{\text{levitate}} = 0\,$ms and $t_{\text{levitate}} = 90\,$ms and variable magnetic field values between $B = 6.572(5)\,$G and $B = 6.676(5)\,$G. We show two image sequences for a magnetic field of $B = 6.676(5)\,$G where the levitation time is varied in figure 4.2. These images are not multiple images of the same cloud but rather single realizations since the imaging process is destructive. In these images, the expansion dynamics after the evaporation of a droplet is not measured since we do not know the exact time at which a droplet evaporated, but rather shows a trend of what we expect to happen. The two sequences are given for two different initial atom numbers. For all realizations, we observe that the droplet is surrounded by a cloud at $t_{\text{levitate}} = 0\,$ms that quickly expands for longer levitation times. The upper row demonstrates the evolution of a droplet that starts with an atom number much larger than the critical atom number $N \gg N_{\text{crit}}$ such that its lifetime is between $t = 70\,$ms and $t = 90\,$ms. The lower row shows a droplet with an atom number much closer to the critical atom number $N > N_{\text{crit}}$ resulting in a much shorter lifetime between $t = 20\,$ms and $t = 50\,$ms. We take 100 realizations for

[22] This value is consistent with our effective GPE simulations.

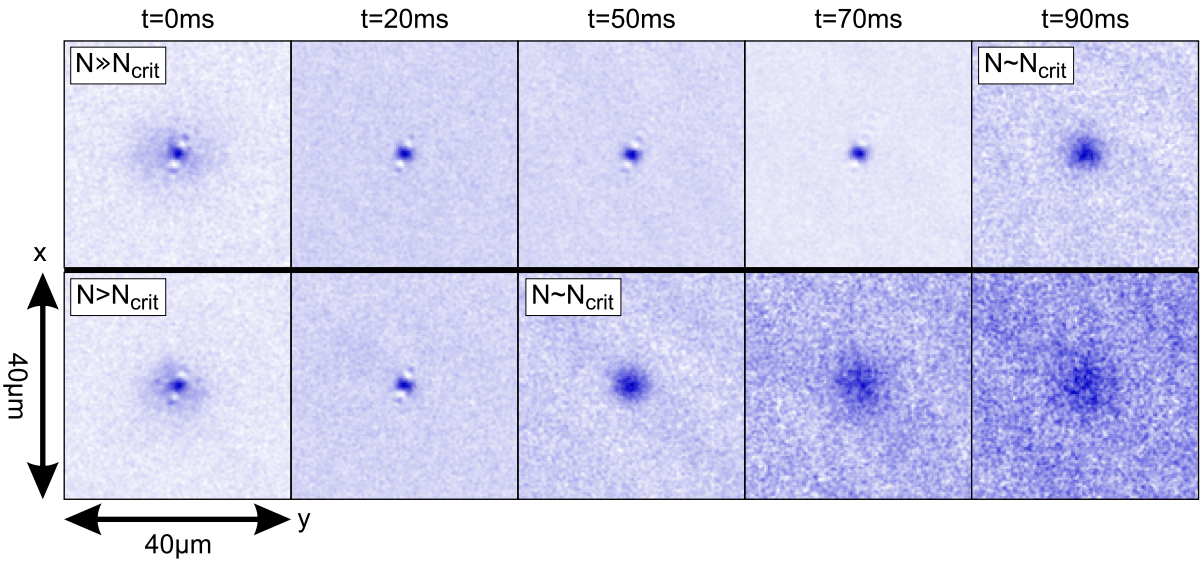

Figure 4.2.: Droplet survival vs. levitation time: We show two image sequences of droplets with different levitation times at the same magnetic field $B = 6.676(5)\,\mathrm{G}$. These two sequences do not show multiple images of the same droplet, but are selected from various images as the imaging process is destructive. All images are rescaled to the maximum optical density and have been re-centered. In the upper row, we start with an atom number that is much larger than the critical atom number and observe a single droplet up to $t_{\mathrm{levitate}} = 70\,\mathrm{ms}$. Between $t = 70\,\mathrm{ms}$ and $t = 90\,\mathrm{ms}$, the droplet reaches the critical atom number and evaporates back to the unbound gas phase and expands. In the lower row, the droplet starts with an atom number that is much closer to the critical atom number, leading to an earlier evaporation, between $t = 20\,\mathrm{ms}$ and $t = 50\,\mathrm{ms}$ of levitation time. From this point in time on, the cloud evaporates to the BEC phase observed as an expanding cloud.

each combination of levitation time and magnetic field. Since these droplets are smaller than our imaging resolution, we observe astigmatic diffraction and we use this aberration to differentiate a self-bound droplet from an expanding cloud. This counting technique overestimates the number of self-bound droplets. A cloud that evaporated right before the imaging process will still be smaller than our resolution and be identified as droplet.

We show a histogram of the survival probability as a function of magnetic field and levitation time in figure 4.3. At low magnetic fields ($B \leqslant 6.676(5)\,\mathrm{G}$), we always start with an atom number that is higher than critical atom number ($N \gg N_{\mathrm{crit}}$), such that we always create a droplet. This can be seen in a survival probability of 100 % for a levitation time $t_{\mathrm{levitate}} = 0$. The survival probability already drops at $t_{\mathrm{levitate}} = 0$ for high magnetic fields ($B \geqslant 6.727(5)\,\mathrm{G}$). Here, the initial atom number seems to be on the order of the critical atom number ($N \sim N_{\mathrm{crit}}$), such that we sometimes do not create a droplet but rather only release a trapped BEC. This is a first hint on the absolute scattering

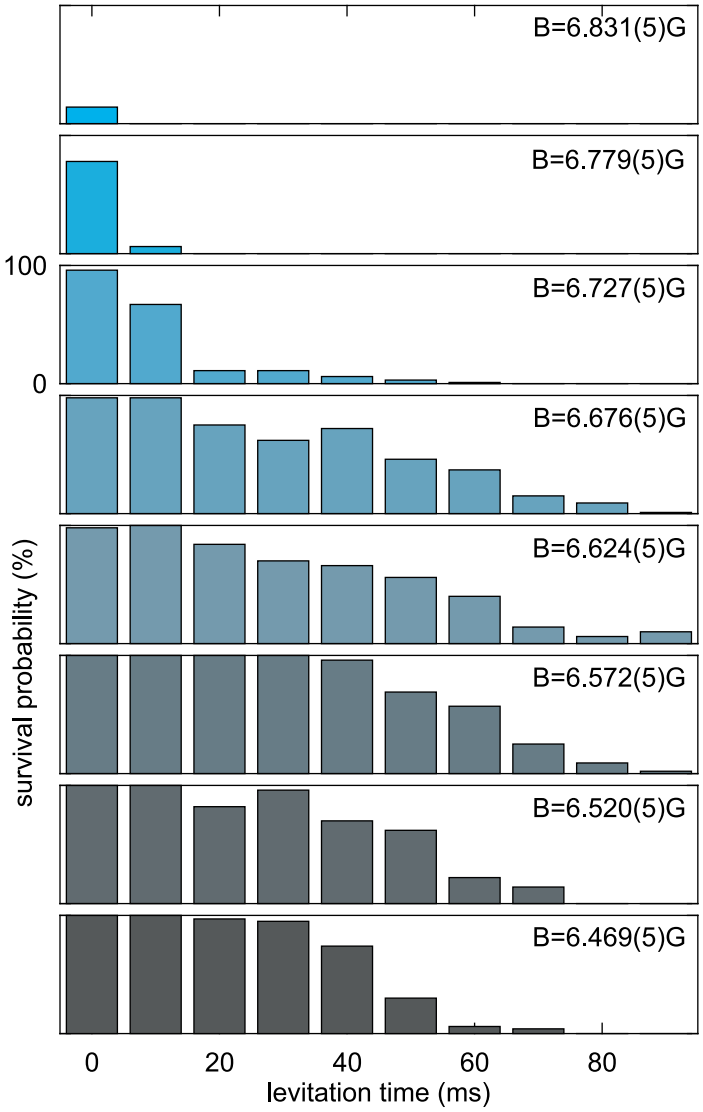

Figure 4.3.: Self-bound droplet survival probability: Histogram of the survival probability of a single droplet as function of levitation time and magnetic field. At low magnetic field $B = 6.469(5)\,\mathrm{G}$, we observe a 100 % survival probability up to $t_{\mathrm{levitate}} = 30\,\mathrm{ms}$, followed by a fast decay. For increasing magnetic field, we observe an increase in the lifetime up to a magnetic field range of $B = 6.572(5) - 6.676(5)\,\mathrm{G}$. Increasing the scattering length even further leads to a fast decay of self-bound droplets even for short times ($t_{\mathrm{levitate}} = 20\,\mathrm{ms}$). We barely create droplets in the trap at the highest measured magnetic field of $B = 6.831(5)\,\mathrm{G}$.

length at this magnetic field: At $B = 6.831(5)\,\mathrm{G}$ we measure a survival probability for the self-bound droplet at $t = 0\,\mathrm{ms}$ of 16 %. With $N \sim N_{\mathrm{crit}}$ and the assumption that our droplet consists of less than $N = 3{,}000$ atoms, we can assign this critical atom number to a scattering length using the methods described in section 2.3. We find that the scattering length must be smaller than $a = 84\,a_0$. Recalling figure 3.3, we calculated a scattering

length at this magnetic field that is given as $a = 1.11 \cdot a_{\mathrm{BG}}$. This results a background scattering length that must be smaller than $a_{\mathrm{BG}} = 75\,a_0$ which is in very stark contrast to the assumed background scattering length of $a_{\mathrm{BG}} = 92.5(12.6)\,a_0$, recalling section 3.1. We will tackle this discrepancy in the next section in more detail.

In addition, we observe a variation in the time-dependence of the fraction of surviving droplets. While the lifetime for low magnetic field ($B = 6.469(5)\,\mathrm{G}$) appears to be very short, we observe an increase in lifetime up to a magnetic field of $B = 6.676(5)\,\mathrm{G}$. At this field we observed a single droplet with a size below our resolution after a levitation time of up to $t_{\mathrm{levitate}} = 100\,\mathrm{ms}$. Even higher magnetic fields cannot be taken into account for reasons that we discussed earlier. The increase in lifetime can be explained by the following reasons. Firstly, we know that the scattering length increases with magnetic field, again recalling figure 3.3. Consequently, the density in a droplet decreases, leading to reduced three-body losses. This behavior has also been observed by earlier measurements in a waveguide configuration [54] and for a single trapped droplet using erbium atoms [116], and is supported by calculations on a self-bound droplet [114, 115]. However, three-body loss does not only scale with the density but also with the three-body loss rate L_3

$$\frac{1}{N}\frac{\mathrm{d}N}{\mathrm{d}t} = -L_3\langle n^2\rangle, \tag{4.1}$$

with the mean density $\langle n^2\rangle$. Here, we ignore one-body losses that result from collisions with the background gas since these losses only play a role on much longer timescales. We also neglect two-body losses that result from spin-exchange collisions or dipolar relaxations as we work with a spin-polarized sample [11]. L_3 depends on the magnetic field, close to a FR it scales as a^4 [117, 133].ends on the magnetic field, close to a FR it scales as a^4 [117, 133]. Away from a resonance pole, this dependence breaks down and another length scale replaces a, typically the effective range or the van-der-Waals length r_{vdW} [134, 135]. However, the exact value and dependence of L_3 is hard to predict. As a consequence, in order to relate the lifetime of a droplet to its mean quadratic density through eq. (4.1), L_3 has to be measured in the relevant magnetic field range. We have performed these measurements in the magnetic field range $B = [6.469(5), 6.676(5)]\,\mathrm{G}$ and observed the three-body loss rate to vary only weakly, between $L_3 = [0.8 \cdot 10^{-40}, 1.1 \cdot 10^{-40}]\,\mathrm{m}^6/\mathrm{s}$. As a consequence, any strong variation in lifetime is mostly due to a variation in density.

To theoretically describe the time evolution of the survival probability, we create the following model: we start with an atom number distribution that follows a Gaussian distribution

$$p_0(N) = \frac{1}{\sqrt{2\pi\Delta N^2}}\exp\left(-\frac{(N-N_0)^2}{\Delta N^2}\right), \tag{4.2}$$

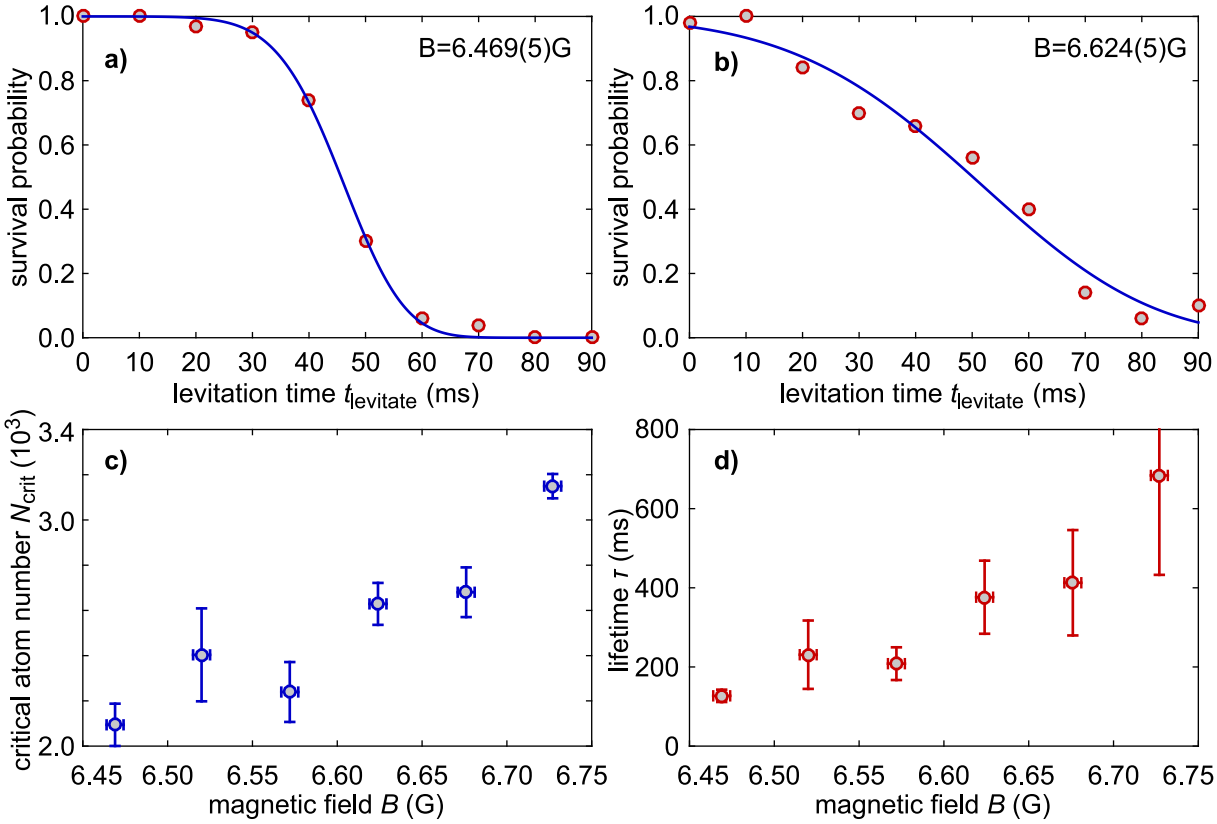

Figure 4.4.: Survival probability analysis: a) & b) We show two examples where a clear difference in N_{crit} and τ is visible. For a magnetic field of $B = 6.469(5)\,\text{G}$, shown in **a)**, we find a smaller critical atom number as well as lifetime as for a magnetic field of $B = 6.624(5)\,\text{G}$, shown in **b)**. The blue curve shows a fit of our model from eq. (4.4) to the measured data points (red circles) for $t_{\text{levitate}} = 20 - 90\,\text{ms}$. **c)** For all different magnetic fields, we extract the critical atom number and plot it versus magnetic field. We find an increase of N_{crit} for increasing magnetic field. The same behavior can be seen in **d)**, where we plot the lifetime against magnetic field. Since our initial atom number is similar to the critical atom number at high magnetic fields ($B \geqslant 6.779(5)\,\text{G}$) the fit model fails as the survival probability is zero for all levitation times. The error bars in the two lower plots describe one standard deviation.

with the mean atom number N_0 and the width in atom number ΔN. This distribution represents the shot-to-shot noise of our experiment. For simplicity, we assume that the time evolution of N follows a single exponential decay $N(t) = N\exp(-t/\tau)$, with τ being the lifetime. Inserting this into eq. (4.2) yields the time dependent probability

$$p_1(N,t) = \frac{1}{\sqrt{2\pi\Delta N^2}}\exp\left(-\frac{\left(\frac{N(t)}{\exp(-t/\tau)} - N_0\right)^2}{\Delta N^2}\right). \tag{4.3}$$

By integrating eq. (4.3) over the atom number, we define the survival probability $SP(t)$ as

$$\begin{aligned} SP(t) &= \frac{\int_{N_{\mathrm{crit}}}^{\infty} \mathrm{d}N\, p_1(N,t)}{\int_0^{\infty} \mathrm{d}N\, p_1(N,t)} \\ &= \frac{1+\mathrm{Erf}\left(\frac{N_0-\exp(t/\tau)N_{\mathrm{crit}}}{\Delta N}\right)}{1+\mathrm{Erf}\left(\frac{N_0}{\Delta N}\right)}, \end{aligned} \tag{4.4}$$

with the critical atom number N_{crit} and $\mathrm{Erf}(x)$ being the error function. By fitting eq. (4.4) to data presented in figure 4.3, we can extract a lifetime τ, as well as a critical atom number N_{crit}. We only fit the data starting from $t_{\mathrm{levitate}} = 20\,\mathrm{ms}$. The reason for this can be seen in the survival probability for a magnetic field of $B = 6.727(5)\,\mathrm{G}$ where we seem to have two different timescales, a fast decay at the beginning followed by a longer lifetime. We interpret this to stem from the fact that our initial atom number is too close to the critical atom number. We show two examples in figure 4.4a and b for a magnetic field of $B = 6.469(5)\,\mathrm{G}$ and $B = 6.624(5)\,\mathrm{G}$, respectively. We see that our model is able to represent the measured data points well and the extracted critical atom number as well as the lifetime are shown in figure 4.4c and d, respectively. When we compare the extracted lifetime of $\tau = 127(15)\,\mathrm{ms}$ for a magnetic field of $B = 6.469(5)\,\mathrm{G}$ with the plot in figure 4.4a, we find a big discrepancy that hints to the drawback of this model. It results from the fact, that N_{crit} as well as τ are strongly dependent on the initial atom number as well as the spread in atom number. Nevertheless, the model is able to extract the correct tendencies as we see an increase in critical atom number, as well as an increase in lifetime for increasing magnetic field (scattering length).

Additionally, this ansatz assumes that all droplets evaporate as soon as they reach the critical atom number. This means it ignores the possibility of a droplet to evaporate before reaching N_{crit}, as well as droplets that still survive, even though their atom number is already lower than N_{crit}. Such 'super-critical' evaporation events can be explained by residual excitations in the droplets. On the other hand, the evaporation rate for a 'sub-critical' droplet should increase strongly since the quantum pressure term starts to dominate and the balance between attraction and repulsion is not given anymore.

While the method presented thus far based on the modeling of the survival probability allows to clearly demonstrate the trends in terms of lifetime and critical atom number, it does not allow for a model-independent, quantitative determination of these quantities. The next section overcomes these limitations for the determination of the critical atom number by profiting from the natural atom loss occurring in the droplets.

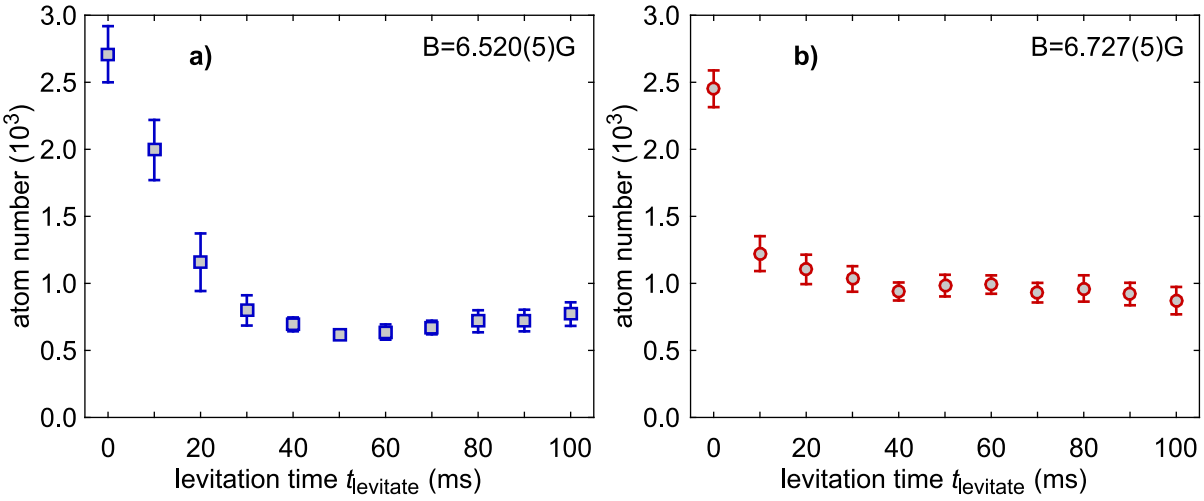

Figure 4.5.: Lifetime evaporated droplets: We show two traces for the atom number N as a function of the levitation time t_{levitate}. In **a)** we plot the decay at a magnetic field of $B = 6.520(5)\,\mathrm{G}$ that results in a lower atom number offset as the decay curve in **b)** where the magnetic field is $B = 6.727(5)\,\mathrm{G}$. Each point is a mean value of 20 different realizations with the error bar denoting one standard deviation.

4.3. Direct measurement of the critical atom number

In this section, we will describe the protocol that we developed to measure the critical atom number. This atom number counting cannot be faithfully obtained when the droplets are self-bound since they have a size smaller than our imaging resolution, together with a very high density. We thus need to dilute the droplets to obtain a sufficiently large size and low density. To do so, we intentionally evaporate the droplets and let them expand for a short time. The experimental sequence that realizes this is as follows: after turning the dipole traps off, we levitate the droplets for a variable levitation time of up to $t_{\mathrm{levitate}} = 100\,\mathrm{ms}$. After the levitation, we linearly increase the magnetic field to $B = 6.986(5)\,\mathrm{G}$ within $t = 100\,\mu\mathrm{s}$. At this magnetic field value, the critical atom number is higher than all observed atom numbers. This is to ensure that we always evaporate the droplets. The cloud freely expands at this field for $t = 10\,\mathrm{ms}$ before we image the atoms using absorption imaging with resonant light on the $\lambda = 421\,\mathrm{nm}$ transition. Figure 4.5 shows the atom number as a function of levitation time for two different magnetic fields. For both fields, we see that the atom number decays very fast to an almost constant offset. We also see that the offset is different for the two different magnetic fields. At low magnetic field ($B = 6.520(5)\,\mathrm{G}$), we observe a lower offset in atom number as compared to the higher magnetic field at $B = 6.727(5)\,\mathrm{G}$. The appearance of this almost constant offset at long times can be explained as follows: Initially, the droplets are self-bound and dense, hence losing atoms through three-body recombination. Once the atom number reaches the critical atom number for

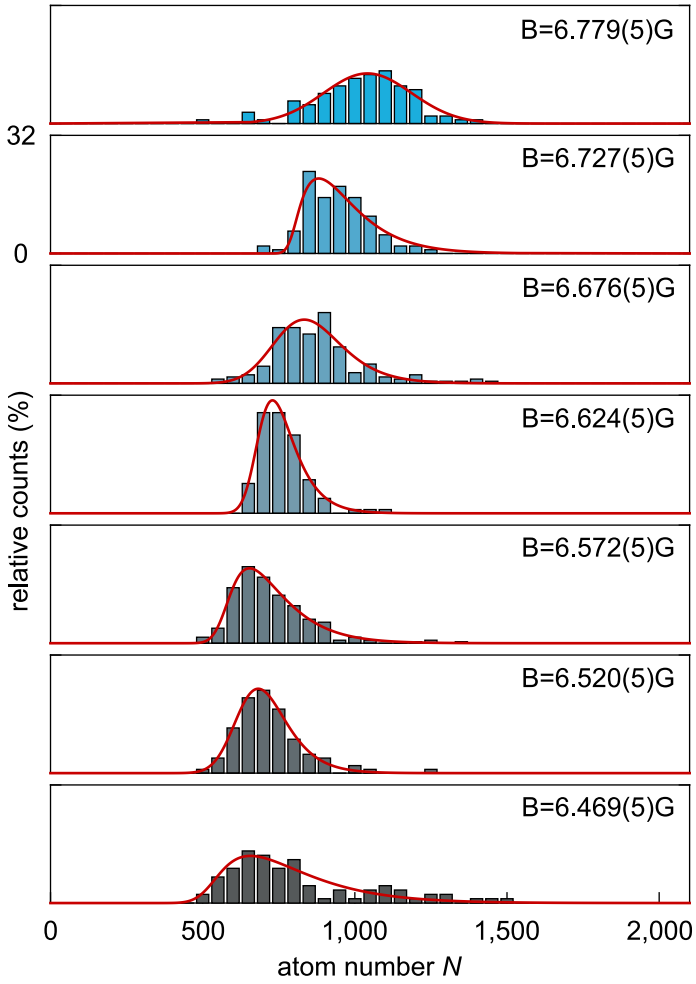

Figure 4.6.: Critical atom number: Analysis of the atom number distributions for levitation times in the range $t_{\text{levitate}} = 60 - 100\,\text{ms}$ as the atom number is mostly constant in this range. The atom number is binned to a window of 50 atoms and we show the relative counts as a function of atom number for various magnetic fields. The fits of the convoluted functions to the observed histograms are shown as red curves. The colors of the plotted histograms match those in figure 4.3, and represent the magnetic field.

the existence of the self-bound state, it evaporates to the gas phase and starts to expand. As soon as this expansion starts to take place the density is lowered drastically and three-body losses are suppressed such that the atom number stays constant. Following this idea, the offset in atom number must be directly connected to the critical atom number. To analyze this effect, we create a histogram of the atom number for levitation times $t_{\text{levitate}} \geqslant 60\,\text{ms}$. Here, we bin the atom number and plot their relative counts as a function of atom number and magnetic field in figure 4.6. To interpret these histograms, we create a phenomenological model that consists of a convolution of a Gaussian distribution

and a Maxwell-Boltzmann distribution. The symmetric Gaussian distribution represents broadening effects that result from statistical errors including detection noise as well as the spread in initial atom number. The asymmetric Maxwell-Boltzmann distribution is used to model the fact that possibly super-critical droplets ($N > N_{\mathrm{crit}}$) could evaporate into the gas phase before reaching the critical atom number due to the presence of energetic excitations, for instance collective modes. The corresponding convolution reads

$$\begin{aligned} f(N) =& \frac{\sigma}{\sqrt{2\pi}\Delta N^2} \exp\left(-\frac{(N-N_{\mathrm{crit}})^2}{2\sigma^2}\right) \\ & \left[1+\sqrt{\pi}g(N-N_{\mathrm{crit}})\exp\left(g(N-N_{\mathrm{crit}})^2\right)\left\{\mathrm{Erf}\Big(g(N-N_{\mathrm{crit}})\Big)-1\right\}\right], \end{aligned} \tag{4.5}$$

with the width of the Gaussian distribution σ, the width of the Maxwell-Boltzmann distribution ΔN and $g(N) = \frac{1}{\sqrt{2}}\left(\frac{\sigma}{\Delta N} - \frac{N}{\sigma}\right)$. We interpret the quadratic mean of the two widths as error in the critical atom number. Fitting this function to the histograms in figure 4.6 allows us to extract N_{crit}, σ and ΔN. We show the resulting fits as red curves in figure 4.6. The extracted values are plotted in figure 4.7 against the magnetic field. Although we observe large error bars for the critical atom number, we find a clear trend of an increasing N_{crit} for increasing magnetic field. More importantly, this method does not depend on any guess of the initial atom number as it only relies on absolute atom number measurements.

The measured critical atom number as a function of the scattering length $N_{\mathrm{crit}}(a)$ represents the phase transition line between a dilute liquid phase and a gas phase, shown in figure 4.7. This phase, that only exists for a cloud with large atom number ($N > N_{\mathrm{crit}}$) is called a dilute liquid phase for several reasons: As we calculated in chapter 2, these quantum droplets share many properties with those of a quantum liquid, being a vanishing compressibility, a saturating peak density for increasing atom number, surface tension and the possibility of creating self-bound droplets. Our measurements on the self-bound character as well as the existence of a critical atom number was the first experimental confirmation of the liquid character. Collective oscillation measurements performed with erbium droplets [116] could show that the monopole mode is weakened deep in the droplet regime, indicating a vanishing compressibility. However, the typical classification of a quantum liquid requires strong correlations. For our system, this means that the quantum fluctuations term has to be large, or $na^3 > 1$. Compared to liquid ^{4}He droplets, the density is rather low such that we do not fulfill this condition and calculate $na^3 \approx 10^{-3}$. Nevertheless, it is correlations that stabilize the quantum droplets and determine its properties. Due to these reasons, the quantum droplets cannot be connected to the gas phase. As soon as the droplets fully evaporate, the cloud can be categorized as a gas again

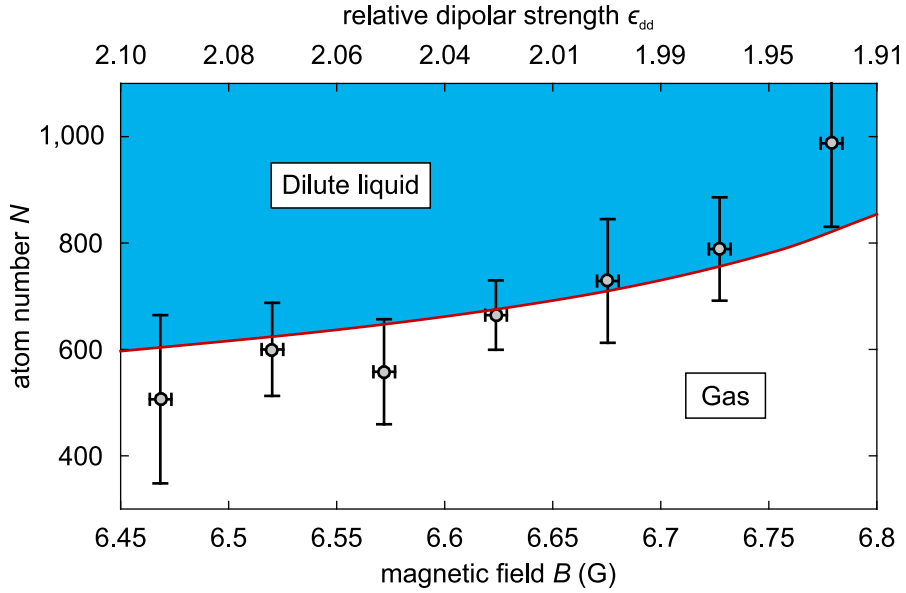

Figure 4.7.: Phase transition between dilute liquid and gas: The data points show the critical atom number as a function of the magnetic field that were determined from the fit values from figure 4.6. The error in the atom number is given by the quadratic mean of the widths of the Gaussian and Maxwell-Boltzmann distributions plus a 10 % error that may result from our atom number determination; the error in magnetic field describes the resolution of our magnetic field coils. The critical atom number N_{crit} decreases with the magnetic field. The upper-left corner is identified as the dilute liquid phase and the lower-right corner as the gas phase. The critical atom number thus marks the phase transition between the dilute liquid phase and the gas phase. We show full Gross-Pitaevskii simulations for different relative dipolar strengths $\varepsilon_{\mathrm{dd}}$ as red solid line.

as it freely expands in the absence of a trapping potential. This is the case for low atom numbers ($N < N_{\mathrm{crit}}$) and for scattering lengths that are larger than the dipolar length as was shown in figure 2.8b. For the small parameter range studied here, we could thereby deduce the phase diagram for an untrapped dipolar gas.

These directly measured critical atom numbers can now be compared to our effective GPE simulations. To do so, we first calculate the critical atom number as a function of the scattering length, as was done in figure 2.8b using the Gaussian ansatz. This gives us a numerical function for $N_{\mathrm{crit}}(a)$, or vice versa $a(N_{\mathrm{crit}})$. Thus using our measurements of $N_{\mathrm{crit}}(B)$, we can obtain an experimental value of $a(B)$, based on either the effective GPE simulations or the Gaussian ansatz. Although this determination of the scattering length is thus model-dependent, the simulations of the effective GPE are more accurate than the Gaussian ansatz, which we ignore here. In a next step we compare the obtained dependence for $a(B)$ with our knowledge of the local scattering length dependence that is based on the overlapping-resonances model of [122], shown We find that the extracted

scattering lengths (red points) are much lower than the calculated scattering length using $a_{\mathrm{BG}} = 92.5(12.6)\,a_0$ (black solid line), confirming the observed trend in section 4.2.

Typically, the most difficult part in the determination of a is to obtain a_{BG}. We described a few different methods to obtain a_{BG} in section 3.1, all of them having different drawbacks. Recent measurements on erbium atoms using a lattice technique to measure the scattering length [116] provide very accurate results but this technique has not been performed with dysprosium atoms yet. If we use the scattering length values extracted from the critical atom number measurements, we can obtain a value of a_{BG}. To do so, we fit these data to the local scattering length dependence using the background scattering length as a single fit parameter. With this we can obtain a measurement of a_{BG}, keeping in mind that it is model dependent. We show our best fit for $N_{\mathrm{crit}}(B)$ in figure 4.7 as red solid line. The same fit is shown in figure 4.8 for $a(B)$ as red solid line. Here, the fitted background scattering length is

$$a_{\mathrm{BG}} = 62.5(2.4)\,a_0. \tag{4.6}$$

The error in a_{BG} comes from a sum of the systematic error and the statistical error. The systematic error results from a conservative assumption that our atom number detection has an error of 10 %, while the statistical error results from the fit. This analysis agrees well with the prior analysis in section 4.2, recalling $a_{\mathrm{BG}} < 75\,a_0$. Using the assigned scattering lengths, we can calculate the relative dipolar strength using equation (1.10). We show these values in figure 4.7 as upper x-axis and calculate a relative dipolar strength at the background scattering length of

$$\varepsilon_{\mathrm{dd}} = 2.09(8). \tag{4.7}$$

We finally use the new value of $a_{\mathrm{BG}} = 62.5(2.4)\,a_0$ to calculate the critical scattering length in section 3.3.2.

The disagreement between the new background scattering length of $a_{\mathrm{BG}} = 62.5(2.4)\,a_0$ and the one that we introduced in section 3.1, recalling $a_{\mathrm{BG}} = 92.5(12.6)\,a_0$, is enormous. in figure 4.8. However, the complexity of the scattering problem in dysprosium does not allow for a theoretical prediction of the absolute scattering length and the local background scattering length might vary in other ranges of magnetic field. Additionally, a comparison of our measurements on the Rosensweig instability [52] with theoretical simulations [88, 90] showed a discrepancy of the critical scattering length, suggesting that a background scattering length of less than $a_{\mathrm{BG}} = 92.5\,a_0$ is necessary. Due to the strong dependence of N_{crit} on the scattering length, these measurements provide a very high sensitivity

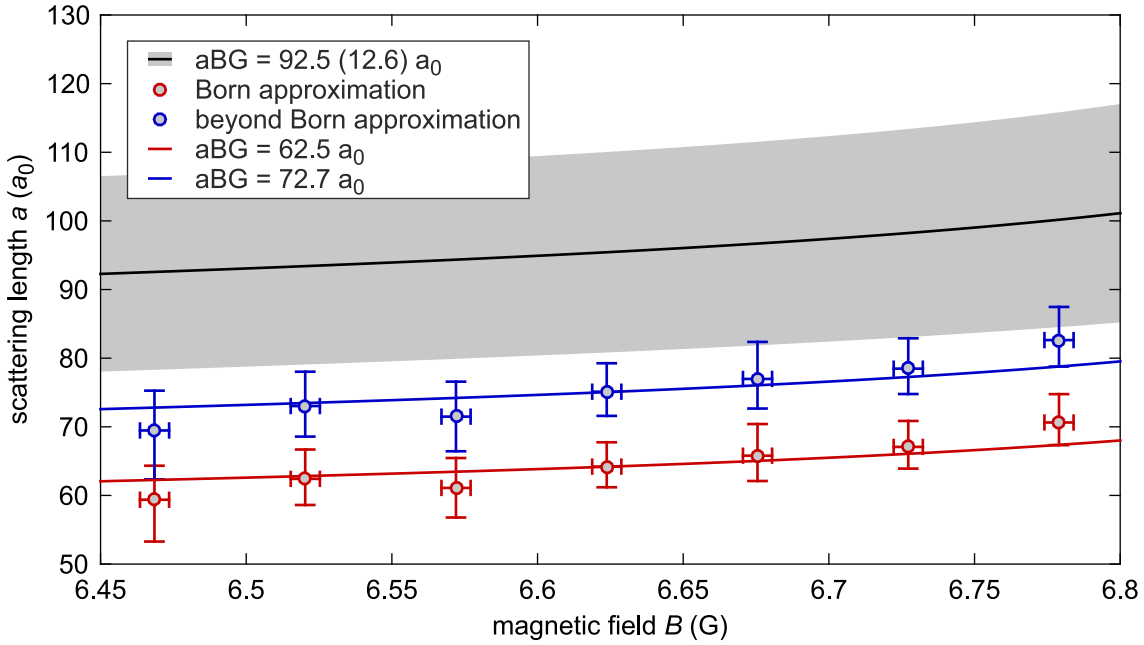

Figure 4.8.: Revision of the background scattering length: We plot the extracted values for the scattering length a as a function of the magnetic field B. We compare the results with our calculations on the scattering length (black solid line and gray area) from figure 3.3b assuming $a_{\mathrm{BG}} = 92.5\,a_0$. The red points show the scattering length assuming the first-order Born approximation. A fit (red solid line) to these values yields $a_{\mathrm{BG}} = 62.5\,a_0$. The revised scattering amplitude from calculations beyond the Born approximation yield to the blue points. The same fitting procedure yields $a_{\mathrm{BG}} = 72.7\,a_0$ (blue solid line). The error in a is calculated from the error in N_{crit} from figure 4.7; the error in B describes the resolution of our magnetic field coils.

and enable precise measurements on the scattering length. Changing the background scattering length from $a_{\mathrm{BG}} = 92.5\,a_0$ to $a_{\mathrm{BG}} = 62.5\,a_0$ reduces N_{crit} by almost a factor of ten. However, at this level of precision, we must question the approximations made in our model, such as the first-order Born approximation for the dipolar scattering and the local density approximation. This means that the value of the background scattering length is dependent on the model that is used to calculate the critical atom number. On the other hand, an independent measurement of the scattering length via the methods presented in reference [116] would make these N_{crit} measurements a very sensitive benchmark for future many-body theories.

Indeed, the presented results motivated new theoretical work to calculate the scattering amplitudes beyond the Born approximation [78]. These calculations apply for all lanthanides with high magnetic moment. In this work a realistic interaction model is used to calculate a modified pseudopotential for the dipolar interaction. Using this modified

pseudopotential the authors see that the characteristic dipolar length is not a constant value for all scattering lengths but rather changes as a function of a. In the parameter range studied here, the authors calculate an enhancement of the dipolar length of 17 %. This change in a_{dd} is not negligible and has a direct influence on our measurements as it basically enhances the scattering length by the 17 %. We calculate the dependence of $a(B)$ using the 17% increased scattering length and plot the extracted scattering lengths in figure 4.8 as blue points. Performing the same fitting procedure we can extract a revised background scattering length for beyond Born approximation that reads

$$a_{\mathrm{BG}} = 72.7(2.9)\, a_0. \tag{4.8}$$

The resulting fit for $a(B)$ is shown in figure 4.8 as blue line. Although this new value lies closer to the previously assumed $a_{\mathrm{BG}} = 92.6\, a_0$, the mismatch is still large calling for an independent measurement of the scattering length.

Conclusion and Outlook

Conclusion

In this thesis, we have presented the experimental observation of a self-bound dilute quantum liquid that is formed from an ultracold atomic gas. The results build up on our findings that a dysprosium Bose-Einstein condensate does not simply collapse for low scattering lengths as is predicted in the framework of mean-field theory. The cloud rather forms quantum droplets that are stabilized by beyond mean-field effects; the so-called quantum fluctuations. These droplets are the first self-bound system formed from an ultracold atomic gas and may thus open up a completely new research direction.

We were only able to observe these fascinating results thanks to the design of our experimental apparatus. The combination of a glass cell with high optical access, a high resolution imaging system and the possibility to almost arbitrarily change the trapping potential was key to a precise control of the external properties of the cloud. In addition, the precise magnetic field control allowed for a high tunability of the internal properties.

Using these experimental tools, we started by studying the properties of a trapped dysprosium BEC as a function of scattering length and trap aspect ratio. This study lead to a phase diagram, where we identified three different phases: the BEC phase, the droplet phase and a bistability phase where BEC and droplet phase coexist. Prior to this thesis we observed that under certain conditions a dysprosium BEC splits up into several stable quantum droplets. Based on this result, we were able to reveal that this droplet crystal only forms for trap aspect ratios that are higher than a critical trap aspect ratio. We measured this critical trap aspect ratio to be $\lambda_c = 1.87(8)$ which is in very good agreement to the theoretically calculated value. Variational calculations using the Gaussian ansatz showed that the transition from a BEC to the droplet crystal is a first-order phase transition following Ehrenfest and that this transition happens in the bistability phase. Furthermore, we measured the critical scattering length which describes the point where the BEC splits into a droplet crystal as a function of the trap aspect ratio in the bistability phase. In contrast, for trap aspect ratios smaller than the critical trap aspect ratio, we observed a continuous crossover from the BEC phase to the droplet phase. This crossover results in the true ground state of the droplet phase being a single droplet.

The droplet phase provides interesting properties. While a BEC is still in the gas phase and shares most of its properties with the ones of an ideal gas, a quantum droplet shares more properties with a liquid. Firstly, it is almost completely decoupled from the trapping potential. This was seen as the peak density of a droplet is not affected by a compression through the trapping frequencies, which was calculated using the Gaussian ansatz. Secondly, for high atom numbers in a droplet we observe the effect of surface tension, very similar to the case of quantum droplets of liquid ^{4}He. And lastly, the droplets are self-bound, removing the necessity of a trapping potential.

We observed and systematically studied the self-bound character. Making use of a magnetic field gradient lead to a levitation of the self-bound droplets that allowed us to observe them for various times without a trapping potential. With this technique we first measured the survival probability as a function of scattering length and levitation time. Here, we observed the existence of a critical atom number and that it varies with scattering length. A more thorough analysis was obtained when we intentionally evaporated the droplets. This enabled a precise atom number determination for different levitation times and scattering lengths and lead to a measure of the critical atom number as a function of the scattering length. The measure of the critical atom number can be seen as the phase transition line between the dilute liquid phase and the gas phase and thus we created a phase diagram as a function of the relative dipolar strength. Comparing these measurements with performed simulations on the effective Gross-Pitaevskii equation finally allowed to draw conclusions on the background scattering length where we deduced a value $a_{\mathrm{BG}} = 72.7(4.6)\,a_0$. This value included a recently appeared theory that calculated the scattering amplitudes for strongly dipolar gases beyond the Born approximation [78].

Outlook

Future experimental as well as theoretical effort will be needed to further enlighten the properties of a strongly dipolar quantum gas. The recent theory work calculating the scattering amplitudes beyond the Born approximation needs to be experimentally confirmed. This can be done by individual measurements on the s-wave scattering length [116] and on the dipolar scattering cross section [47]. In general, these measurements would enable the critical atom number measurements to be a very precise benchmark for any future theory on a dipolar many-body systems.

The self-bound droplets offer a closed dissipative quantum system that opens the possibility to study many-body physics without being perturbed by the trapping potential. On the other hand, the droplets itself can be considered as a trapping potential for a different species, for example a fermionic isotope. We performed a first calculation of

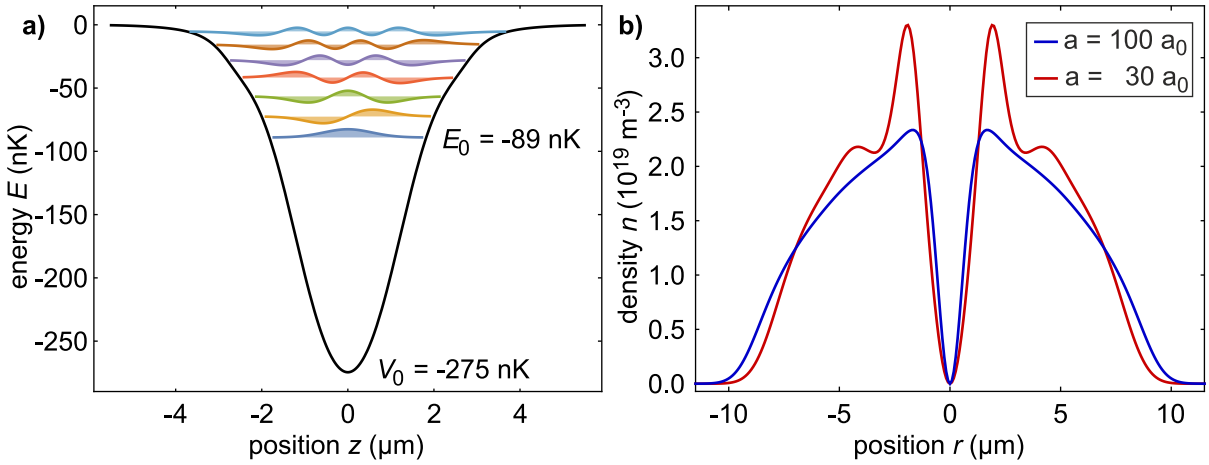

Figure 4.9.: Fermion trapped in a bosonic droplet: a) We show the trapping potential for fermionic ^{163}Dy atoms created by a droplet of bosons with $N = 1{,}000$ atoms at scattering lengths $a_{\mathrm{BB}} = 80\,a_0$ and $a_{\mathrm{BF}} = 40\,a_0$. In the axial direction, we find seven bound states, while there is only one bound state in the radial direction. **Trapped vortex line in a dipolar BEC: b)** We show two cuts of the density profile in radial direction for a trapped vortex in a ^{164}Dy BEC. At high scattering length $a = 100\,a_0$ (blue line), we observe the vortex line as vanishing density in the center of the cloud. For $a = 30\,a_0$ (red line) we see an additional density modification that show typical features of a dipolar BEC close to an instability.

the trapping potential for the ^{163}Dy isotope that is created by a droplet. In short: One needs to calculate the Hamiltonian for a mixture of bosons and non-interacting fermions. Here, one assumes that the fermions do not disturb the state of the bosons. Finally, the trapping potential is given as a function of the density profile of the bosons as well as the scattering length between bosons and fermions. Solving the Schrödinger equation with this potential then yields the energy of the bound states. Using our simulations on the effective Gross-Pitaevskii equation we can extract the density profile for a droplet at $a_{\mathrm{BB}} = 80\,a_0$ with $N = 1{,}000$ atoms and calculate the potential depth as well as the possible bound states. We show our result in figure 4.9a. For a scattering length between bosons and fermions of $a_{\mathrm{BF}} = 40\,a_0$, we find a potential depth of $V_0 = -275\,\mathrm{nK}$. Along the z-direction of the droplet we find seven bound states, where the lowest one has an energy of $E_0 = -89\,\mathrm{nK}$. Due to the large effective radial trapping frequency, we only find one bound state in the radial direction, making this droplet a quasi one-dimensional trap for fermions.

Another interesting research direction will be the study of dimensionality of these dipolar gases. The first question one could ask is if the quantum liquid state can exist in one- or two-dimensional systems as it was calculated for a two-component Bose gas [136]. Very recently, Mishra et. al. calculated the influence of the quantum fluctuations for a quasi

one-dimensional system that surprisingly changes from a repulsive force to an attractive one [137]. Nevertheless, there is a parameter range where a droplet phase exists. However, in two dimensions the quantum fluctuations are repulsive and their effect on a dipolar BEC has yet to be calculated.

Studying two dimensions is of further interest for multiple reasons. Besides the study of quantum fluctuations in these systems, people predicted even more exotic phases. One prominent example is the so-called stripe phase [138] that appears for certain conditions when the polarization axis of the dipoles is tilted towards the atomic plane.

On the experimental side, we will be able to observe the real density distribution in an atomic gas with a single image being taken. For example, a vortex-line in a BEC should be directly observable using our objective. Additionally, stable rotonic features have been predicted and should be directly observable in the density distribution. In figure 4.9b, we show a cut of the density distribution for a BEC consisting of $N = 10{,}000$ atoms for two different scattering lengths with one trapped vortex-line in a trap with trap aspect ratio $\lambda = 10$. At $a = 100\,a_0$ the density distribution is purely disturbed by the vortex, clearly visible in the vanishing density at the center of the cloud. In contrast, at $a = 30\,a_0$ the BEC is close to the instability, where we expect to see an effect of the dipolar character (rotonic excitations). Indeed, we see an enhancement of the density close to the vortex-line followed by an additional minimum before decreasing to zero. All these features are visible on length scales that are on the order of a micrometer, confirming the possibility to observe them with our current experimental setup.

Appendix

A. Image cleaning algorithm

Our imaging process always relies on taking three images after each other. The first image (atom picture) with matrix $\boldsymbol{I}_1$ contains the information about the atoms, either through absorption or dispersion of the imaging light. We typically wait for $t = 150\,\mathrm{ms}$ before taking the second image (bright picture) with the matrix $\boldsymbol{I}_2$ that just contains our imaging light. After another 150 ms we take a third image (dark picture) with matrix $\boldsymbol{I}_3$ where our imaging light is turned off and we measure the background light, together with the dark counts of the camera. For phase contrast imaging, we calculate the column density with equation (3.13). In the case of a droplet which cannot be perfectly resolved by our imaging system it makes sense to only calculate the optical density as these values are strongly disturbed by the astigmatism effects. The optical density is defined as

$$OD = \frac{n_{2\mathrm{D}}}{\sigma_0}, \tag{A.1}$$

with the optical peak absorption cross section $\sigma_0 = \frac{3\lambda^2}{2\pi}$. We show a typical image of the optical density in figure A.1a. We observe strong interference effects visible over the whole camera chip. These result from the fact that the imaging beam is slightly moving between the two images $\boldsymbol{I}_1$ and $\boldsymbol{I}_2$. In principle, reducing the wait time between the two images can help to improve the signal to noise on these images. However, we are limited by the finite read-out time of the image from the camera chip.

An alternative method [139] relies on creating a new bright picture and was derived from the eigenface method [140]. It creates a set of orthogonal eigenvectors to reconstruct the new bright picture that has an optimized phase difference compared to the atom picture. Thus, this method ensures a minimization of any unwanted interference effects in the calculated OD and we will explain the details in the following paragraphs.

For our experiments, we first take a set of bright images. In principle, the signal to noise becomes better the more images we take. However, the computation time also increases, which is why we typically take between 30 and 100 bright images. In a second step we define an area on the image that will be ignored in the cleaning process shown in figure A.1 as green rectangle. This area typically represents the area where we expect the atoms

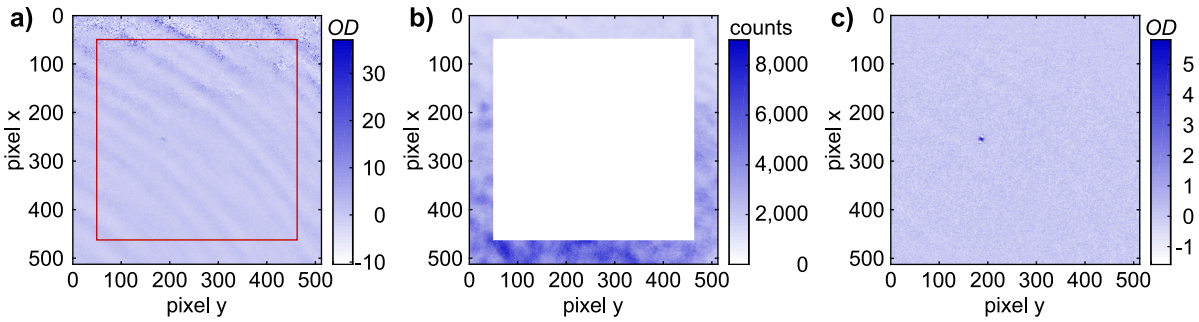

Figure A.1.: Image cleaning algorithm: a) We show the optical density using one set of images ($\boldsymbol{I}_1 - \boldsymbol{I}_3$) calculated with equation (A.1) over the whole camera chip. The positions are relative to the upper left corner of the camera chip. Due to the strong interference effects it almost impossible to observe the atomic cloud. Additionally, the optical density is distorted and does not reflect the one of the atomic cloud. The red rectangle shows the defined atom area. **b)** We show the atom picture of the calculated image in **a**. Here, the atom area was removed from the image and only the outer edge of the image is left over. This image represents the matrix $\tilde{\boldsymbol{I}}_1$ from eq. (A.3) that will be multiplied with the correlation matrix $\boldsymbol{B}$ to extract the eigenvalues in the basis of the reference images. **c)** We show the same image as in **a** after the cleaning process. The interference rings disappeared almost completely and the OD now correctly represents the one of the atomic cloud that is now clearly visible.

to be. The outside area is then used to create a correlation matrix $\boldsymbol{B}$ with

$$\boldsymbol{B}(i,j) = \sum_{n,m} \tilde{\boldsymbol{I}}_{2,i}(n,m) \cdot \tilde{\boldsymbol{I}}_{2,j}(n,m), \tag{A.2}$$

for all bright images i, j where n, m are the row and column indices of the modified bright images $\tilde{\boldsymbol{I}}_2$. Afterwards, we take the raw atom picture $\boldsymbol{I}_1$ and also remove the atom area here, shown in figure A.1b. We multiply this modified matrix $\tilde{\boldsymbol{I}}_1$ with all modified bright images and thus create the product of eigenvalue and eigenvector as

$$\boldsymbol{s}(i) = \sum_{n,m} \tilde{\boldsymbol{I}}_1(n,m) \cdot \tilde{\boldsymbol{I}}_{2,i}(n,m). \tag{A.3}$$

We calculate the vector consisting of all eigenvalues $\boldsymbol{c}$ by solving the following linear system

$$\boldsymbol{B} \cdot \boldsymbol{c} = \boldsymbol{s}. \tag{A.4}$$

Finally, the best bright picture $\boldsymbol{I}_2^*$ is given as a linear combination of all bright images

$\boldsymbol{I}_{2,i}$ with

$$\boldsymbol{I}_2^* = \sum_i \boldsymbol{c}(i) \cdot \boldsymbol{I}_{2,i}. \tag{A.5}$$

We calculate the cleaned optical density as

$$OD^* = 8\frac{\Delta_{421}}{\gamma_{421}} \left\{ \theta - \arccos\left(\sqrt{\frac{I_1 - I_3}{I_2^* - I_3}} \cos\theta \right) \right\}, \tag{A.6}$$

shown in figure A.1c.

B. Principal component analysis

In section 3.3, we performed the principal component analysis [132, 141] to explore the phase diagram of a trapped dipolar BEC. Here, we want to explain the details of this method on the example of the results obtained in section 3.3.1.

In the given example, we measured a total of 780 images. As we are interested in specific details of the individual images, we first subtract the mean of all the images from each image $\boldsymbol{I}_i$

$$\tilde{\boldsymbol{I}}_i = \boldsymbol{I}_i - \frac{1}{N}\left(\sum_i \boldsymbol{I}_i\right), \tag{B.1}$$

with $N = 780$ being the number of images. From these matrices $\hat{\boldsymbol{I}}_i$ we now build the covariance matrix as

$$\boldsymbol{B} = \sum_i \tilde{\boldsymbol{I}}_i \cdot \tilde{\boldsymbol{I}}_i^{\mathsf{T}}. \tag{B.2}$$

Here, we only take a small fraction of the image to minimize the computation time as the covariance matrix scales with the image size squared. We then calculate the eigenvalues as well as the eigenvectors from this matrix and use the eigenvectors as new basis to represent the 780 images. To do so, we simply multiply each image $\tilde{\boldsymbol{I}}_i$ with each eigenvector $\boldsymbol{v}_n$ and result with the corresponding eigenvalues $\alpha_{i,n}$

$$\alpha_{i,n} = \tilde{\boldsymbol{I}}_i \cdot \boldsymbol{v}_n. \tag{B.3}$$

We show the mean image as well as the first two eigenvectors in figure B.1a-c. For these three images, the color bar represents the OD of the images. In section 3.3.1, we were interested in the differentiation between a single droplet and multiple droplets. In figure 3.6 we observed that the squared eigenvalues differ in their contribution for the two mentioned cases. While α^2 for a single droplet already saturated for $n > 40$, we need more than 120 eigenvectors to fully represent the image of multiple droplets. We show this behavior in figure B.1d-i. There, d and g are real images of a single droplet or multiple droplets, respectively. We then simply calculate the linear combination of the eigenvectors and eigenvalues up to $n = 40$ and add the mean of all images from eq. (B.1)

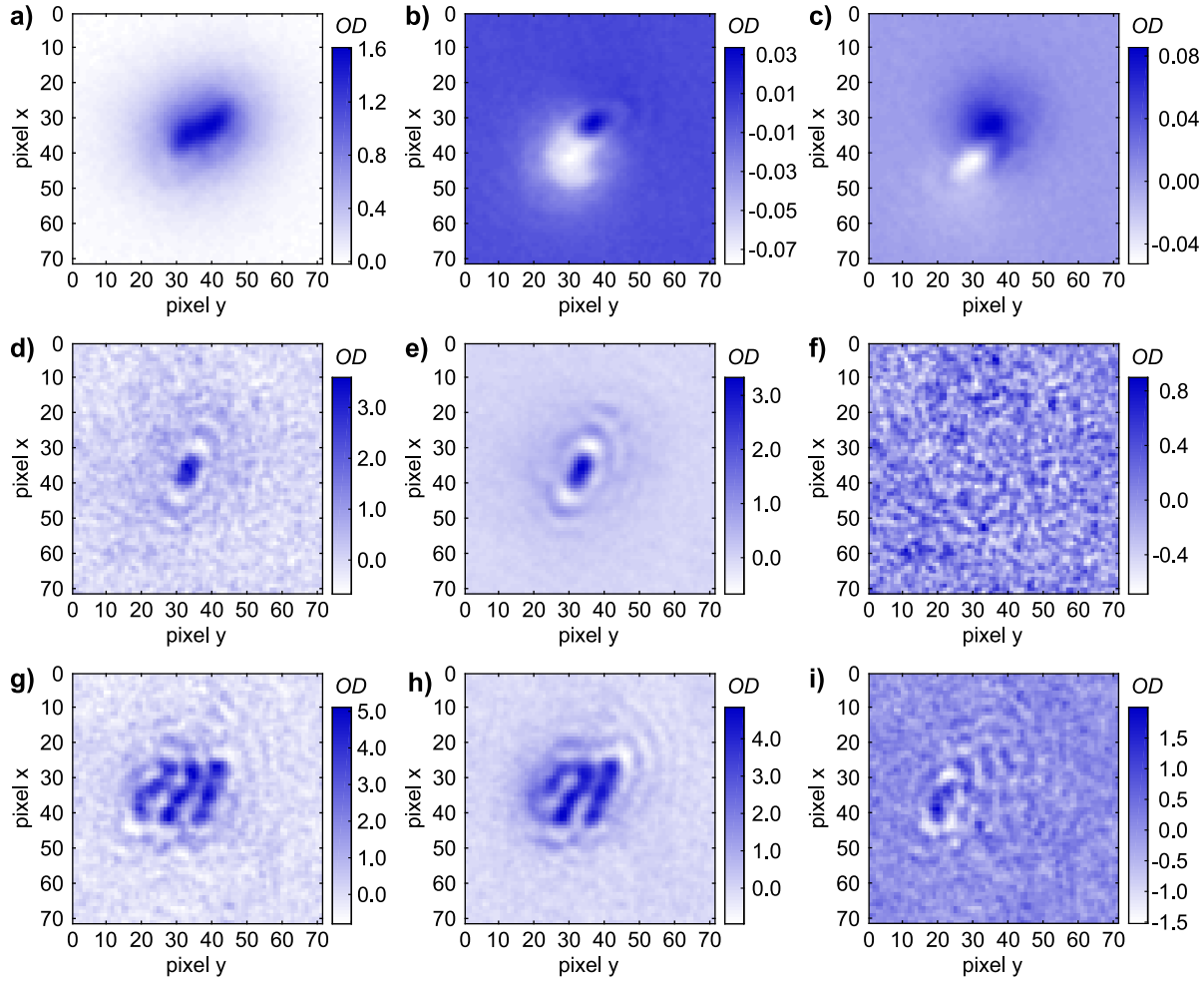

Figure B.1.: Principal component analysis: a) We show the mean image of all 780 images taken for the analysis for a small region on the camera chip. **b),c)** The images represent the first two eigenvectors $\boldsymbol{v}_1$ and $\boldsymbol{v}_2$ that have the largest contribution for all images. **d)-f)** The second row shows a single droplet image, a calculation of the very same image using eq. (B.4) and the difference between the two images. **g)-i)** The third row shows the same but for a multiple droplet image.

to get the images in e and h

$$\boldsymbol{K} = \frac{1}{N}\left(\sum_i \boldsymbol{I}_i\right) + \sum_{n=1}^{40} \alpha_n \boldsymbol{v}_n. \tag{B.4}$$

To see the difference, we subtract the created images $\boldsymbol{K}$ from the real images $\boldsymbol{I}$ and show the results in f and i. While the single droplet image is fully represented besides some white noise, the multiple droplet image clearly misses some features. Following the definition of section 3.3.1, the multiple droplet image is much more complex than a single droplet image.

Bibliography

[1] H. K. Onnes, *Nobel lecture: Investigations into the properties of substances at low temperatures, which have led, amongst other things, to the preparation of liquid helium*, Nobelprize.org (1913).

[2] D. van Delft and P. Kes, *The discovery of superconductivity*, Physics Today, **63**, 38 (2010).

[3] P. Kapitza, *Viscosity of Liquid Helium below the λ-Point*, Nature, **141**, 74 (1938).

[4] J. F. Allen and A. D. Misener, *Flow of Liquid Helium II*, Nature, **141**, 75 (1938).

[5] F. London, *On the Bose-Einstein Condensation*, Phys. Rev., **54**, 947–954 (1938).

[6] K. B. Davis, M. O. Mewes, M. R. Andrews, N. J. van Druten, D. S. Durfee, D. M. Kurn and W. Ketterle, *Bose-Einstein Condensation in a Gas of Sodium Atoms*, Phys. Rev. Lett., **75**, 3969–3973 (1995).

[7] M. H. Anderson, J. R. Ensher, M. R. Matthews, C. E. Wieman and E. A. Cornell, *Observation of Bose-Einstein Condensation in a Dilute Atomic Vapor*, Science, **269**, 198–201 (1995).

[8] C. C. Bradley, C. A. Sackett, J. J. Tollett and R. G. Hulet, *Evidence of Bose-Einstein Condensation in an Atomic Gas with Attractive Interactions*, Phys. Rev. Lett., **75**, 1687–1690 (1995).

[9] I. Bloch, J. Dalibard and W. Zwerger, *Many-body physics with ultracold gases*, Rev. Mod. Phys., **80**, 885–964 (2008).

[10] S. Inouye, M. R. Andrews, J. Stenger, H.-J. Miesner, D. M. Stamper-Kurn and W. Ketterle, *Observation of Feshbach resonances in a Bose-Einstein condensate*, Nature, **392**, 151–154 (1998).

[11] C. Chin, R. Grimm, P. Julienne and E. Tiesinga, *Feshbach resonances in ultracold gases*, Rev. Mod. Phys., **82**, 1225–1286 (2010).

[12] S. Jochim, M. Bartenstein, A. Altmeyer, G. Hendl, S. Riedl, C. Chin, J. Hecker Denschlag and R. Grimm, *Bose-Einstein Condensation of Molecules*, Science, **302**, 2101–2103 (2003).

[13] M. W. Zwierlein, C. A. Stan, C. H. Schunck, S. M. F. Raupach, S. Gupta, Z. Hadzibabic and W. Ketterle, *Observation of Bose-Einstein Condensation of Molecules*, Phys. Rev. Lett., **91**, 250401 (2003).

[14] M. Greiner, C. A. Regal and D. S. Jin, *Emergence of a molecular Bose-Einstein condensate from a Fermi gas*, Nature, **426**, 537–540 (2003).

[15] B. DeMarco and D. S. Jin, *Onset of Fermi Degeneracy in a Trapped Atomic Gas*, Science, **285**, 1703–1706 (1999).

[16] J. P. Toennies and A. F. Vilesov, *Superfluid Helium Droplets: A Uniquely Cold Nanomatrix for Molecules and Molecular Complexes*, Angewandte Chemie International Edition, **43**, 2622–2648 (2004).

[17] G. Volovik, *The Universe in a Helium Droplet*, Oxford Science Publications (2009).

[18] L. F. Gomez, K. R. Ferguson, J. P. Cryan, C. Bacellar, R. M. P. Tanyag, C. Jones, S. Schorb, D. Anielski, A. Belkacem, C. Bernando, R. Boll, J. Bozek, S. Carron, G. Chen, T. Delmas, L. Englert, S. W. Epp, B. Erk, L. Foucar, R. Hartmann, A. Hexemer, M. Huth, J. Kwok, S. R. Leone, J. H. S. Ma, F. R. N. C. Maia, E. Malmerberg, S. Marchesini, D. M. Neumark, B. Poon, J. Prell, D. Rolles, B. Rudek, A. Rudenko, M. Seifrid, K. R. Siefermann, F. P. Sturm, M. Swiggers, J. Ullrich, F. Weise, P. Zwart, C. Bostedt, O. Gessner and A. F. Vilesov, *Shapes and vorticities of superfluid helium nanodroplets*, Science, **345**, 906–909 (2014).

[19] M. Bender, P.-H. Heenen and P.-G. Reinhard, *Self-consistent mean-field models for nuclear structure*, Rev. Mod. Phys., **75**, 121–180 (2003).

[20] J. M. Lattimer and M. Prakash, *The Physics of Neutron Stars*, Science, **304**, 536–542 (2004).

[21] D. S. Petrov, *Quantum Mechanical Stabilization of a Collapsing Bose-Bose Mixture*, Phys. Rev. Lett., **115**, 155302 (2015).

[22] A. Bulgac, *Dilute Quantum Droplets*, Phys. Rev. Lett., **89**, 050402 (2002).

[23] K. E. Strecker, G. B. Partridge, A. G. Truscott and R. G. Hulet, *Formation and propagation of matter-wave soliton trains*, Nature, **417**, 150–153 (2002).

[24] L. Khaykovich, F. Schreck, G. Ferrari, T. Bourdel, J. Cubizolles, L. D. Carr, Y. Castin and C. Salomon, *Formation of a Matter-Wave Bright Soliton*, Science, **296**, 1290–1293 (2002).

[25] A. Griesmaier, J. Werner, S. Hensler, J. Stuhler and T. Pfau, *Bose-Einstein Condensation of Chromium*, Phys. Rev. Lett., **94**, 160401 (2005).

[26] J. Stuhler, A. Griesmaier, T. Koch, M. Fattori, T. Pfau, S. Giovanazzi, P. Pedri and L. Santos, *Observation of Dipole-Dipole Interaction in a Degenerate Quantum Gas*, Phys. Rev. Lett., **95**, 150406 (2005).

[27] S. Giovanazzi, P. Pedri, L. Santos, A. Griesmaier, M. Fattori, T. Koch, J. Stuhler and T. Pfau, *Expansion dynamics of a dipolar Bose-Einstein condensate*, Phys. Rev. A, **74**, 013621 (2006).

[28] T. Lahaye, C. Menotti, L. Santos, M. Lewenstein and T. Pfau, *The physics of dipolar bosonic quantum gases*, Reports on Progress in Physics, **72**, 126401 (2009).

[29] Q. Beaufils, R. Chicireanu, T. Zanon, B. Laburthe-Tolra, E. Maréchal, L. Vernac, J.-C. Keller and O. Gorceix, *All-optical production of chromium Bose-Einstein condensates*, Phys. Rev. A, **77**, 061601 (2008).

[30] T. Koch, T. Lahaye, J. Metz, B. Fröhlich, A. Griesmaier and T. Pfau, *Stabilization of a purely dipolar quantum gas against collapse*, Nature Physics, **4**, 218–222 (2008).

[31] S. Müller, J. Billy, Henn, E. A. L., H. Kadau, A. Griesmaier, M. Jona-Lasinio, L. Santos and T. Pfau, *Stability of a dipolar Bose-Einstein condensate in a one-dimensional lattice*, Physical Review A, **84** (2011).

[32] T. Lahaye, J. Metz, B. Fröhlich, T. Koch, M. Meister, A. Griesmaier, T. Pfau, H. Saito, Y. Kawaguchi and M. Ueda, *d-Wave Collapse and Explosion of a Dipolar Bose-Einstein Condensate*, Phys. Rev. Lett., **101**, 080401 (2008).

[33] J. Metz, T. Lahaye, B. Fröhlich, A. Griesmaier, T. Pfau, H. Saito, Y. Kawaguchi and M. Ueda, *Coherent collapses of dipolar Bose–Einstein condensates for different trap geometries*, New Journal of Physics, **11**, 055032 (2009).

[34] J. Billy, E. A. L. Henn, S. Müller, T. Maier, H. Kadau, A. Griesmaier, M. Jona-Lasinio, L. Santos and T. Pfau, *Deconfinement-induced collapse of a coherent array of dipolar Bose-Einstein condensates*, Phys. Rev. A, **86**, 051603 (2012).

[35] S. Hensler, J. Werner, A. Griesmaier, P. Schmidt, A. Görlitz, T. Pfau, S. Giovanazzi and K. Rzażewski, *Dipolar relaxation in an ultra-cold gas of magnetically trapped chromium atoms*, Applied Physics B, **77**, 765–772 (2003).

[36] B. Pasquiou, G. Bismut, Q. Beaufils, A. Crubellier, E. Maréchal, P. Pedri, L. Vernac, O. Gorceix and B. Laburthe-Tolra, *Control of dipolar relaxation in external fields*, Phys. Rev. A, **81**, 042716 (2010).

[37] M. Fattori, T. Koch, S. Goetz, A. Griesmaier, S. Hensler, J. Stuhler and T. Pfau, *Demagnetization cooling of a gas*, Nat Phys, **2**, 765–768 (2006).

[38] B. Pasquiou, E. Maréchal, G. Bismut, P. Pedri, L. Vernac, O. Gorceix and B. Laburthe-Tolra, *Spontaneous Demagnetization of a Dipolar Spinor Bose Gas in an Ultralow Magnetic Field*, Phys. Rev. Lett., **106**, 255303 (2011).

[39] B. Pasquiou, E. Maréchal, L. Vernac, O. Gorceix and B. Laburthe-Tolra, *Thermodynamics of a Bose-Einstein Condensate with Free Magnetization*, Phys. Rev. Lett., **108**, 045307 (2012).

[40] G. Bismut, B. Pasquiou, E. Maréchal, P. Pedri, L. Vernac, O. Gorceix and B. Laburthe-Tolra, *Collective Excitations of a Dipolar Bose-Einstein Condensate*, Phys. Rev. Lett., **105**, 040404 (2010).

[41] G. Bismut, B. Laburthe-Tolra, E. Maréchal, P. Pedri, O. Gorceix and L. Vernac, *Anisotropic Excitation Spectrum of a Dipolar Quantum Bose Gas*, Phys. Rev. Lett., **109**, 155302 (2012).

[42] A. Griesmaier, J. Stuhler, T. Koch, M. Fattori, T. Pfau and S. Giovanazzi, *Comparing Contact and Dipolar Interactions in a Bose-Einstein Condensate*, Phys. Rev. Lett., **97**, 250402 (2006).

[43] T. Lahaye, T. Koch, B. Frohlich, M. Fattori, J. Metz, A. Griesmaier, S. Giovanazzi and T. Pfau, *Strong dipolar effects in a quantum ferrofluid*, Nature, **448**, 672–675 (2007).

[44] M. Lu, N. Q. Burdick, S. H. Youn and B. L. Lev, *Strongly Dipolar Bose-Einstein Condensate of Dysprosium*, Phys. Rev. Lett., **107**, 190401 (2011).

[45] M. Lu, N. Q. Burdick and B. L. Lev, *Quantum Degenerate Dipolar Fermi Gas*, Phys. Rev. Lett., **108**, 215301 (2012).

[46] K. Aikawa, A. Frisch, M. Mark, S. Baier, A. Rietzler, R. Grimm and F. Ferlaino, *Bose-Einstein Condensation of Erbium*, Phys. Rev. Lett., **108**, 210401 (2012).

[47] K. Aikawa, A. Frisch, M. Mark, S. Baier, R. Grimm and F. Ferlaino, *Reaching Fermi Degeneracy via Universal Dipolar Scattering*, Physical Review Letters, **112**, 010404 (2014).

[48] A. Frisch, M. Mark, K. Aikawa, F. Ferlaino, J. L. Bohn, C. Makrides, A. Petrov and S. Kotochigova, *Quantum chaos in ultracold collisions of gas-phase erbium atoms*, Nature, **507**, 475–479 (2014).

[49] T. Maier, H. Kadau, M. Schmitt, M. Wenzel, I. Ferrier-Barbut, T. Pfau, A. Frisch, S. Baier, K. Aikawa, L. Chomaz, M. J. Mark, F. Ferlaino, C. Makrides, E. Tiesinga, A. Petrov and S. Kotochigova, *Emergence of Chaotic Scattering in Ultracold Er and Dy*, Phys. Rev. X, **5**, 041029 (2015).

[50] A. Frisch, M. Mark, K. Aikawa, S. Baier, R. Grimm, A. Petrov, S. Kotochigova, G. Quéméner, M. Lepers, O. Dulieu and F. Ferlaino, *Ultracold Dipolar Molecules Composed of Strongly Magnetic Atoms*, Phys. Rev. Lett., **115**, 203201 (2015).

[51] T. Maier, I. Ferrier-Barbut, H. Kadau, M. Schmitt, M. Wenzel, C. Wink, T. Pfau, K. Jachymski and P. S. Julienne, *Broad universal Feshbach resonances in the chaotic spectrum of dysprosium atoms*, Phys. Rev. A, **92**, 060702(R) (2015).

[52] H. Kadau, M. Schmitt, M. Wenzel, C. Wink, T. Maier, I. Ferrier-Barbut and T. Pfau, *Observing the Rosensweig instability of a quantum ferrofluid*, Nature, **530**, 194–197 (2016).

[53] M. D. Cowley and R. E. Rosensweig, *The interfacial stability of a ferromagnetic fluid*, Journal of Fluid Mechanics, **30**, 671–688 (1967).

[54] I. Ferrier-Barbut, H. Kadau, M. Schmitt, M. Wenzel and T. Pfau, *Observation of Quantum Droplets in a Strongly Dipolar Bose Gas*, Phys. Rev. Lett., **116**, 215301 (2016).

[55] S. Bose, *Plancks Gesetz und Lichtquantenhypothese*, Zeitschrift für Physik, **26**, 178–181 (1924).

[56] A. Einstein, *Quantentheorie des einatomigen idealen Gases*, Sitzungsberichte der Preussischen Akademie der Wissenschaften, pages 261–267 (1924).

[57] A. Einstein, *Quantentheorie des einatomigen idealen Gases. 2. Abhandlung*, Sitzungsberichte der Preussischen Akademie der Wissenschaften, pages 3–14 (1925).

[58] L. Landau, *Theory of the Superfluidity of Helium II*, Phys. Rev., **60**, 356–358 (1941).

[59] O. Penrose, *CXXXVI. On the quantum mechanics of helium II*, The London, Edinburgh, and Dublin Philosophical Magazine and Journal of Science, **42**, 1373–1377 (1951).

[60] O. Penrose and L. Onsager, *Bose-Einstein Condensation and Liquid Helium*, Phys. Rev., **104**, 576–584 (1956).

[61] W. D. Phillips, *Nobel Lecture: Laser cooling and trapping of neutral atoms*, Rev. Mod. Phys., **70**, 721–741 (1998).

[62] C. C. Bradley, C. A. Sackett and R. G. Hulet, *Bose-Einstein Condensation of Lithium: Observation of Limited Condensate Number*, Phys. Rev. Lett., **78**, 985–989 (1997).

[63] L. P. Pitaevskii and S. Sandro, *Bose-Einstein Condensation*, Oxford University Press (2003).

[64] C. J. Pethick and H. Smith, *Bose-Einstein Condensation in Dilute Gases*, Cambridge University Press (2002).

[65] W. Ketterle, D. S. Durfee and D. M. Stamper-Kurn, *Making, probing and understanding Bose-Einstein condensates*, arXiv:cond-mat:9904034 (1999).

[66] F. Dalfovo, S. Giorgini, L. P. Pitaevskii and S. Stringari, *Theory of Bose-Einstein condensation in trapped gases*, Rev. Mod. Phys., **71**, 463–512 (1999).

[67] E. A. Donley, N. R. Claussen, S. L. Cornish, J. L. Roberts, E. A. Cornell and C. E. Wieman, *Dynamics of collapsing and exploding Bose-Einstein condensates*, Nature, **412**, 295–299 (2001).

[68] J. Dalibard, *Collisional dynamics of ultra-cold atomic gases*, IOS Press in *Bose-Einstein Condensation in Atomic Gases: Proceedings of the International School of Physics "Enrico Fermi"* (1998).

[69] S. Müller, *Stability and Collapse Dynamics of Dipolar Bose-Einstein Condensates in One-Dimensional Optical Lattices*, Ph.D. thesis, Universität Stuttgart (2012).

[70] M. Marinescu and L. You, *Controlling Atom-Atom Interaction at Ultralow Temperatures by dc Electric Fields*, Phys. Rev. Lett., **81**, 4596–4599 (1998).

[71] H. Feshbach, *Unified theory of nuclear reactions*, Annals of Physics, **5**, 357 – 390 (1958).

[72] U. Fano, *Effects of Configuration Interaction on Intensities and Phase Shifts*, Phys. Rev., **124**, 1866–1878 (1961).

[73] P. O. Fedichev, Y. Kagan, G. V. Shlyapnikov and J. T. M. Walraven, *Influence of Nearly Resonant Light on the Scattering Length in Low-Temperature Atomic Gases*, Phys. Rev. Lett., **77**, 2913–2916 (1996).

[74] J. L. Bohn and P. S. Julienne, *Prospects for influencing scattering lengths with far-off-resonant light*, Phys. Rev. A, **56**, 1486–1491 (1997).

[75] R. Zhang, Y. Cheng, H. Zhai and P. Zhang, *Orbital Feshbach Resonance in Alkali-Earth Atoms*, Phys. Rev. Lett., **115**, 135301 (2015).

[76] G. E. Astrakharchik and Y. E. Lozovik, *Super-Tonks-Girardeau regime in trapped one-dimensional dipolar gases*, Phys. Rev. A, **77**, 013404 (2008).

[77] S. Yi and L. You, *Trapped condensates of atoms with dipole interactions*, Phys. Rev. A, **63**, 053607 (2001).

[78] R. Ołdziejewski and K. Jachymski, *Properties of strongly dipolar Bose gases beyond the Born approximation*, Physical Review A, **94** (2016).

[79] G. Baym and C. J. Pethick, *Ground-State Properties of Magnetically Trapped Bose-Condensed Rubidium Gas*, Phys. Rev. Lett., **76**, 6–9 (1996).

[80] V. M. Pérez-García, H. Michinel, J. I. Cirac, M. Lewenstein and P. Zoller, *Low Energy Excitations of a Bose-Einstein Condensate: A Time-Dependent Variational Analysis*, Phys. Rev. Lett., **77**, 5320–5323 (1996).

[81] D. H. J. O'Dell, S. Giovanazzi and C. Eberlein, *Exact Hydrodynamics of a Trapped Dipolar Bose-Einstein Condensate*, Phys. Rev. Lett., **92**, 250401 (2004).

[82] C. Eberlein, S. Giovanazzi and D. H. J. O'Dell, *Exact solution of the Thomas-Fermi equation for a trapped Bose-Einstein condensate with dipole-dipole interactions*, Phys. Rev. A, **71**, 033618 (2005).

[83] T. D. Lee and C. N. Yang, *Many-Body Problem in Quantum Mechanics and Quantum Statistical Mechanics*, Phys. Rev., **105**, 1119–1120 (1957).

[84] T. D. Lee, K. Huang and C. N. Yang, *Eigenvalues and Eigenfunctions of a Bose System of Hard Spheres and Its Low-Temperature Properties*, Phys. Rev., **106**, 1135–1145 (1957).

[85] N. N. Bogolyubov, *On the theory of superfluidity*, J. Phys.(USSR), **11**, 23–32 (1947).

[86] A. R. P. Lima and A. Pelster, *Quantum fluctuations in dipolar Bose gases*, Phys. Rev. A, **84**, 041604 (2011).

[87] A. R. P. Lima and A. Pelster, *Beyond mean-field low-lying excitations of dipolar Bose gases*, Phys. Rev. A, **86**, 063609 (2012).

[88] F. Wächtler and L. Santos, *Quantum filaments in dipolar Bose-Einstein condensates*, Phys. Rev. A, **93**, 061603 (2016).

[89] S. Yi and L. You, *Trapped atomic condensates with anisotropic interactions*, Phys. Rev. A, **61**, 041604 (2000).

[90] R. N. Bisset, R. M. Wilson, D. Baillie and P. B. Blakie, *Ground-state phase diagram of a dipolar condensate with quantum fluctuations*, Phys. Rev. A, **94**, 033619 (2016).

[91] D. Peter, *Theoretical investigations of dipolar quantum gases in multi-well potentials*, Diploma thesis, Universität Stuttgart (2015).

[92] F. Dalfovo and S. Stringari, *Helium nanodroplets and trapped Bose-Einstein condensates as prototypes of finite quantum fluids*, The Journal of Chemical Physics, **115**, 10078–10089 (2001).

[93] D. M. Ceperley and E. Manousakis, *Path integral Monte Carlo applications to quantum fluids in confined geometries*, The Journal of Chemical Physics, **115**, 10111 (2001).

[94] E. Krotscheck and R. Zillich, *Dynamics of ^{4}He droplets*, The Journal of Chemical Physics, **115**, 10161 (2001).

[95] S. Stringari and J. Treiner, *Surface properties of liquid ^{3}He and ^{4}He: A density-functional approach*, Phys. Rev. B, **36**, 8369–8375 (1987).

[96] S. Stringari and J. Treiner, *Systematics of liquid helium clusters*, The Journal of Chemical Physics, **87**, 5021 (1987).

[97] W. Ketterle and N. V. Druten, *Evaporative Cooling of Trapped Atoms*, volume 37 of *Advances In Atomic, Molecular, and Optical Physics*, pages 181 – 236, Academic Press (1996).

[98] E. A. Donley, N. R. Claussen, S. T. Thompson and C. E. Wieman, *Atom-molecule coherence in a Bose-Einstein condensate*, Nature, **417**, 529–533 (2002).

[99] A. E. Leanhardt, T. A. Pasquini, M. Saba, A. Schirotzek, Y. Shin, D. Kielpinski, D. E. Pritchard and W. Ketterle, *Cooling Bose-Einstein Condensates Below 500 Picokelvin*, Science, **301**, 1513–1515 (2003).

[100] M. Hartmann, R. E. Miller, J. P. Toennies and A. Vilesov, *Rotationally Resolved Spectroscopy of SF_6 in Liquid Helium Clusters: A Molecular Probe of Cluster Temperature*, Phys. Rev. Lett., **75**, 1566–1569 (1995).

[101] D. M. Brink and S. Stringari, *Density of states and evaporation rate of helium clusters*, Zeitschrift für Physik D Atoms, Molecules and Clusters, **15**, 257–263 (1990).

[102] F. Dalfovo, L. Pitaevskii and S. Stringari, *Order parameter at the boundary of a trapped Bose gas*, Phys. Rev. A, **54**, 4213–4217 (1996).

[103] J. Harms, J. P. Toennies and F. Dalfovo, *Density of superfluid helium droplets*, Phys. Rev. B, **58**, 3341–3350 (1998).

[104] J. Treiner, *Small drops of saturating fluids*, International Workshop on Semi-classical and Phase Space Approaches of the Nucleus, **48**, C2–107–C2–116 (1987).

[105] P. A. Ruprecht, M. J. Holland, K. Burnett, and Mark Edwards, *Time-dependent solution of the nonlinear Schrodinger equation for Bose-condensed trapped neutral atoms*, Physical Review A, **51**, 4704–4711 (1995).

[106] J. L. Roberts, N. R. Claussen, S. L. Cornish, E. A. Donley, E. A. Cornell and C. E. Wieman, *Controlled collapse of a Bose-Einstein condensate*, Physical Review Letters, **86**, 4211–4214 (2001).

[107] L. Santos, G. V. Shlyapnikov, P. Zoller and M. Lewenstein, *Bose-Einstein Condensation in Trapped Dipolar Gases*, Physical Review Letters, **85**, 1791–1794 (2000).

[108] P. Ehrenfest, *Phasenumwandlungen im ueblichen und erweiterten Sinn, classifiziert nach den entsprechenden Singularitaeten des thermodynamischen Potentiales*, Proceedings Royal Acad. Amsterdam, **36**, 153–157 (1933).

[109] S. Ronen, D. C. E. Bortolotti and J. L. Bohn, *Radial and Angular Rotons in Trapped Dipolar Gases*, Phys. Rev. Lett., **98**, 030406 (2007).

[110] D. H. J. O'Dell, S. Giovanazzi and G. Kurizki, *Rotons in Gaseous Bose-Einstein Condensates Irradiated by a Laser*, Phys. Rev. Lett., **90**, 110402 (2003).

[111] L. Santos, G. V. Shlyapnikov and M. Lewenstein, *Roton-Maxon Spectrum and Stability of Trapped Dipolar Bose-Einstein Condensates*, Phys. Rev. Lett., **90**, 250403 (2003).

[112] H. Kadau, *Rosensweig Instability and Droplets in a Quantum Ferrofluid of Dysprosium Atoms*, Ph.D. thesis, Universität Stuttgart (2016).

[113] I. Ferrier-Barbut, M. Schmitt, M. Wenzel, H. Kadau and T. Pfau, *Liquid quantum droplets of ultracold magnetic atoms*, Journal of Physics B: Atomic, Molecular and Optical Physics, **49**, 214004 (2016).

[114] F. Wächtler and L. Santos, *Ground-state properties and elementary excitations of quantum droplets in dipolar Bose-Einstein condensates*, Phys. Rev. A, **94**, 043618 (2016).

[115] D. Baillie, R. M. Wilson, R. N. Bisset and P. B. Blakie, *Self-bound dipolar droplet: A localized matter wave in free space*, Physical Review A, **94** (2016).

[116] L. Chomaz, S. Baier, D. Petter, M. J. Mark, F. Wächtler, L. Santos and F. Ferlaino, *Quantum-Fluctuation-Driven Crossover from a Dilute Bose-Einstein Condensate to a Macrodroplet in a Dipolar Quantum Fluid*, Phys. Rev. X, **6**, 041039 (2016).

[117] T. Weber, J. Herbig, M. Mark, H.-C. Nägerl and R. Grimm, *Three-Body Recombination at Large Scattering Lengths in an Ultracold Atomic Gas*, Phys. Rev. Lett., **91**, 123201 (2003).

[118] T. Maier, *Interactions in a Quantum Gas of Dysprosium Atoms*, Ph.D. thesis, Universität Stuttgart (2015).

[119] I. Segal, L. Halicz and I. T. Platzner, *Isotope ratio measurements of dysprosium by multiple collection inductively coupled plasma mass spectrometry*, International Journal of Mass Spectrometry, **216**, 177 – 184 (2002).

[120] A. Petrov, E. Tiesinga and S. Kotochigova, *Anisotropy-induced Feshbach resonances in a quantum dipolar gas of highly magnetic atoms*, Physical Review Letters, **109**, 103002 (2012).

[121] Y. Tang, A. Sykes, N. Q. Burdick, J. L. Bohn and B. L. Lev, *s-wave scattering lengths of the strongly dipolar bosons* ^{162}Dy *and* ^{164}Dy, Phys. Rev. A, **92**, 022703 (2015).

[122] K. Jachymski and P. S. Julienne, *Analytical model of overlapping Feshbach resonances*, Phys. Rev. A, **88**, 052701 (2013).

[123] Y. Tang, A. G. Sykes, N. Q. Burdick, J. M. DiSciacca, D. S. Petrov and B. L. Lev, *Anisotropic Expansion of a Thermal Dipolar Bose Gas*, Physical Review Letters, **117**, 155301 (2016).

[124] T. Maier, H. Kadau, M. Schmitt, A. Griesmaier and T. Pfau, *Narrow-line magneto-optical trap for dysprosium atoms*, Optics letters, **39**, 3138–3141 (2014).

[125] R. Grimm, M. Weidemüller and Y. B. Ovchinnikov, *Optical Dipole Traps for Neutral Atoms*, volume 42 of *Advances In Atomic, Molecular, and Optical Physics*, pages 95 – 170, Academic Press (2000).

[126] B. E. A. Saleh and M. C. Teich, *Fundamentals of Photonics*, John Wiley & Sons, Inc. (1991).

[127] M. Gustavsson, H. Lundberg, L. Nilsson and S. Svanberg, *Lifetime measurements for excited states of rare-earth atoms using pulse modulation of a cw dye-laser beam*, J. Opt. Soc. Am., **69**, 984–992 (1979).

[128] I. Reis, *Hochauflösendes Abbildungssystem für ultrakalte Atome*, Bachelor's thesis, Universität Stuttgart (2014).

[129] C. C. Bradley, C. A. Sackett and R. G. Hulet, *Bose-Einstein Condensation of Lithium: Observation of Limited Condensate Number*, Phys. Rev. Lett., **78**, 985–989 (1997).

[130] M. Wenzel, *A dysprosium quantum gas in highly controllable optical traps*, Master's thesis, Universität Stuttgart (2015).

[131] H. Li, J.-F. Wyart, O. Dulieu, S. Nascimbène and M. Lepers, *Optical trapping of ultracold dysprosium atoms: transition probabilities, dynamic dipole polarizabilities and van der Waals C_6 coefficients*, arXiv:1607.05628 (2016).

[132] S. R. Segal, Q. Diot, E. A. Cornell, A. A. Zozulya and D. Z. Anderson, *Revealing buried information: Statistical processing techniques for ultracold-gas image analysis*, Physical Review A, **81** (2010).

[133] P. O. Fedichev, M. W. Reynolds and G. V. Shlyapnikov, *Three-Body Recombination of Ultracold Atoms to a Weakly Bound s Level*, Phys. Rev. Lett., **77**, 2921–2924 (1996).

[134] Z. Shotan, O. Machtey, S. Kokkelmans and L. Khaykovich, *Three-Body Recombination at Vanishing Scattering Lengths in an Ultracold Bose Gas*, Phys. Rev. Lett., **113**, 053202 (2014).

[135] Y. Wang and P. S. Julienne, *Universal van der Waals physics for three cold atoms near Feshbach resonances*, Nature Physics, **10**, 768–773 (2014).

[136] D. S. Petrov and G. E. Astrakharchik, *Ultradilute Low-Dimensional Liquids*, Phys. Rev. Lett., **117**, 100401 (2016).

[137] C. Mishra, D. Edler, F. Wächtler, R. Nath, S. Sinha and L. Santos, *Quantum droplets in one-dimensional dipolar Bose-Einstein condensates*, arXiv:1610.09176v2 (2016).

[138] A. Macia, D. Hufnagl, F. Mazzanti, J. Boronat and R. E. Zillich, *Excitations and Stripe Phase Formation in a Two-Dimensional Dipolar Bose Gas with Tilted Polarization*, Phys. Rev. Lett., **109**, 235307 (2012).

[139] C. F. Ockeloen, A. F. Tauschinsky, R. J. C. Spreeuw and S. Whitlock, *Detection of small atom numbers through image processing*, Phys. Rev. A, **82**, 061606 (2010).

[140] L. Sirovich and M. Kirby, *Low-dimensional procedure for the characterization of human faces*, J. Opt. Soc. Am. A, **4**, 519–524 (1987).

[141] R. Desbuquois, *Thermal and superfluid properties of the two-dimensional Bose gas*, Ph.D. thesis, Université Pierre et Marie Curie - Paris VI (2013).

Ohne Freunde möchte niemand leben, auch wenn er alle übrigen Güter besäße.

(Aristoteles)

Danksagung

Es ist mir eine besondere Freude am Ende all jenen zu danken, die mich auf dem langen Weg zur erfolgreichen Promotion begleitet und unterstützt haben.

Mein erster Dank gilt meinem Doktorvater Tilman Pfau. Danke für die Aufnahme in deinem Institut, die bereits im Jahr 2010 im Rahmen einer Bachelorarbeit war. Seitdem war es mir eine Freude zusammen mit dir die dipolare Quantenwelt zu erforschen. Du hast es stets verstanden auch in schwere Zeiten die Motivation aufrecht zu erhalten und nach vorne zu blicken. Ich habe in der Zeit viel von dir lernen können.

Next, i would like to thank Hidenori Takagi for being a part of the defense committee of this thesis. Im selben Atemzug möchte ich Hans Peter Büchler danken für die Übernahme des Prüfungsvorsitzes und die zahlreichen Diskussionen, die unserem Verständnis der gemessenen Daten sehr geholfen haben.

Ein besonderer Dank geht an meine beiden Vorgänger Thomas Maier und Holger Kadau. Eure Betreuung während meiner Masterarbeit, als auch die Zusammenarbeit während unserer gemeinsamen Doktorandenzeit hat mir sehr gut gefallen. Ich habe uns immer als Dreamteam gesehen, dass zusammen alle Probleme lösen könnte.

Unterstützt wurde unser Dreamteam zu Beginn von unserem Gruppenleiter Axel Griesmaier, dem ich hiermit danken möchte. Durch deine langjährige Erfahrung am Chromexperiment hast du vor allem in der Anfangszeit mit deinem technischen und physikalischen Verständnis sehr weitergeholfen.

Als nächstes möchte ich mich bei unserem Postdoc und späteren Gruppenleiter Igor Ferrier-Barbut bedanken. Du hast unser Experiment durch dein unglaubliches Wissen weit vorangebracht und ich bin mir sicher, dass du bald deine eigene Gruppe zum Erfolg führen wirst. Dafür wünsche ich dir für die Zukunft alles Gute.

Mein nächster Dank geht an Matthias Wenzel. Du hast sowohl während deiner Masterarbeit, als in der anschließenden Doktorandenzeit sehr zum Erfolg des Experimentes beigetragen. Ich wünsche dir zusammen mit Fabian Böttcher weiterhin eine erfolgreiche Zeit. Es hat mir stets Spaß gemacht mit euch beiden zu arbeiten. Ihr habt die Maschine voll im Griff!

Ich bedanke mich bei allen Diplom-, Bachelor- und Masterstudenten: Bernd Doctors, Nikolas Zuber, Matthias Feldmaier, Michaela Nickel, Isabel Reis, Clarissa Wink, Niklas Uhl und Tobias Sixt. Ihr alle habt mit euren Projekten das Experiment unterstützt und vorangebracht.

Besonders bedanken möchte ich mich bei Thomas "Balu" Baluktsian. Auch wenn du bereits kurz nach dem Beginn meiner Doktorarbeit das Institut verlassen hast, genieße ich es nach wie vor mit dir etwas zu unternehmen. Ich hoffe, dass unsere Freundschaft noch sehr lange anhält.

Vielen Dank an Ralf Ritter und Hannes Gorniaczyk für die musikalische Gestaltung neben der Promotion. Unsere Sessions haben mir sehr viel Spaß gemacht und ich hoffe, dass wir das in der Zukunft nochmal wiederholen können.

Als nächstes möchte ich mich bei meiner Tanzpartnerin Kathrin Kleinbach bedanken. Ich hoffe, dass wir uns noch weiterhin einmal die Woche auf die Füße treten werden.

Die Organisation des Instituts funktioniert nur dank der tollen Arbeit des Sekretariats. Dafür bedanke ich mich bei Astrid Buck, Karin Otter, Oliver Nagel, Nadine Prellwitz, Katrin Maier und Britta Lenz.

Weiter möchte ich dem kompletten PI5 danken für die schöne Zeit, die ich mit euch erleben durfte. Ob Mittagspause, Kaffeepause, DPG Tagung oder der kurze Tratsch auf dem Gang, es hat mir sehr viel Spaß mit euch gemacht.

Zum Schluss möchte ich dann noch meiner ganzen Familie danken. Ihr habt mich alle stets unterstützt, auch wenn es einmal nicht so lief wie ich es mir erhofft hatte. Ich konnte jederzeit auf eure Hilfe bauen, ob aus Gilzem oder Stuttgart. Vielen Dank, ihr seid klasse.